Quantifying the dynamic response of permafrost and slope stability to a changing climate

Huw Thomas Mithan

School of Earth and Ocean Sciences
Cardiff University

Submitted in partial fulfilment of the requirements for the degree of
Doctor of Philosophy

April 2018

Abstract

The Arctic contains a wealth of landforms that are governed by the diurnal and seasonal response of permafrost to climatic and topographic forcings. Of key importance to the process rates of many periglacial landforms is the dynamic behaviour of the active layer, which regulates the transfer of heat and moisture between the atmosphere and permafrost. The strong dependence of periglacial process rates on active layer dynamics makes this geomorphic system particularly sensitive to future increases in Arctic temperatures and precipitation. These increases will continue to degrade permafrost, affecting the distribution and rates of periglacial processes. I develop a landform classification model on Svalbard that reveals solifluction and scree to be the most dominant hillslope processes acting on this landscape, with sediment fluxes greatest in solifluction. A combination of landslide mapping, solifluction modelling and slope stability analysis in Alaska reveals that landslides are coincident with convergent topography on soliflucting hillslopes that have concentrated ground ice at depth. Convergent topography allows for higher moisture availability that feeds the growth, concentration, and development of a large network of ice lenses at the permafrost/active layer boundary. The excess pore pressures generated upon thaw reduces the shear strength of soil at the base of the active layer, causing it to slide downslope along a planar slip surface on top of the unthawed permafrost. Due to a warming Arctic, permafrost is expected to continue thawing, creating an ever more dynamic and deeper active layer. Consequently, the relative regional extent of periglacial landforms in mountainous Arctic environments is expected to change, with Arctic hillslopes becoming more unstable during extreme summer thawing. This will pose a greater hazard to Arctic infrastructure and act as a major force for environmental and geomorphological change.

Acknowledgements

The past four years have been the longest and toughest, but also the most fulfilling. I come out of this PhD a better person, with more knowledge about the natural landscape. Without the help of my family, friends, and colleagues I couldn't have done it. I have many wonderful people to thank.

First and foremost I am profoundly grateful to TC. Without you, none of this would have happened. I remember as an undergraduate I wanted to do a glacial mapping project in Snowdonia for my 3rd-year dissertation. My tutor, Dr Jenny Pike, told me to go and see you, the guy from New Zealand! Who would have thought that 7 years later (including two undergraduate dissertations, one master's thesis) I would be finishing my PhD with you! My biggest aspiration since starting university was to become a professional researcher and you've helped me fulfil that. I remember being asked if I wanted to work with you on this PhD. You told me this wouldn't be easy for me and I now realise it probably wasn't easy for you too, so thank you for your patience. I would not be where I am today without your guidance, support and teaching. I still have much to learn from you, so I hope we can continue to work together. I'm looking forward to publishing our work. You've been the best mentor and the biggest influence on my work. I'm very proud to have been your PhD student! Diolch yn fawr TC.

I want to thank my second supervisor, Dr Peter Cleall. Thank you so much for your guidance and mentoring. Your input has been invaluable, especially because of your engineering background which has kept me focused on smaller scale processes. I will miss our meetings with TC, mainly because of the enlightening discussions that you two have for the first 15 minutes or so! You've been very patient with me. Diolch yn fawr!

Diolch yn fawr to Dr Jose Constantine for your enthusiastic approach to geomorphology.

I would like to thank all the guys in the geomorphology lab, Rhodri Thomas, Ollie, and the now Dr Josh Ahmed and Dr Alex Horton, for their help and antics over the past four years. Dr Lisa Mol for letting me join her trip to Svalbard during the summer of 2014. All the teaching staff in the University Centre on Svalbard (UNIS)

for improving my understanding of the periglacial environment, the Permafrost and Periglacial Environments course in 2015 was enlightening, to say the least. Dr Rob Parker for helping me out with learning to code in Python during the early and now not so vivid days of my PhD. Dr Ian Thomas for his help during the later and more vivid stages of my PhD when I became more advanced in Python. On the same note, I want to thank the online community on Stack Overflow for answering so many of my python questions. Also a big thank you to the developers of python and other open source software I have utilised.

A special thank you to my old housemates Jon and Paul and to my extended circle of friends here in Cardiff. I especially want to thank Jon for being such a good friend, you've kept me sane with so many climbing and hiking adventures. A special thank you to Laurence for always having time for me.

Thank you to my two good friends from my home in Eryri (Snowdonia), David and Ieuan. Even though we only see each other during public holidays, our walks in northern Eryri have always been adventurous and a way for me to vent my PhD frustrations at someone. Naturally, I thank the beautiful and inspiring landscape of Eryri too.

Even though I haven't met the following, I would like to give a special mention to the work of Professor Emeritus Charles Harris and Professor Antoni Lewkowicz as their research provided a basis for this PhD.

Honourable mentions include my laptop, how it has survived hours of model runs I do not know. My road bike for keeping me sane with exercise. Also Cardiff University Mountaineering Club for taking me to places with lots of awesome geomorphology!

Finally but most emphatically I wish to thank my parents. Your love, support, and stability have been the foundation for my success so far. You're the best parents in the world. Thank you for encouraging me to take this PhD. And lastly to Sophie, you're love and support has helped me through the toughest times of this PhD. You've never doubted me, even when I've doubted myself. Without you, I couldn't have finished. Thank you for your endless happiness.

In loving memory of my oldest brother James

Table of contents

List of figures

List of tables

Frequently used acronyms

ALD(s) Active layer detachment(s)

AUC Area under the curve

DEM(s) Digital elevation model(s)

F of S Factor of safety

GIS Geographical information system

GLM Generalised linear model

GPU Geomorphological process unit

IFSAR Interferometric Synthetic Aperture Radar

LD Linear discriminant

LDA Linear discriminant analysis

LiDAR Light detection and ranging

SOC Soil organic carbon

Chapter 1

Introduction

1.1 Global context, rationale, and motivation

The morphology of mountainous Arctic landscapes is the result of geomorphological processes that are driven by glaciations and the freezing and thawing of ground over thousands of years (French 2007). These periglacial landscapes, form in areas that are currently underlain with or have had permafrost. Today, permafrost covers 12.8 to 17.8% of the Earth's land surface area, most of which is in the northern hemisphere(Harris et al. 2001a; French 2007; Tarnocai et al. 2009; Zhang et al. 2000; Gruber 2012). The diurnal and seasonal response of permafrost to climatic and topographic forcings governs the morphology and extent of periglacial landforms (Etzelmüller et al. 2001; French 2007; Aalto et al. 2014). Of key importance to the process rates of many periglacial landforms is the dynamic behaviour of the active layer, which regulates the transfer of heat and moisture between the atmosphere and permafrost (Matsuoka 2001a). The strong dependence of periglacial process rates on active layer dynamics makes this geomorphological system particularly sensitive to current global warming. Future increases in Arctic temperatures and precipitation (Stocker et al. 2013; Cohen et al. 2014) will continue to degrade

permafrost (Osterkamp 2003; Harris et al. 2009), affecting the distribution and rates of periglacial processes (Akerman 2005).

Currently, our understanding of how current global warming will affect periglacial processes and their rates is in its infancy. International permafrost monitoring collaborations such as the Permafrost and Climate in Europe (PACE) project (Harris et al. 2001a; Harris et al. 2009) and Circumpolar Active Layer Monitoring programme (CALM) (Brown et al. 2000; Akerman and Johansson 2008) have observed changes in the rate of periglacial processes with a deepening active layer. Greater monitoring is being supported by an improved quantitative understanding of periglacial processes and how these are affected by climate (Gruber et al. 2004; Andersen et al. 2015). I view current global warming as a process that will lead to significant changes in the frequency of hazardous surface processes and in hillslope sediment fluxes (Bartsch et al. 2009).

Given the challenge of gathering topographic and remotely sensed data in the Arctic, we lack a basic understanding of the spatial extent of landforms (Aalto et al. 2014). Quantifying the relationship between topography and landform process is a key challenge for periglacial geomorphologists. The effect of future climate warming on hazards and hillslope sediment fluxes depends on identifying regionally extensive periglacial landforms that are susceptible to warmer climates. To address this knowledge gap, periglacial geomorphologists are now turning to geographical information systems (GIS) to measure the spatial distribution of periglacial landforms (Luoto and Seppala 2002; Hjort and Luoto 2006; Marmion et al. 2008; Aalto and Luoto 2014; Aalto et al. 2014). These empirical studies have driven process-based and statistical models of topographic and environmental factors that govern periglacial processes (Bartsch et al. 2002; Luoto and Hjort 2005; Hjort et al. 2007; Marmion et al. 2008). However, only a few studies have been able to explore the impact of landforms on the topography of landscapes and their sediment budgets (Bartsch et al. 2008; Bartsch et al. 2009), the impact of current global warming on

the occurrence and spatial extent of landforms (Aalto and Luoto 2014; Aalto et al. 2014), and topographic controls on the physical process governing hillslope stability.

In this thesis, I seek to understand the spatial distribution of key mountainous Arctic landforms. I will use this to test hypotheses about the mechanism controlling the process of shallow translational landsliding in permafrost called active layer detachment (ALD) failure. This thesis focuses on two geographical areas: (1) I utilised remotely sensed data from Spitsbergen, Svalbard to create and develop a generalised periglacial landform model that can classify landscapes from topographic data. I chose Svalbard because of its high density of landforms in a small area (Andre 1997; Matsuoka and Hirakawa 2000; Prick 2003; Humlum et al. 2007; Harris et al. 2011; Siewert et al. 2012) and because it has one of the fastest warming regions in the Arctic (Harris et al. 2009). Additionally, many empirical studies provide information about periglacial processes on Svalbard (Matsuoka 2001a; Harris et al. 2011). (2) I used digital elevation models (DEMs) of the Brooks Range, Alaska to (i) test the classification model developed using the Svalbard data and (ii) create a physically based model of hillslope stability and to assess the impact of thawing permafrost on mass-wasting processes. I chose the Brooks Range because it has a landscape similar to Svalbard, it's within the continuous permafrost zone, and in the past decade, it has experienced warming events that have created mass-wasting landforms (Balser et al. 2009; Gooseff et al. 2009; Kokelj and Jorgenson 2013; Balser et al. 2015). As a result, I aim to test the following hypotheses:

H1: *The relative spatial distribution of periglacial landforms and their impact on sediment fluxes in mountainous Arctic landscapes can be quantified by automating the classification of landforms using topographic parameters derived from DEMs.*
Studies have shown how climate can have a profound impact on the erosion, storage, and deposition rates of periglacial landforms, impacting the sediment budget of landscapes (Matsuoka 2001a; Beylich 2008; Lewkowicz and Harris 2005a). To address

this at a regional scale, some studies have used a combination of remotely sensed data, field studies, and statistical analysis to model the distribution of landforms. There are few studies that have attempted to quantify the sediment flux of landforms on Svalbard (Hjort et al. 2014). This is important because Svalbard is an Arctic region already seeing rapid warming and geomorphological response to current global warming (Akerman 2005). Having a tool with which to quantify current and future sediment fluxes will help our understanding of the future topographic response to current global warming on Svalbard. Here, I develop a new tool for identifying periglacial landforms found in mountainous Arctic landscapes and apply this tool to regions on Svalbard. I then combine these data with process-rate information to estimate landform specific sediment fluxes.

H2: *Active layer detachments occur in convergent topography on soliflucting hillslopes.*

ALDs are a potentially hazardous Arctic process for which we have a limited understanding. Here I investigated whether there was a spatial control on the initiation of ALDs, and whether an improved understanding of their spatial extent can help map areas of potential ALD initiation. These shallow landslides initiate due to excess pore pressures along a shear plane between the base of a soil layer and the top of an impermeable layer such as permafrost or bedrock (Lewkowicz and Harris 2005b). In permafrost landscapes, water accumulates and freezes in regions of convergent topography known as water-tracks, where ground ice content can be found in excess of 60% (Trochim et al. 2016a). Balser et al. (2015) observed that ALDs initiate in water-track zones while Lewkowicz (1990) noted the occurrence of many ALDs on Ellesmere Island, Canada in convergent topography. However, not all landscapes fail, because there is an element of pre-conditioning relating to ground ice development from the previous year and to soil shear strength reduction by annual plug-like solifluction (Lewkowicz and Harris 2005a).

H3: *The spatial distribution of ground ice in the active layer and its location along the failure plain control hillslope instability.*

Hillslope instabilities such as ALDs occur in both continuous and discontinuous permafrost zones (Lewkowicz and Harris 2005a). During autumn freezing, in areas of continuous permafrost, the freezing front advances upward from the permafrost leading to a high concentration of segregation ice at the active layer-permafrost boundary (Mackay 1981; Harris and Lewkowicz 2000) with ice content of 30 and 40% by weight (Lewkowicz 1992).

After a review of key periglacial literature, the following thesis addresses the three hypotheses in three data chapters: (i) Chapter 3 presents the results of creating a supervised automated model for classifying DEMs into landforms found in mountainous periglacial environments as well as quantifying sediment fluxes; (ii) Chapter 4 investigates the spatial controls on ALD initiation; (iii) Chapter 5 explores the impact of different ice lens distributions in the active layer on the stability of a hillslope during thaw.

Chapter 2

Literature review

This literature review is focussed on both the development of our understanding of landform classification methods that form the basis of chapters 3 and 4, providing an overview of the range of Arctic landforms that form the basis of these classifications. Finally, the literature review provides an overview of the state of our current understanding of ALDs. This will be the basis for chapters 4 and 5.

2.1 Landform classification

2.1.1 Introduction

Being able to automate the classification of remote landscapes can provide valuable contributions to laboratory based research (Harris et al. 2001a; Harris et al. 2001b). Automated analysis of DEMs has provided a significantly improved understanding of the genesis and processes that govern the spatial extent of landforms across all geographical areas (Bolongaro-Crevenna et al. 2005; Barlow et al. 2006; Debella-Gilo and Etzelmüller 2009; Etzelmüller et al. 2001; Nishimura et al. 2009; Abellan et al. 2010; Prima and Yoshida 2010). Areas of permafrost and periglacial landforms have received less research than warmer landscapes, although there has been a

growing amount of recent work (Aalto and Luoto 2014; Hjort et al. 2014; Rudy et al. 2016; Rudy et al. 2017).

2.1.2 Historical overview of landform classification

Spatial analysis of landforms has been made possible due to (1) the availability of remotely sensed data and the ability to process this data in large quantities, and (2) the development of geomorphometry, the spatial modelling of topography using remotely sensed data and/or DEMs (Evans 1972; Dikau et al. 1995). Geomorphometry attempts to understand the relationship between surface processes and the topographic characteristics of landforms (Pike 1988). Topographic parameters including slope gradient, slope aspect, curvature, and topographic wetness index provide a basis for geomorphometric classification. Geomorphometry defines topographic regions based on different combinations of topographic parameters. These regions represent the dominance of certain surface processes (landforms) (Etzelmüller and Sulebak 2000; Etzelmüller et al. 2001). If an empirical or physical relationship can be established between topographic parameters and surface processes, a landscape can be classified into landform types (Etzelmüller et al. 2001).

Geomorphometric parameters of a landscape have been measured manually, classifying a landscape into landform features such as 'flat', 'hilly', and 'rolling' (Horton 1945) and are often the first or second order derivatives of elevation (Jasiewicz and Stepinski 2013). Hammond (1964) was among the first to experiment with using a combination of three geomorphometric parameters: (1) Percentage of area with flat or gentle ground with slopes <8%; (2) local relief (maximum – minimum elevation); and (3) profile type (relative proportion of flat or gently sloping terrain). From these three geomorphometric parameters Hammond (1964) was able to classify the continental United States into five landform features (plains, tablelands, plains with hills or mountains, open hills and mountains, and hills and mountains).

With the advent of GIS, Hammond's (1964) method was automated by Evans (1972) and Dikau et al. (1995). Pike (1988) took this further and introduced the concept of classifying a landscape by automating the generation of geomorphometric parameters, proposing that landform processes have a 'geometric signature'. Pike (1988) recognised that with the availability of DEMs and computer technology, the field of geomorphometry can move on from the vague classifications of Hammond (1964), to answering more fundamental questions about the processes that shape landscapes at regional scales. Current methods of landscape classification use a combination of geomorphometric parameters to determine the unique geometric signature of particular landforms (Evans 1972; Pike 1988; MacMillan et al. 2003; Jasiewicz and Stepinski 2013).

Today, geomorphometry has a variety of applications in the Earth Science community from mapping landslide distribution, groundwater movement (Armstrong and Martz 2003), and soil type (Debella-Gilo and Etzelmüller 2009) to volcanoes and craters on Mars (Stepinski and Vilalta 2005; Ghosh et al. 2010).

2.1.3 Pixel and object-orientated analysis

The classification of landforms using DEMs can be accomplished by using either pixel-based or object-oriented methods. Pixel-based methods assign a classification to each pixel, regardless of whether the classification applies to adjacent pixels (Irvin et al. 1997; Asselen and Seijmonsbergen 2006; Burrough et al. 2015). In contrast, object-orientated classifications group pixels by context and geometric signature, generating objects of different shapes and scale (Dragut and Blaschke 2006; Ghosh et al. 2010). Both methodologies rely on classifiers designed manually on the basis of expert knowledge and empirical evidence, called supervised classification (Iwahashi et al. 2001; MacMillan et al. 2003; Iwahashi and Pike 2007; Minar and Evans 2008; Ghosh et al. 2010; Iwahashi et al. 2012). Jasiewicz and Stepinski (2013)

developed a novel method using machine vision that they have termed 'geomorphons'. This is different to cell-based and object-based classifiers because it uses pattern recognition and is independent of scale, similar to how a trained geomorphologist would distinguish landform types from an aerial photograph.

2.1.4 Landform classifications of permafrost and periglacial landscapes

Our understanding of the interaction between process and form at a landscape scale in periglacial landscapes has improved over the past decade (Luoto and Hjort 2004; Hjort and Luoto 2006; Bartsch et al. 2009; Aalto and Luoto 2014). The wide knowledge gap between our understanding of form and process was highlighted by Barsch (1993), who described the analysis of processes as the major task in future periglacial geomorphological research. The initial work in the 1990s focussed on basic analysis of landforms, including understanding the altitudinal zonation of landforms in northern Sweden (Niessen et al. 1992). Linear discriminant analysis (LDA) of satellite imagery and DEMs was employed to provide an initial 'slope unit' classification for the Yukon Territory, Canada (Giles and Franklin 1998).

Analysis of different classification systems and parameters has provided a significant insight into both the spatial distribution of periglacial landforms in Arctic environments and the challenges and limitations of these geomorphometric methods (Etzelmüller and Sulebak 2000; Etzelmüller et al. 2001; Romstad 2001; Romstad and Etzelmüller 2012). This suite of papers assumed that the distribution of periglacial landforms can be described by relief parameters, thermal regime, soil moisture, and soil properties, all of which could be determined topographically (Etzelmüller et al. 2001). They demonstrate that by using logistic regression, solifluction could be classified based on its slope curvature, slope gradient and slope length (Etzelmüller et al. 2001). Romstad (2001) used contextual merging and iterative cluster analysis to clas-

sify debris cones on a slope in Ny-Ålesund, Svalbard using slope, profile curvature, planform curvature and topographic wetness index. Romstad and Etzelmüller (2012) mapped landform features using a terrain segmentation method, which subdivides a terrain surface into discrete 'terrain units' and applied this method across watersheds to create a mean-curvature map. The results of this method compared favourably with landforms mapped in Bolterdalen, Svalbard.

The geomorphological process unit (GPU) classification system was developed in Rabotsbekken, Northern Norway and Kärkevagge for Northern Sweden (Bartsch et al. 2002; Gurney and Bartsch 2005; Bartsch et al. 2008; Bartsch et al. 2009). A GPU is an area with homogenous processes that can be grouped on the basis of a single geomorphometric signature. This method recognises the challenge of separating landforms of similar geomorphometry, so each GPU can contain multiple landforms. GPUs can be classified using a combination of fieldwork, satellite imagery and DEMs such as slope gradient, slope aspect and profile curvature (Bartsch et al. 2002). Bartsch et al. (2009) is the only periglacial study to date that has attempted to quantify sediment transport processes at a catchment scale. A key finding of their research was that 680 t a^{-1} of sediment is moved from beneath rockwalls and 150 t a^{-1} is transported into the fluvial system.

Multiple logistic regression has been used to determine the distribution of palsas (peat mounds with perennially frozen cores), patterned ground, earth hummocks, sorted solifluction sheets and periglacial deflation sites (wind eroded bare ground sites in cold climates) in Finland (Luoto and Seppala 2002; Luoto and Hjort 2004; Luoto and Hjort 2005; Hjort and Luoto 2006; Luoto and Hjort 2006; Hjort et al. 2007; Hjort et al. 2010; Hjort and Luoto 2011; Hjort et al. 2014). Hjort et al. (2007) used logistic regression to determine that the key predictor variables for identifying these landforms are mean slope gradient, mean elevation, elevation-relief ratio, topographic wetness index, mean solar radiation, slope aspect, total curvature, and soil type. This classification was deemed successful for identifying palsas, earth

hummocks, and sorted solifluction sheets due to a high area under the curve (AUC) of 0.92 to 0.95. The AUC ranges from 0.5 for models with no discrimination ability to 1 for models with perfect discrimination. For example, a value of 0.9 for AUC means that the model can correctly discriminate between landforms 90% of the time (Hjort and Luoto 2006). Hjort and Luoto (2006) created six models, each of which used a different combination of topographic variables, ground type variables, and Landsat data. They determined that the key geomorphometric parameters were mean altitude, mean slope gradient, the proportion of concave topography, and mean of topographical wetness index. The classification was validated by splitting the data into a calibration set (70%) and an evaluation set (30%). Luoto and Hjort (2004) applied another variant of the suite of linear models, the generalised linear model (GLM). They justified the use of GLM because it enabled the analysis of non-linear relationships and different types of statistical distributions (i.e. they allowed for non-linearity and non-constant variance structures in data). This makes GLMs more flexible and better for analysing spatial relationships between landforms and surface form. They applied their classification to both satellite imagery and DEM data. They visually defined inactive and active patterned ground from satellite images and used five topographic parameters (mean altitude, mean slope gradient, topographic wetness index, flat topography (<2°), and profile curvature) to classify the probability of patterned ground occurrence. Their classifier correctly classified 76.9% of the area. Of the geomorphological parameters in the classifier, the topographic wetness index had the highest deviance i.e. it explained most of the variability in the classifier. Luoto and Seppala (2002) used a combination of land cover (water % and mire %), coordinates (north-coordinate and east-coordinate), and geomorphometric parameters (mean altitude, lowest point, highest point, and proportion of flat surface (<2°). They applied a multiple logistic regression to analyse the relationship between environmental variables and the distribution of palsa mires. They then developed a stepwise model to determine which environmental variables have the strongest

explanatory power. These suite of papers, (Luoto and Seppala 2002; Luoto and Hjort 2004; Luoto and Hjort 2005; Hjort and Luoto 2006; Luoto and Hjort 2006; Hjort et al. 2007; Hjort et al. 2010; Hjort and Luoto 2011; Hjort et al. 2014) identified suggestions for future studies that utilise the relationship between landform form and process, and including (1) testing grid-based models in different periglacial regions, (2) testing other physically environmental variables, (3) determining the interaction between environmental conditions and periglacial processes at different special scales (4) determine how periglacial processes will change with current global warming.

DEM data derived from topographic maps and/or Light Detection and Ranging (LiDAR) have become more widely available over the past decade (Showstack 2017). The advent of high-resolution DEM data has allowed landform-scale characterisation of topography (McKean and Roering 2004). One of the first geomorphological applications of high-resolution topography was the semi-automatic detection of earthflows (McKean and Roering 2004). This study defined a new topographic variable, which they called roughness, based on the eigenvalue ratios for the poles to individual pixels within a DEM. They demonstrated that earthflow terrain was rougher than the surrounding topography. Wavelet analysis has also shown significant success as an indicator of deep-seated landslides (Booth et al. 2009). Another study used a 2 m resolution LiDAR-derived DEM to assess the possibility of recognising topographic differences between earthquake-induced and rainfall-induced landslides. Iwahashi et al. (2012) calculated slope gradient and curvature at different moving window sizes, concluding that the optimal window size for detection of rainfall driven landslides is c.a. 30 m. Prima et al. (2006) successfully distinguish different landforms (volcanoes, alluvial fans, alluvial plains, mountains, and hills) using DEM derivatives (slope gradient and topographic openness). Object-oriented methods have also been applied to recognise deep-seated and shallow landslides (Barlow et al. 2006; Van Den Eeckhaut et al. 2012).

Nested modelling using a suite of different model structures provides insights into the accuracy of different methods. Combining statistical and process-based modelling approaches may provide useful insights into the relative importance of different techniques. Marmion et al. (2009) combined eight modelling techniques using nine environmental parameters (including geomorphometric parameters) to predict probabilities of occurrence of twelve landform processes in a periglacial landscape, northern Finland. Individual models produced AUC values of 0.71 to 0.76 while the proposed combined method produced values of 0.75 to 0.78 (Marmion et al. 2009). However, the issue with these studies is that they don't make the link between the model output and landform processes i.e. they don't explain why certain geomorphometric parameters are the best predictors for some landforms and not for others.

Hjort et al. (2014) investigated model transferability between different periglacial landscapes. Their study tested the transferability of three statistically-based models of the distribution of solifluction models: a generalized linear model, a generalized additive model, and a maximum entropy model between six study sites (Adventdalen and Kvadehuksletta on Svalbard, Paistunturit in Finland, and Kåfjord, Nordre Andøya, and Mållejus in Norway). They concluded that the best performing models were those calibrated in regions with a wide range of topographic conditions, for example, in slope gradient or elevation. This made the model sensitive to the location in which it was developed. For solifluction, the most important predictor variables were slope gradient, mean annual air temperature, and an index of vegetation abundance. It seems that altitude (as a proxy for air temperature) and slope gradient (as a proxy for potential energy) are the most commonly used geomorphometric parameters in periglacial studies (Etzelmüller et al. 2001; Hjort and Luoto 2006). Some studies have concluded that simple models such as generalized additive models and logistic regression performed equally when compared to more complex machine-learning techniques (Brenning 2005; Vorpahl et al. 2012).

2.2 What is permafrost?

Permafrost is defined as any material (rock or soil) that remains below 0°C for more than two consecutive years (French 2007). This is a thermal definition and there is no relation to the absence or presence of ground ice. Ground ice can form within a range of subzero conditions (Ballantyne and Harris 1994). Permafrost covers 12.8% to 17.8% of Earth's land surface area, most of which is in the northern hemisphere (Figure 2.1) (Zhang et al. 2000; Gruber 2012).

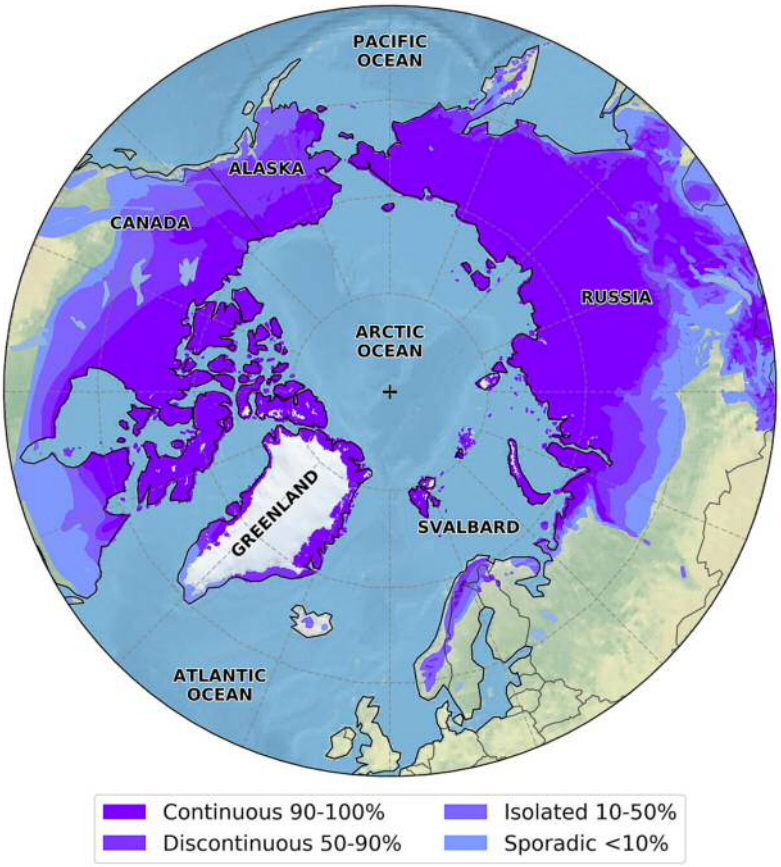

Figure 2.1 Map showing the spatial extent of permafrost in the northern hemisphere. Permafrost distribution data from Brown et al. (2002a).

The thickness of permafrost below the ground surface is influenced by the balance between the amount incoming solar radiation at the surface and the heat loss from the Earth's interior (Anderson and Anderson 2010). A number of factors impact surface temperatures; latitude, altitude, and continentality (Anderson and Anderson 2010).

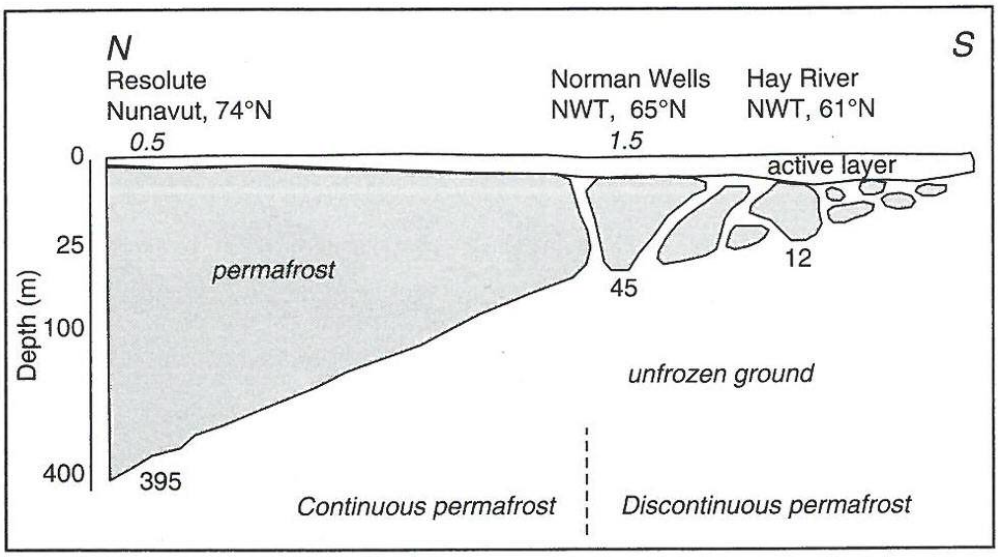

Figure 2.2 Cross section through permafrost in northern Canada. Permafrost thickens and the active layer thins with increasing latitude. Adapted from (Anderson and Anderson 2010).

At higher latitudes, solar radiation passes through a greater thickness of atmosphere, resulting in a lower mean solar radiation per unit area. Also, air temperatures decrease with increasing altitude, known as the environmental lapse rate which averages 6.5°C km^{-1} (Anderson and Anderson 2010). Hence permafrost can exist at lower latitudes, but also at higher altitudes, for example in the Tibetan Plateau (Niu et al. 2015). Continentality impacts the seasonal temperature distribution so that the further away an area of land is from the ocean the greater the annual air temperature variation it experiences. The geothermal gradient ultimately governs the depth of permafrost and this is controlled by the thermal conductivity of the ground; on average the geothermal gradient is 25°C km^{-1} (Figure 2.3) (Anderson and Anderson 2010). The balance between the above creates a patchy development of permafrost in areas (Figure 2.2). The continuous performs zone exists at the highest latitudes where >90% of the land surface is underlain with permafrost. Discontinuous permafrost is where 50% to 90% of the surface is underlain by permafrost. Sporadic permafrost is where 10% to 50% of the land surface is underlain by permafrost and areas with <10% permafrost are called isolated permafrost (French 2007). A general trend is for

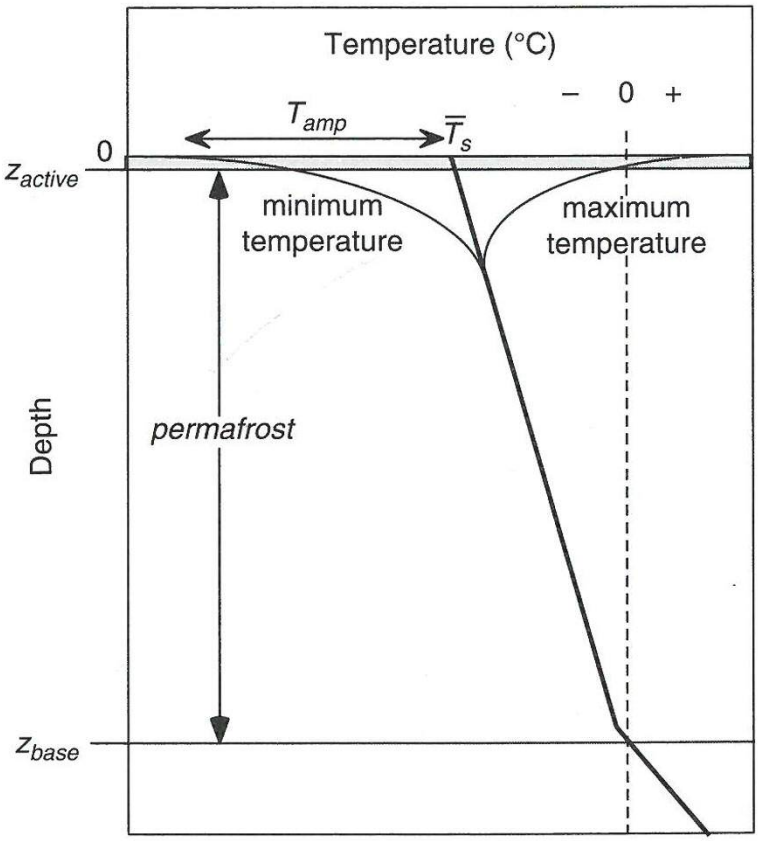

Figure 2.3 Plot showing the temperature profile through permafrost. Z_{active} is the depth of the active layer, T_{amp} is the temperature amplitude from the mean annual surface temperature, $\bar{T}_s$. Z_{base} is the base of the permafrost. Adapted from Anderson and Anderson (2010).

permafrost to thicken and become more continuous with increasing latitude (French 2007) (Figure 2.2).

2.2.1 Permafrost Structure

Ground underlain by permafrost can be divided into three layers: the active layer; the transition zone; and permafrost (Shur et al. 2005) (Figure 2.4). The active layer is the top ground layer that freezes and thaws seasonally. Its maximum depth is defined as the depth at which the annual maximum temperature reaches 0°C (Figure 2.3). The depth of the 0°C isotherm is dependent on the mean annual surface temperature (Figure 2.3). However, the 0°C depth is driven by changes in

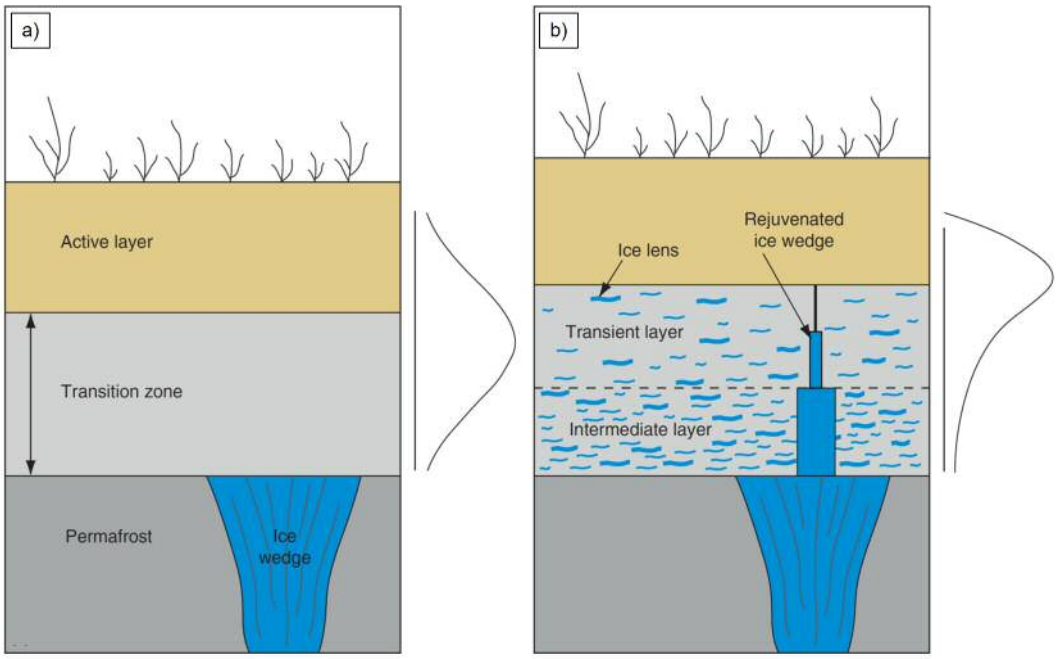

Figure 2.4 Diagram showing the three-layer model of the active layer, transition zone, and permafrost. The curve on the right of each figure represents the relative probability of annual thaw depth. a) Thawing a sub-decadal to centennial timescales. b) Ice-enrichment of the transition zone. Modified from Shur at al. (2005) and Murton (2013).

ground temperatures caused by interannual variations and climatic fluctuations in air and ground surface temperatures (Anderson and Anderson 2010). The base of the permafrost is reached at the depth at which ground temperature is 0°C (Figure 2.3). Where the top of the permafrost is within the range of -5°C to 0°C it is termed 'warm' permafrost. However, if the top of the permafrost is <-5°C it is termed 'cold' permafrost (Ballantyne 2018).

At the boundary between the active layer and permafrost, there is a region where ground ice is concentrated, called the transition zone (Figure 2.5) (Shur et al. 2005). The development of the transition zone is more pronounced in frost-susceptible soils in lowland Arctic regions underlain by cold permafrost (Ballantyne 2018). Here, this concentration of ice, called excess ice, tends to be in the form of segregated ice. The transition zone is composed of two parts: an upper ice-rich layer called the transient layer and, beneath this, is an even more ice-rich layer called the intermediate layer (Figure 2.4) (Shur et al. 2005). Over sub-decadal to centennial time scales the

Figure 2.5 Image of the ice rich transition zone of segregated ice (white). Adapted from (Murton 2013).

transition zone alternates between being seasonally frozen ground (active layer) to perennially frozen ground (permafrost) (Murton 2013). This occurs because of short and long-term changes in subsurface thermal conditions caused by abnormally warm or cold summers and/or because of changes in climate. The base of the transition zone reflects the long-term permafrost table and is defined by thaw unconformities such as truncated tops of ice wedges or by sudden changes in excess ground ice content (Figure 2.4) (Murton 2013). Because of its high ground-ice content, the transition zone acts as a thermal buffer between the active layer and the long-term permafrost by increasing the latent heat required to thaw the ice (Ballantyne 2018).

Ice enrichment within the transition zone occurs because of a combination of two mechanisms. First is the upward aggradation of permafrost into the active layer, either syngenetically as sediment and organic material accumulate on the surface, or epigenetically as atmospheric cooling or biological/hydrological changes lower the surface ground temperature (Murton 2013). As permafrost aggrades upwards towards

the surface and the permafrost table rises, ice lenses that formed at the base of the active layer become incorporated into the top of the permafrost (Figure 2.6). Second, is the repeated growth of segregation ice from the unequal and seasonal movement of unfrozen water into the transition zone (Figure 2.7) (Murton 2013). During autumn freeze-back of the active layer, water is drawn both upward by colder temperatures at the ground surface and downward toward the permafrost to feed the growth of segregated ice, called two-sided or bidirectional freezing (Figure 2.7). In winter, after the active layer has frozen through, the ground surface becomes colder than the permafrost creating a thermal gradient which encourages water migration toward the surface by cryosuction. However, during winter, the rate of water movement by cryosuction is limited by the low permeability of the frozen active layer (Figure 2.7). In summer, the unfrozen active layer enhances water movement because of high hydraulic conductivity and an open hydrological system. This allows for easy

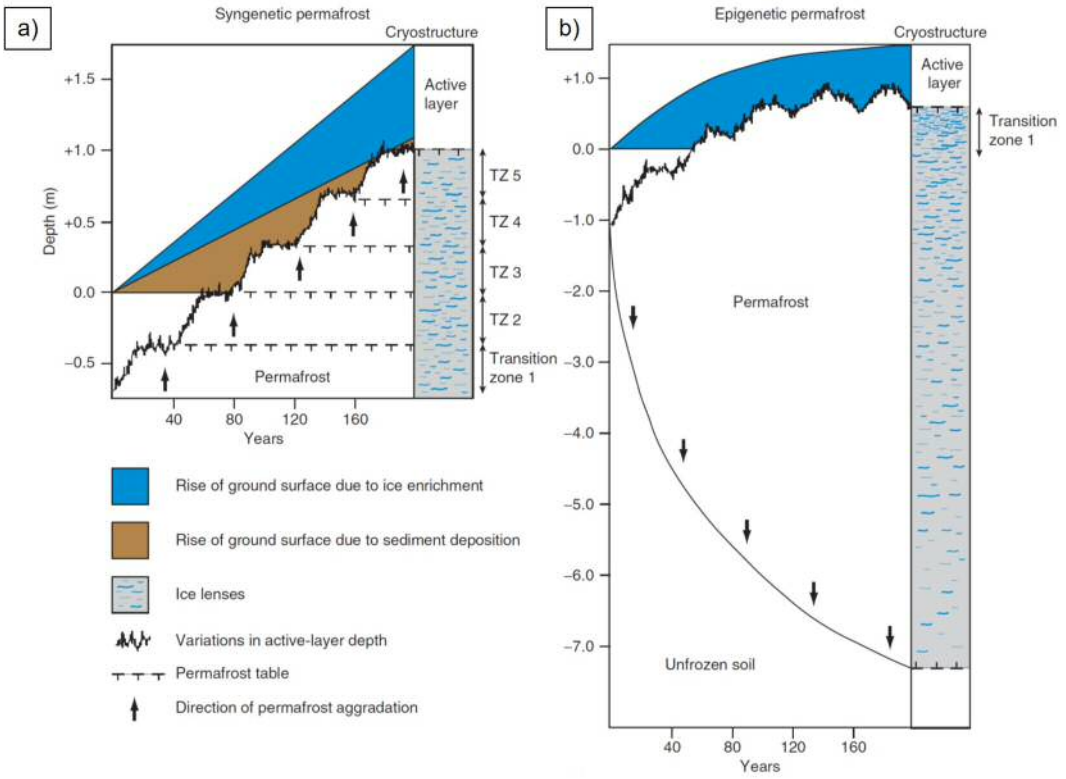

Figure 2.6 Development of the transition one during a) syngenetic and b) epigenetic permafrost formation (French and Shur 2010; Murton 2013).

downward movement of water supplied by melting ice lenses, snowmelt, rain, and groundwater flow which saturates the base of the active layer. Colder permafrost temperatures draw water, by cryosuction, from the base of the active layer and into the transition zone (Ballantyne 2018). This renews and promotes ice segregation within the upper layers of permafrost, contributing to the progressive ice enrichment in the transition zone. The intermediate layer is more ice rich than the transient layer because in the long term it is thermally more stable i.e. it remains cold for longer. The transient layer on the other hand is subject to more frequent thaw events, giving less time for ice to accumulate. In summary, the amount of water (ice) added to the top of the permafrost during summer is greater than the amount added to the top of the active layer during winter, which progressively enriches the transition zone (upper layer of permafrost) in segregation ice. Evidence supporting the ice enrichment of the transition zone comes from field experiments by Burn (1988), who monitored ice-lens growth over a period of fifteen months in the upper 20 cm of permafrost in the Yukon Territory, Canada. The study observed an increase in ice content during the summer months. In addition, the study found that the rate of water incorporation into the upper layers of permafrost during the last 8000 years

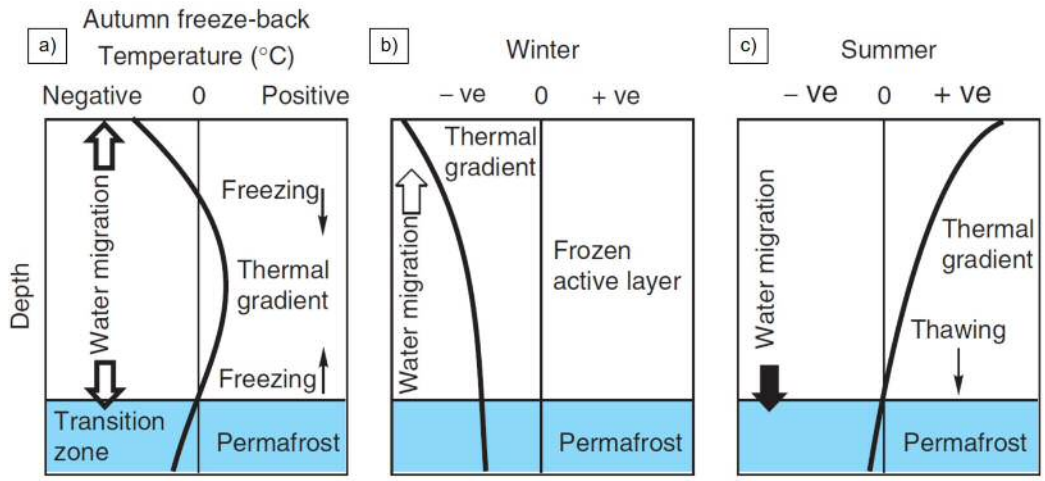

Figure 2.7 Conceptual model showing the movement of water in the active layer, transition zone, and permafrost layers during a) autumn freeze-back, b) winter, and c) summer (Murton 2013).

has been between 0.1 to 0.2 mm a^{-1}. To further support the ice enrichment of the transition zone, Burn and Micheal (1988) observed elevated tritium levels in ground ice below the current permafrost table. The elevated tritium is a marker for nuclear weapons testing during the 1950s and 60s, thus some ground ice must be derived from atmospheric precipitation that migrated downward through the active layer during this period, contributing to recent ice enrichment of the transition zone.

2.2.2 Segregation ice

Figure 2.8 Segregation ice collected by drilling into the transient zone of permafrost in Adventdalen, Svalbard. The silt is brown material in between the opaque segregated ice. Photo by Murton (2013).

Permafrost often contains lenses of pure ice called segregated ice lenses (Figure 2.8). These ice lenses were first recognised by Taber (1929), who demonstrated that they develop not by the volumetric expansion of water, but by the movement of water across an underlying frozen fringe (Figure 2.10). The mechanism driving the formation of segregated ice lenses has been well described by Rempel et al. (2004).

They demonstrated that a suction force was created by the forces generated at the interface between ice and solid material (either sediment or rock). Here, van der Walls and electrostatic forces generated at the ice surface, create a thin, unfrozen (premelted) film of water whose thickness decreases with temperature (Rempel 2007) (Figure 2.9). Rempel et al. (2004) calculated the force balance of the water inside these premelted films, demonstrating that lower water pressures generated at lower temperatures drove the suction of water through these films. Hence, segregated ice lenses form where there is a freely available source of water and a suitably strong temperature gradient (Rempel et al. 2004). These growing ice lenses heave apart the adjacent soil and rock causing ice lenses to become 'segregated' from the surrounding material (Murton 2013) (Figure 2.8), hence the term segregation ice. Ice

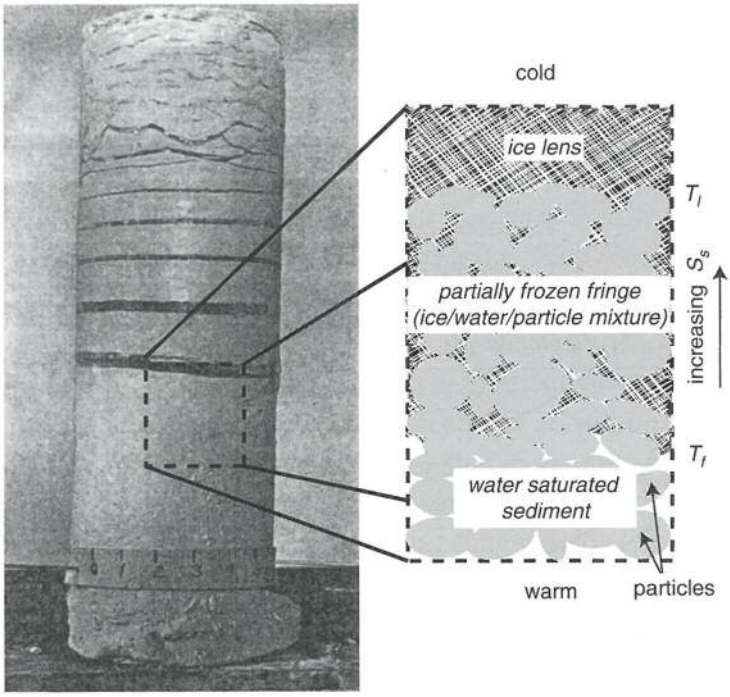

Figure 2.9 Frozen silt with ice lenses (shown as dark bands), an experiment conducted by Taber (1930). The diagram on the right depicts the transition from unfrozen saturated water content across the partially frozen fringe to the ice lens at the top. T_f is the freezing temperature of water, T_l is the temperature at the base of the ice lens, and S_s is the ice saturation, the volume fraction of the pore space occupied by ice. Figure adapted from Anderson and Anderson (2010).

lenses grow parallel to the freezing front making them horizontal on a flat surface and inclined beneath a slope (Murton 2013). Their volumetric expansion and resultant heaving pressures are exerted normal to the ground surface, i.e. in the direction of heat flow (Murton 2013). This process is known to concentrate ice at the base of the active layer and in the transition zone (Burn and Kokelj 2009) (Figure2.11).

The lateral extent of ice lenses depends on the homogeneity of the surrounding soil and the uniformity of the water supply (Smith 2004). If the freezing front advances from the surface downwards, i.e. in discontinuous permafrost zone, then water will migrate upwards against gravity to contribute to the growth of ice lenses near the surface (single-sided freezing) (Harris et al. 2008a) (Figure 2.20). It is common in continuous permafrost regions, during autumn freezback, for freezing fronts to advance from the surface down and from the top of the permafrost upwards, called two-sided freezing (Harris et al. 2008a) (Figure 2.20). In this case, a zone of desiccation forms in the middle of the active layer where water has migrated to both areas of freezing at the top and bottom of the active layer (Harris and Lewkowicz

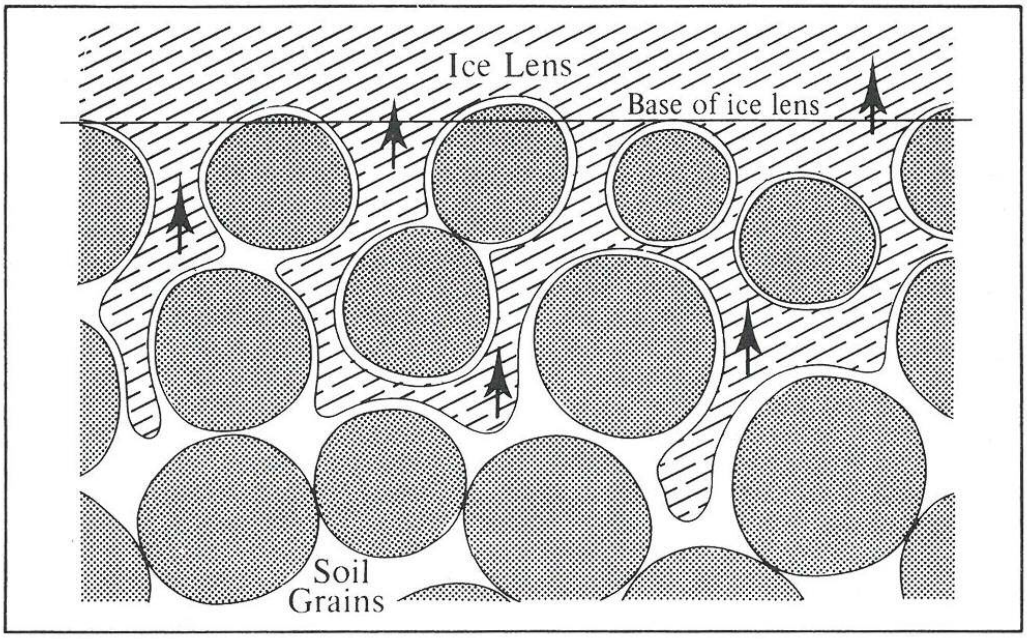

Figure 2.10 A schematic diagram of the frozen fringe. Arrows represent direction of water movement. Adapted from Williams and Smith (1989).

2000). Due to the growth of ice lenses moisture is re-distributed, locally increasing the water content of the base of the active layer (Mackay 1981). As a result it is common for the ice volumetric content to exceed pore space in areas of ice lens growth (Harris et al. 2011) (Figure 2.11). It is the growth of these ice lenses that causes the soil above to expand upward normal to the surface, termed frost heave (Harris et al. 2008b). Layers of ice lenses have a range of thicknesses from <1 mm to >10 m and can be millimetres to hundreds of metres in length (Murton 2013). Generally, ice lenses with a thickness >1 m are termed 'massive ground ice' (Murton 2013).

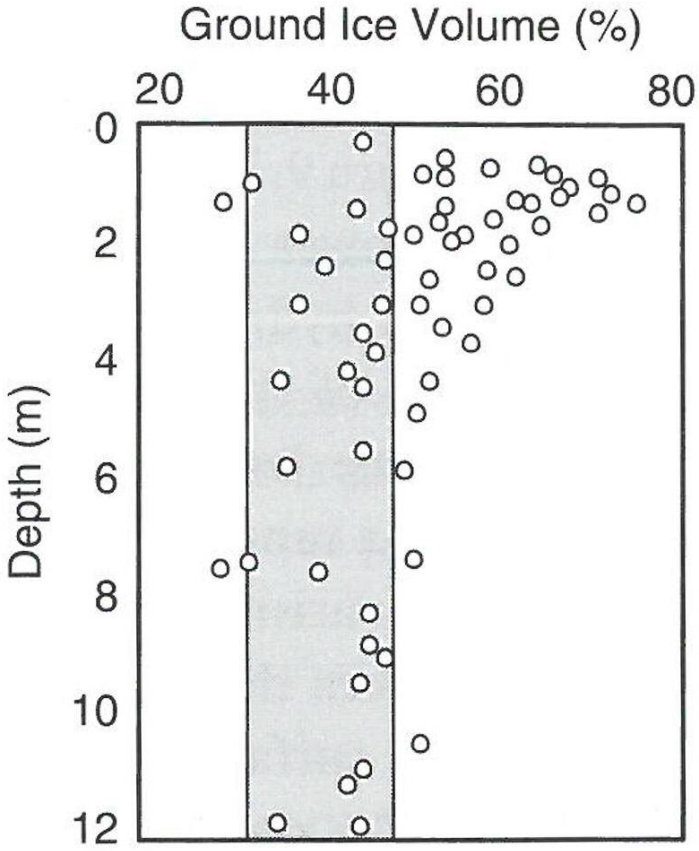

Figure 2.11 Plot showing ground ice volume as a function of depth. Note a higher volume of ground ice near the surface c.a. 1 m. Adapted from Anderson and Anderson (2010).

2.2.3 Frost-susceptibility

Soils that are porous and fine-grained, typically silty-clays, are prone to the growth of segregation ice and are termed frost susceptible (Williams and Smith 1989)(Figure 2.12). A frost susceptible soil usually contains >3% silt content (Anderson and Anderson 2010). The pore spaces in fine-grained soils such as clays and silts are so small that they prevent pore ice from forming, like a semi-permeable membrane (Williams and Smith 1989). Silt has a mid-range of capillarity. Capillarity controls the amount of surface tension between the soil particles and water surface. Where capillarity is too low water can't migrate to growing ice lenses by cryosuction. Permeability is the a measure of ease by which water can flow through soil and is dependent on particle size. The bigger the particles, the larger the voids are between them, allowing more water to migrate. Silt has a mid-range of capillarity and permeability to allow for enough water to migrate by cryosuction to feed the

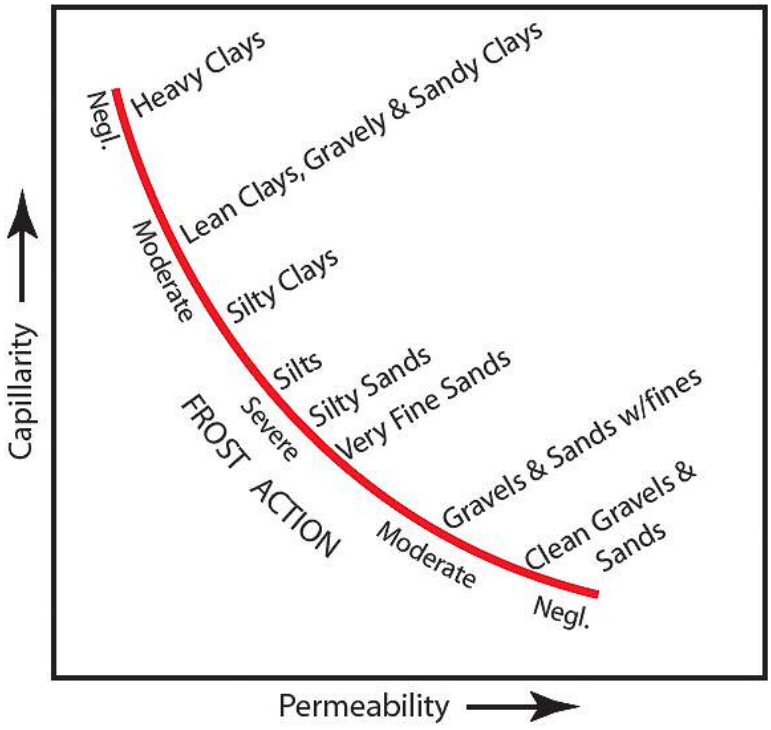

Figure 2.12 Plot showing how the hydraulic properties of different soil types impact their susceptibility to frost action. Adapted from Table (2008)

growth of ice lenses (Figure 2.12). In contrast, non-frost susceptible materials such as sands and gravels exhibit low cryosuction on the larger grain surface, preventing the movement of water by cryosuction (Anderson and Anderson 2010). In this case, water freezes in the pore spaces, creating pore ice where no heaving occurs. In clay soils, the growth of ice lenses is stunted because of their low permeability making it is difficult to maintain sufficient water flux by cryosuction to the zone of freezing (Harris 1981). The temperature range in which water remains liquid below 0°C is greater in fine-textured soils. Sand has no unfrozen water at -4°C while clays and silts still have liquid water (Anderson and Anderson 2010) (Figure 2.13). This means that in permafrost regions where the ground temperature falls below 0°C there is a supply of unfrozen water to feed the growth of ice lenses in silty soils. The movement

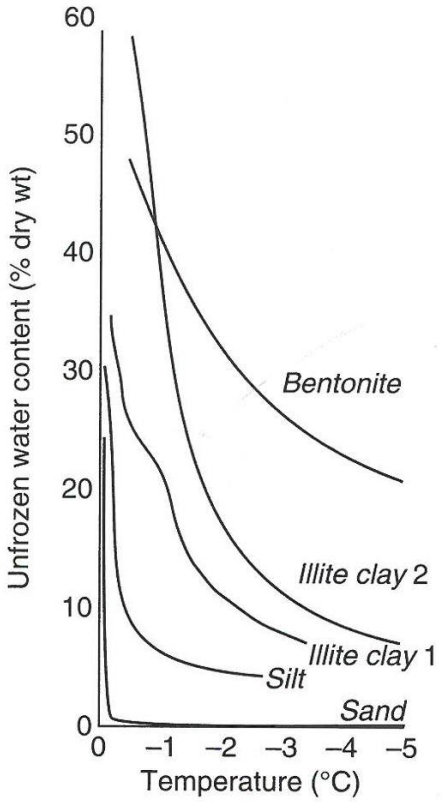

Figure 2.13 Plot showing the amount of water found in different soils at temperatures below 0°C. Adapted from Anderson and Anderson (2010).

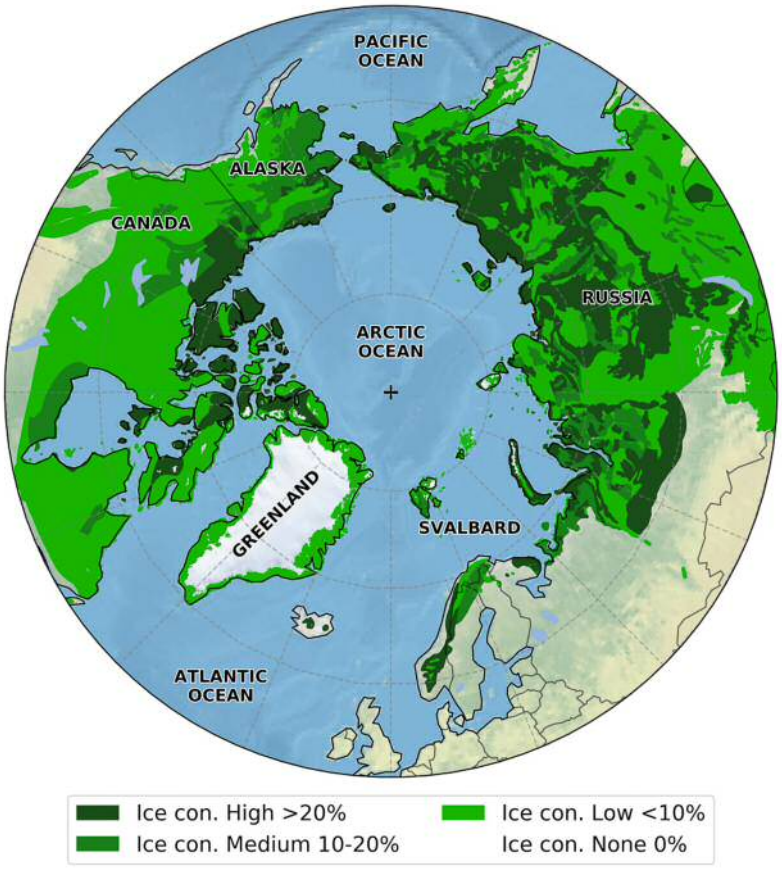

Figure 2.14 Map showing the ground ice content by volume in the upper 20 m of permafrost. Data from Brown et al. (2002b).

of water in the active layer is unequal when comparing the freezing and thawing season. During a summer thaw, more water migrates downwards to the bottom of the active layer/top of permafrost than migrates upward during autumn freezback (Williams and Smith 1989). In the summer a greater unfrozen water content exists because of increased hydraulic conductivity and a supply of water from thawing ice lenses, melting snow, rain, and groundwater flow (Smith 2004). By contrast during autumn freezeback, when two-sided freezing occurs, the movement of water is restricted upwards by reduced hydraulic conductivity from lower temperatures and where water movement migrates against gravity by cryosuction (Anderson and Anderson 2010). This causes a preferential accumulation of pore and segregated ice

at the base of the active layer or top of the permafrost (Shur et al. 2005). However, ice lenses still form at the top of the active layer (French 2003).

2.2.4 Thaw consolidation

Thaw consolidation is the time-dependent compression of soil caused by the thawing of segregated ice, and the subsequent drainage of pore water (McRoberts and Morgenstern 1974). There are three main components to thaw consolidation: (1) reduction in soil ice volume during melting; (2) reduction in soil pore sizes as collapsing voids left by segregated ice squeeze soil grains closer together; (3) drainage and expulsion of pore-water and excess water from soil pores generated by thawing ice lenses. Thaw consolidation is non-existent in coarse-grained soils such as sand because excess ice such as ice lenses are absent or minimal. In frost-susceptible fine-grained soils such as silts, thaw consolidation occurs because of the presence of excess ice (Ballantyne 2018).

Thaw consolidation causes a reduction in soil strength which leads to slope instability. During a thawing event, the upper soil layers thaw first creating a low-permeable layer that limits the rate of water drainage from the soil below. When the rate of water released (due to thawing of excess ice) is greater than the rate of water drainage, the weight of the overlying thawed soil (W) is transferred from grain-to-grain contact to trapped soil water. This raises pore-water pressure (u) and reduces the soil's effective stress (σ'), and therefore its strength (McRoberts and Morgenstern 1974)

$$\sigma' = W - u = \gamma z_t - u \tag{2.1}$$

where γ is the unit weight of thawed soil and z_t is the depth of thawed soil. The strength of a thawing soil is therefore dependent on the ratio of the rate of water released from melting excess ice, to the rate of water drainage through the now

thaw-consolidated soil. This can be described using the thaw consolidation ratio (R) (McRoberts and Morgenstern 1974)

$$R = \frac{\alpha}{2\sqrt{C_v}} \tag{2.2}$$

where α, a thaw parameter, is derived by (McRoberts and Morgenstern 1974)

$$\alpha = \frac{z_t}{\sqrt{t}} \tag{2.3}$$

where z_t is the depth of thaw and t is time passed since the onset of thaw at the ground surface. C_v is the coefficient of consolidation and is given by

$$C_v = \frac{k}{p_w m_v} \tag{2.4}$$

where k is the permeability of the thawed soil, p_w is the density of water, and m_v is the coefficient of compressibility. A high value of R indicates rapid thaw and/or slow drainage of water released from melting ice, generating high pore pressures (Ballantyne 2018). This situation is associated with fine-grained silt or clay-rich soils with low permeability and high excess ice content. A low value of R suggests a slow thaw and/or rapid drainage of water, producing low pore pressures. This is likely with uniformly coarse-grained sandy soils that contain little or no excess ice (Ballantyne 2018).

Relatively higher R values reflect the greater likelihood of slope failure. If the rate of thawing is fast enough and the C_v parameter sufficiently small, meltwater is generated faster than can drain (Smith 2004). This creates a scenario where all of the overburden pressure from the soil above is supported by pore water rather than grain-to-grain contact (Smith 2004). This can lead to slow downslope mass-movements (solifluction) but is also linked to rapid slope failures such as ALDs.

2.3 Periglacial landforms

2.3.1 Blockfields

Blockfields are veneers of coarse regolith mantling plateau surfaces (Ballantyne 2010). They occupy areas of low gradient found at mountain summits or plateaus and are formed by in situ weathering of underlying bedrock (Goodfellow 2007) (Figure 2.15). Allochthonous blockfields comprise of material derived from up-

Figure 2.15 Blockfield on the Gruvefjellet plateau at 500 m a.s.l. Photo © Huw Mithan.

freezing of clasts in till or by the downslope movement of weathered material (Goodfellow 2007). Autochthonous blockfields develop through weathering of bedrock with a negligible downslope displacement of weathered debris (Ballantyne 2010). Rea (2007) demonstrated that the transport mechanism defines the character of the landform as transport distances increase. The formation and preservation of blockfields are controlled by slope gradient because as slope gradient increases the downslope shear stress acting on each clast/particle increases (Rea 2007; Rixhon and Demoulin 2013). An upper slope gradient limit of 25° was reported by Dahl (1966), beyond which scree slopes formed. In general, plateaux blockfields form on slope gradients of <10° (Rea 2007). As slope gradient increases blockfields become

more open-work because of the removal of fine-grained matrix sediments (Rea et al. 1996). At lower slope gradients fine material will collect and be retained. These finer fractions are partly derived from chemical weathering producing particle sizes below the crystal size of the parent bedrock; these fines enriches the matrix with silt (2 to 63 μm) and clay (<2 μm) (Rea 2007).

Blockfields form in periglacial regions underlain by permafrost because of frost cracking of bedrock (Ballantyne 2010). Drainage is impeded at the blockfield base because of impermeable permafrost, allowing for saturation of the bedrock or blockfield clasts. With a moisture source and low mean annual air temperatures, ice lenses can grow by upward freezing from the permafrost (Ballantyne 2010). However some have challenged the primacy of frost shattering because of (1) the presence of blockfields in arid, non-periglacial environments such as the Namibian desert (Goodfellow 2007); (2) the possible role of thermal stress and shock from diurnal and/or seasonal variations in surface rock temperatures, (3) and possibly the effect of chemical weathering, in providing fines that could result in movement by plug-like deformation over impermeable permafrost (Boelhouwers 2004). Current research indicates that there is no current formation of new blockfields from exposed bedrock, leading to the suggestion that the majority of blockfields are pre-Quaternary in origin (Boelhouwers 2004).

2.3.2 Bedrock exposure

The presence of bedrock is a common feature of alpine and upland Arctic landscapes, yet is often relatively sparse, particularly in highly fractured or porous rock types (Hales and Roering 2007). Bedrock which has a high moisture content and is highly porous is frost susceptible (Murton et al. 2006).

Prick (2003) conducted a study on the frost weathering of an outcrop of sandstone, siltstone, and shale bedrock exposed during the construction of a road from the airport

Figure 2.16 Frost shattered bedrock overhanging the Endalen valley. Photo © Huw Mithan.

to Longyearbyen, Svalbard. The study found that the porosity of the sandstone in this formation was low, making it not frost susceptible. Shattering of bedrock is commonly seen in these landscapes, and recent work has focussed on possible mechanisms for this (Hallet 2006). The most commonly stated hypothesis is that shattering is driven by the 9% volumetric expansion from the in situ freezing of water occupying joints or pore spaces. However, this requires a high saturation level of >90% (Hallet et al. 1991). The second explanation is segregation ice growth (Walder and Hallet 1985; Hallet et al. 1991; Hallet 2006), where ice lenses growing within pore spaces drive strong tensile forces and growth of crack tips. For this to happen requires an upward advance of the freezing front at the beginning of winter (low mean annual air temperatures of between -3°C to -8°C frost cracking window), a continuous downward water supply in the summer (from melting snow patches or cornices) and a high porosity allowing movement of the water supply through the bedrock too the freezing front (porous sedimentary bedrock) (Walder and Hallet 1985; Hales and Roering 2007). Field evidence in porous sedimentary bedrock and laboratory experiments show that ice segregation is likely to be the dominant frost

weathering mechanism responsible for shattering porous sedimentary rock (Hales and Roering 2005; Murton et al. 2006). The volumetric expansion is thought to be a minor influence because the growth of pore ice in an open system exerts little outward pressure onto the pore wall (Anderson and Anderson 2010). However, some studies have shown that the volumetric expansion of water upon freezing in cracks is a mechanism for crack enlargement and block detachment (Matsuoka 2001b; Matsuoka 2008).

Cornices have been identified as areas of enhanced frost weathering on mostly snow-free rock faces (Rapp 1960a; Eckerstorfer et al. 2013). It is thought that prior to autumn freeze-back, rain supplies moisture to the cornice backwall and maintains moisture in the pore spaces and cracks before cornice accretion. Snow insulates the frozen ground keeping the ground temperature stable and within the frost cracking window (Eckerstorfer et al. 2013) (Figure 2.16). Water supplied from snow is thought to be a significant control on bedrock weathering of rock walls (Matsuoka 1990; Sass 2005).

Field (Prick 2003) and laboratory (Murton et al. 2000; Murton et al. 2001; Murton et al. 2006) experiments of frost weathering have attempted to constrain frost weathering processes. Frost weathering tests on blocks of local sandstone in Longyeardalen, Svalbard demonstrated no shattering during eighteen months of exposure (Prick 2003). The short-term nature of this study demonstrated unfavourable conditions for frost weathering, as the rocks need a longer exposure time, a greater moisture content, and the local sandstones are low porosity making them less frost susceptible (Prick 2003). Matsuoka (2008) demonstrated that a moisture source is important for rockwall weathering. Boulders and bedrock were rapidly fractured along lakes and streams because these rocks were saturated before seasonal freezing (Matsuoka 2008). The intensive shattering of rocks occurs along lakes and streams where high moisture availability promotes ice segregation (Matsuoka 2008). Matsuoka (1990) concluded that moisture was insufficient for frost shattering on Svalbard.

2.3.3 Allochthonous material and scree

Scree, or talus, are landfroms representing the accumulation of rockfall debris (Kirkby and Statham 1975) (Figure 2.17). The proximal scree slopes are rectilinear, with slope gradients ranging from 30° to 40° and become concave and shallower at the distal end of the scree slope between 20° to 10° (Sanders 2010). As scree slopes

Figure 2.17 Allochthonous and scree material on the east-facing slopes of Endalen. Note the bedrock at the top of the slope and gullying of deposited material © Huw Mithan.

aggrade, they steepen at the proximal end and prograde at the distal end (Sanders 2010). Their surface is composed of angular-cobble to boulder-sized clasts. There is a sorting gradient of finer surficial material at the top and coarser surficial material at the bottom caused by fall sorting (Statham 1976). (Kirkby and Statham 1975; Statham 1976) . Once supply of upslope material reduces, scree slopes become vegetated. Rapp (1960b) noted that vegetation grew on scree slopes because of moisture form upslope, micro-climate and development of fine-grained soil cover.

Rockfall is the primary process producing scree slopes (Fisher 1866). Rockfall onto talus slopes is either primary, i.e. triggered by freeze-thaw activity on the rock face and subsequent downslope transfer of newly detached material, or secondary, i.e.

rockfall debris is dislodged by later rockfall events, snow avalanches, water runoff, debris flows, or even cornice collapse (Hales and Roering 2007; Hales and Roering 2009; Eckerstorfer et al. 2013). Rock-cliff faces are often dissected and complex, resulting in debris being channelled into accumulation corridors that open downslope into talus cones (Siewert et al. 2012). Smaller rocks and finer material deposited onto the talus slope surface are washed or trapped in the interstitial voids between larger clasts (Hinchliffe et al. 1998). Other mechanisms of downslope sediment transfer include rockfall impact, dry avalanching, translational sliding, solifluction, snow avalanches, debris flows, and surface runoff (Anderson and Anderson 2010). The fine material can also be moved downslope by needle-ice creep and upper rectilinear slopes are often reworked by debris flows (Hinchliffe et al. 1998).

On Svalbard, Akerman (1984) found that scree accumulations were made of a layer of coarse debris overlying a poorly sorted diamicton with an abundance of fine-grained sediments. In Longyeardalen, Svalbard these accumulations ranged from 18 m to 34 m (Siewert et al. 2012). The finer sediment within scree originated from granular disaggregation (flaking and granular weathering) of the rockwall above (Curry and Black 2003; Hinchliffe et al. 1998; Hinchliffe and Ballantyne 1999).

2.3.4 Alluvial fans and braided rivers

Alluvial fan activity in the Arctic is limited to the spring and summer months because fan surfaces are frozen during winter (Haas et al. 2015) (Figure 2.18). Geomorphological activity is highest during the melting season from snowmelt, glacier melt, rainfall, thawing ground ice (Haas et al. 2015).

The supply of material for alluvial fans includes outwash from glaciers, re-sedimentation of glaciogenic deposits and debris from frost weathered bedrock cliffs (Anderson and Anderson 2010). Arctic alluvial fan sedimentation involves streamflow, debris flow processes, and sporadic snow avalanches. De Haas et al.

Figure 2.18 An alluvial fan at the mouth of Kosladalen, Svalbard. Note the braided river system and floodplain of Adventdalen in the bottom right. Photo © Huw Mithan.

(2015) identified three types of 'fans' on Svalbard: (1) Colluvial fans formed by snow avalanches and rockfalls; (2) alluvial fans dominated by debris flows; and (3) alluvial fans formed by fluvial flows. In this study I will focus on alluvial fans formed by fluvial flows (Haas et al. 2015).

2.3.5 Solifluction

The term 'solifluction' (Figure 2.19) was originally coined by Andersson (1906) to describe the slow downslope movement of saturated soil. Washburn (1980) coined the term 'gelifluction' to describe the movement of the saturated active layer after and during a seasonal thaw. Solifluction also incorporates frost creep driven by the growth and thawing of segregated ice (Washburn 1980). The landform associated with solifluction sediment in this study is usually termed a solifluction sheet.

The growth of segregated ice causes the ground to heave normal to the slope during the winter, and consolidate vertically during thaw while at the same time causing saturated downslope movement of the active layer (Harris 1981). Therefore, the common definition of solifluction is the slow (several mm to cm per annum) downslope movement of the active layer resulting from the annual freezing and

Figure 2.19 Solifluction (regions of green) at the mouth of Endalen. Note the tilting white poles in the centre left of the image. This is caused by soil moving downslope due to annual solifluction. In the center far-left is the solifluction monitoring station put in place by Harris et al. (2011). Photo © Huw Mithan.

thawing of soils (Ballantyne and Harris 1994; Matsuoka 2001a). Two processes contribute to this movement: (1) Frost creep which is the heaving of the active layer perpendicular to the slope during autumn freeze-back as a result of growing ice lenses, followed by near-vertical resettlement during the spring thaw; (2) Gelifluction which is the elasto-plastic deformation of thawed active layer material downslope during spring thaw (Harris 1981; Matsuoka 2001a; Harris and Smith 2003). Both processes can vary depending on the soil properties, stress history, ice lens concentration, and other environmental factors (Harris and Davies 2000; Harris et al. 2008a).

As a result, four types of mechanisms exist that can be considered solifluction. Firstly, needle-ice creep is a diurnal process that occurs when the upper centimetre of soil is lifted by ice needles and falls back onto the slope during thaw. This is a nocturnal process occurring on alpine terrain when the freezing plane advances less than a few centimetres into the soil (Matsuoka 2001a). Secondly, frost creep is both a diurnal and seasonal process by which the soil heaves normal to the slope due to expansion caused by the growth of segregated ice (Figure 2.20). Thirdly, gelifluction

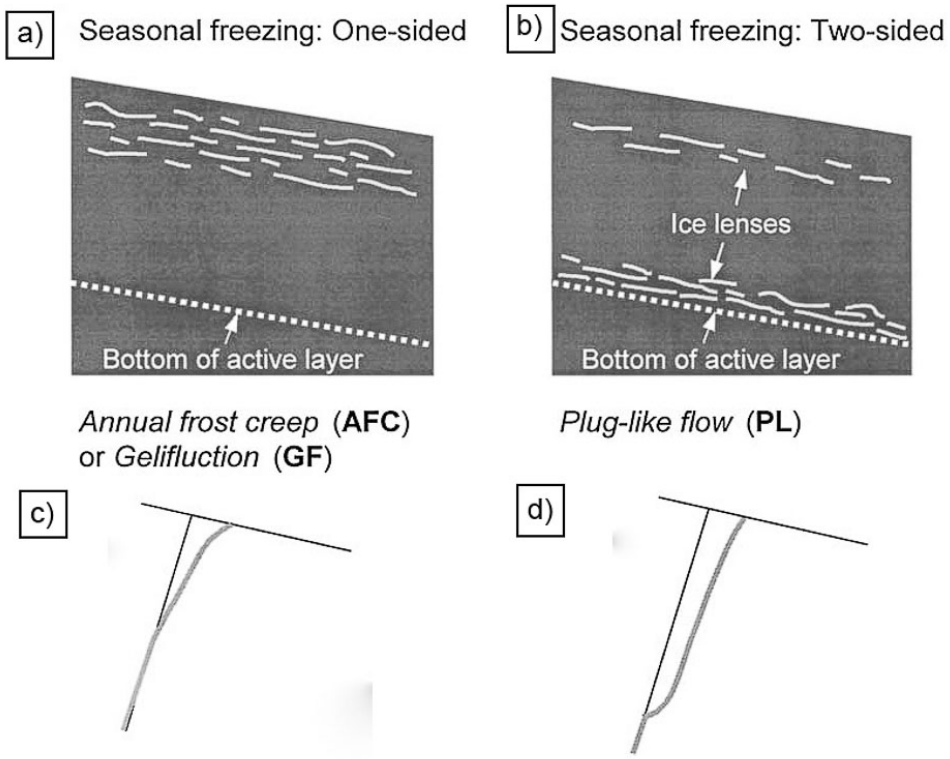

Figure 2.20 Diagrams showing a) the impact of one-sided freezing on the distribution of ice lenses in the active layer. b) two-sided freezing. c) Movement velocity profile caused by one sided freezing. d) Velocity profile caused by two-sided freezing. Adapted from Matsuoka (2001a).

occurs when the water content of the soil is greater than the plastic soil limit. Here the soil layer undergoes elasto-plastic deformation (Harris et al. 2003) (Figure 2.21). During thaw, the soil consolidates under its own weight because of the collapsing voids left by thawed ice lenses (Morgenstern and Price 1965). The expulsion of water from the voids and into the pore spaces of the soil matrix can create pore-water pressure in excess of hydrostatic (Harris et al. 2001b). Excess water can come from thaw consolidation of thawing ground or by inflow from melting snow, ice, or rainwater from the surface (Matsuoka 2001a). Thus the amount of gelifluction is strongly dependent on the amount of segregated ice in the soil (Harris et al. 2003). However, gelifluction movement is restricted to the upper soil layers where soil shear strengths are low (Harris et al. 2003). Finally, plug-like deformation is exclusive

to regions of continuous cold permafrost where two sided-freezing occurs (Mackay 1981). During summer thaw the ice-rich transitional layer undergoes thaw settlement creating a zone of plastic deformation of basal sediment, involving the full thickness of the active layer (Harris et al. 2008a). As a result, plug-like deformation tends to produce the greatest volumetric velocities. Matsuoka (2001a) found that because of plug-like deformation a soil mass with a depth of 110 cm produced volumetric displacements of 200 cm^3 cm^{-1} a^{-1}.

The strong relationship between frost heave and solifluction rates have led numerous studies to attempt to understand the topographic, climatic, and temporal controls on ground ice distribution (Harris et al. 2011). As ground ice is difficult to measure, these studies often look to understand the distribution of pore water within soil active layers (Harris et al. 2008b; Harris et al. 2011). One focus has been the distribution of snow cover, which provides a source of water to the active layer. Snow cover reduces soil freezing rate, thus promotes ice-lens growth (Matsuoka 2001a). The spatial and temporal variability in snow cover has been correlated with rates of downslope soil transport by gelifluction (Jaesche et al. 2003; Harris et al. 2008c; Harris et al. 2009). Other studies have emphasised the indirect effects of precipitation, length of snow cover, snow depth, and timing of autumn freezing as controlling frost heave rates (Ridefelt and Boelhouwers 2006; Ridefelt et al. 2011). Vegetation may also increase the rates of solifluction, where it traps snow to provide added water (Ridefelt et al. 2011). At a regional scale, lee-side accumulation of snow leads may increase pore water concentrations on west-facing slopes (Ridefelt and Boelhouwers 2006; Ridefelt et al. 2010).

Solifluction on slope gradients as low as 1° but as high as 36° (Washburn 1980; Matsuoka 2001a). This happens because of the dominance of gelifluction and plug-like deformation caused by two-sided freezing (Matsuoka 2001a; Harris et al. 2008c; Harris et al. 2011). Harris and Smith (2003) found that gelifluction was strongly influenced by slope gradient, creating flow-slide slope failure at gradients

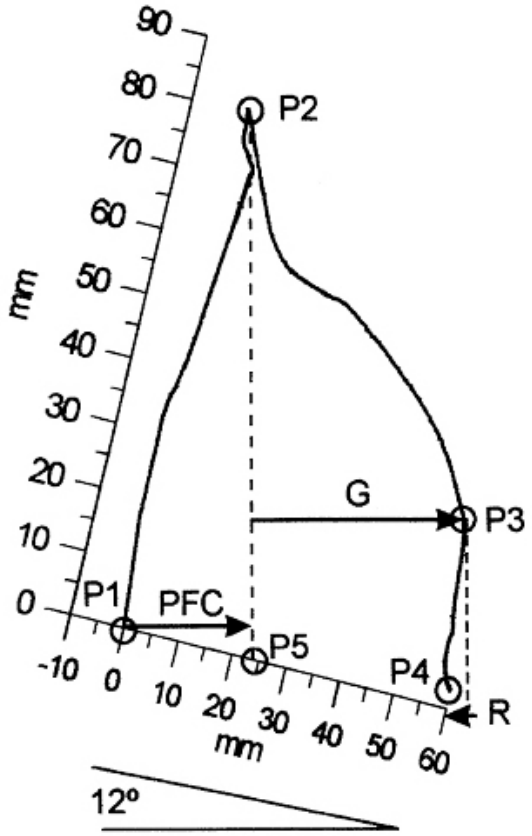

Figure 2.21 Movement of freezing and thawing soil. P1 - P2 Path of the target during frost heaving. P1 - P2 - P5 Path of target if only vertical settlement occurred during thaw. P2 - P3 Path of the target during gelifluction. P3 - P4 Path of the target with a settling of the ground. PFC is the horizontal component of potential frost creep, assuming vertical resettlement of the soil grains. G is the horizontal component of gelifluction. R is the horizontal component of retrograde movement. Adapted from Harris and Davies (2000).

above 16°. Contrary to this, a more recent study found that slope gradient only had a minor influence on solifluction (Harris et al. 2008a). Instead, the rate of soil movement appears to be sensitive to small changes in clay content and stress history (Harris et al. 2008a). Smith (2004) isolated slope gradient and found that the self-weight shearing stress increased with slope gradient. Matsuoka (2001a) found that solifluction velocity varies widely with gradient within a single study site, as did Harris and Smith (2003) during their laboratory simulations of gelifluction. A study of solifluction lobes in the Yukon found that lobes are larger at the foot of the hillslope and on shallower slope gradients (Hugenholtz and Lewkowicz 2002).

The material properties of the soil that control the formation of ice lenses also affect solifluction rates. Matsuoka (2011) proposed that the thickness of fine material increases downslope with decreasing slope gradients, favouring seasonal frost heave and thaw consolidation aided by increasing moisture content from convergent moisture sources. Soil macro fabric analysis has suggested that frost heave is dominant on shallow slopes because clast orientations are steeper than the slope gradient (Millar 2006). Clasts undergoing freeze-thaw action tend to rotate to a positon where their long axis is perpendicular to the direction of the freezing front (Washburn 1980).

The impact of vegetation at the regional scale is subsidiary to other factors such as topography and climate (Aalto and Luoto 2014). However, the effect of vegetation is more apparent at smaller scales, Eichel et al. (2016) demonstrated a strong relationship between vegetation cover and the occurrence of solifluction processes because the mat of vegetation trapped fine sediment and stored moisture in the soil, facilitating the development of ground ice in the active layer.

Long-term monitoring studies of solifluction rates on Svalbard and in Arctic Sweden have demonstrated that as the active layer deepens due to increasing summer temperatures, rates of solifluction have increased (Akerman 2005; Ridefelt et al. 2009; Harris et al. 2011). However, for the Swiss Alps, Matsuoka (2010) concluded that warming in discontinuous permafrost regions such as the Alps will reduce the seasonal depth of freezing thus limiting the rate of slope movement. Interestingly, a 35-year record of downslope soil movement in the Scottish Highlands demonstrated that solifluction processes can occur in non-permafrost regions with mild winter air temperatures and shallow ground freezing with volumetric velocities similar to those recorded in high-alpine environments (Ballantyne 2013).

2.3.6 Paraglacial environment

The term 'paraglacial' refers to landform processes and systems that are conditioned by former glaciation and deglaciation (Ballantyne 2002). Much of the alluvial fan deposits in glaciated regions are likely to have formed due to the reworking of glaciogenic sediment left by retreating valley glaciers at the end of the last glaciation, creating what's called paraglacial alluvial landsystems (Ballantyne 2002). The movement of glacial and hillslope-derived sediment by solifluction on, for example , Svalbard is part of a wider glacier foreland land system model (Ballantyne 2002).

2.4 Active Layer Detachments (ALDs)

2.4.1 Summary

Figure 2.22 A compact ALD at the base of a solifluction lobe in Adventdalen, Svalbard © Huw Mithan.

ALDs (Figure 2.22) are mass-wasting events characterised by shallow translational landslides that initiate in areas of continuous and discontinuous permafrost (Mackay 1981; Harris and Lewkowicz 2000; Leibman et al. 2003; Lipovsky et al. 2006; Gooseff et al. 2009; Lafreniere and Lamoureux 2013; Lamoureux et al. 2014; Niu et al. 2015). ALDs are thought to form by a reduction in shear strength at the

base of the active layer caused by a sudden increase in excess pore pressure from thawing of an ice-rich zone of segregated ice (Mackay 1981; Harris and Lewkowicz 1993). During a failure event, the active layer-mass slides along a slip plane. Physical modelling of ALDs have shown that the stress history, clay content, and the coherent nature of the soil are important geotechnical characteristics for the likelihood of ALD initiation (Harris et al. 2008c). Field measurements suggest that ALDs initiate in frost-susceptible silty clays but that high pore pressures are key for ALD initiation (Lewkowicz and Harris 2005b). However, high pore-water pressures alone cannot generate ALDs. If ground ice is sporadic or ice lenses are at shallow depth, the loss of shear strength during thaw may not be enough to exceed earth pressure or cohesion and create a through-going slip plane. Therefore, there may be more creep-like failure or solifluction. Hence, understanding which the ground ice conditions that promote the development of ALDs rather than solifluction remain an open question.

The distribution of ground ice varies through time as a function of soil moisture and temperature conditions. In regions of cold permafrost, ground ice distribution is governed by two-sided freezing (Mackay 1981). Here, a downward (from the surface) and upward (from the permafrost) freezing causes liquid water to migrate towards the surface and base of the active layer, leaving a desiccated central zone and an ice-rich zone at the base of the active layer. In a given year, the volume of segregated ice in a soil column is governed by pre-conditioning of the active layer via high summer rainfall prior to autumn freeze-back, which concentrates ice at the base of the active layer (Leibman 1995; Lewkowicz and Harris 2005a). During periods of average temperature conditions, a high moisture content in the active layer encourages strong ice lens development through time due to a thermally induced migration of unfrozen water to the basal zone (Lewkowicz 1990; Lewkowicz and Harris 2005b). Similarly, areas of high topographic convergence such as water-tracks, have greater summer water contents and greater winter ice development (Balser et al. 2009; Lamoureux and Lafreniere 2009). Extreme climate events that drive heat beyond the average

active layer depth and into the ice-rich basal zone can be caused by early thaw, thick winter snow depths, extremely high summer temperatures, and high rainfall (Dyke 2004; Lewkowicz and Harris 2005a; Balser et al. 2015). Non-climatic mechanisms for ALD initiation include forest fires, lateral river erosion, and civil engineering projects (Harris and Lewkowicz 2000; Jolivel and Allard 2013; Wang et al. 2014). Apart from the undercutting mechanisms, all ALD initiations depend on heat and the rate at which it moves through the active layer. In chapter 5, I explore this further by modelling the range of ground ice contents and thawing rates that promote ALD initiation.

2.4.2 Geographic extent

Much of our current understanding of ALDs comes from studies in the northern Canadian Arctic (McRoberts and Morgenstern 1974; Lewkowicz 1990; Lewkowicz 1992; Harris and Lewkowicz 1993; Kokelj and Lewkowicz 1999; Kokelj and Lewkowicz 1999; Couture 2000; Harris and Lewkowicz 2000; Lewkowicz and Kokelj 2002; Lewkowicz and Harris 2005a; Lewkowicz 2007; Favero 2009; Cannone et al. 2010; Lafreniere et al. 2013; Lamoureux et al. 2014; Rudy et al. 2017). Other sites include northern Alaska (Mackay 1981; Bowden et al. 2008; Balser et al. 2009; Gooseff et al. 2009; Swanson 2014; Balser et al. 2015). The Yamal Penninsual, Russia (Leibman 1995; Leibman et al. 2003; Ukraintseva and Leibman 2007). Svalbard (Larsson 1982) (Figure 2.23).

2.4.3 Morphology

Lewkowicz and Harris (2005a) categorised ALDs into three morphological types: (1) 'compact' where the detachment only moves a few metres to tens of metres, found at the footslopes bordering a floodplain or incised river bank; (2) 'elongate' types can initiate anywhere on a hillslope the mass of displaced material can be hundreds

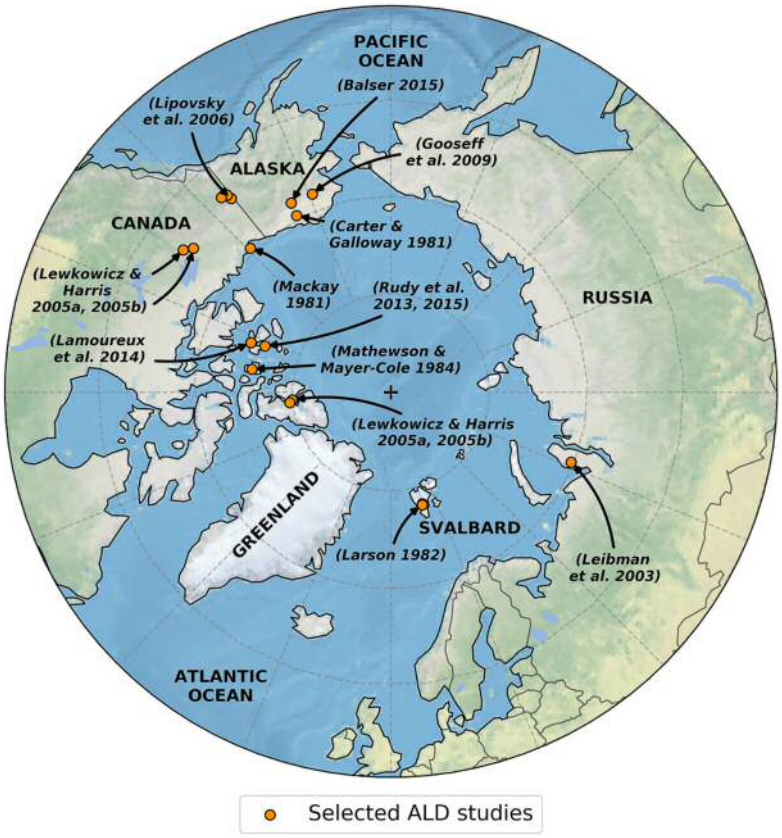

Figure 2.23 Map showing locations of selected ALD field studies in the northern hemishpere.

of metres away from the headscarp; and (3) 'complex' types which comprise of successive movements over multiple days, and the headscarp will continue to experience retrogressive failure (Figure 2.24). ALDs have run-out lengths of between 20 m to 1 km. They are typically 20 m to 30 m wide and up to 1.5 m deep (Harris and Lewkowicz 1993; Balser et al. 2015) (Figure 2.25). Failures exhibit an arcuate upslope scar, a runout zone with blocks of detached active layer on the surface, and a compressional zone of active layer material bounding the landslide at the toe and edges. Failures initiate from the toe upward, at the headwall, or along the runout zone (Harris and Lewkowicz 1993).

Whether a slide will move downslope as a cohesive block or as a viscous fluid depends on the geotechnical properties and cryo-history of the active layer (1993). An active layer with a low liquid limit (moisture content at which a soil begins to

behave as a liquid) and a high silt content will behave as a viscous fluid (Harris et al. 2008c). If the liquid limit and clay content are high, the soil will become more cohesive and shear planes will develop. This allows for blocks or entire regions of the active layer to slide downslope (Harris et al. 2008a; Harris and Lewkowicz 1993). During two-sided freezing of the active layer, water migrates from the centre to the top and bottom of the active layer, forming a central desiccated zone. As ice lenses thaw rapidly at the base of the active layer the water released is in excess of the liquid limit of the adjacent soil, forming a liquefied sediment layer of a few millimetres to centimetres thick. This causes a rigid block of active layer material to slide 'en masse' downslope across the underlying liquefied soil reaching speeds of 2 m h^{-1} to 9 m h^{-1} downslope (Lewkowicz 2007).

Swanson (2014) mapped 2246 ALDs in the Noatak National Preserve, Alaska. ALDs were most common on north-west facing slope aspects, on slope gradients ranging from 4.5° to 21.3°. ALDs can initiate on slope gradients as low as 1° to 2° (McRoberts and Morgenstern 1973; Leibman 1995). Lewkowicz and Harris (2005a) analysed the preferred aspect of ALDs relative to the valley orientation,

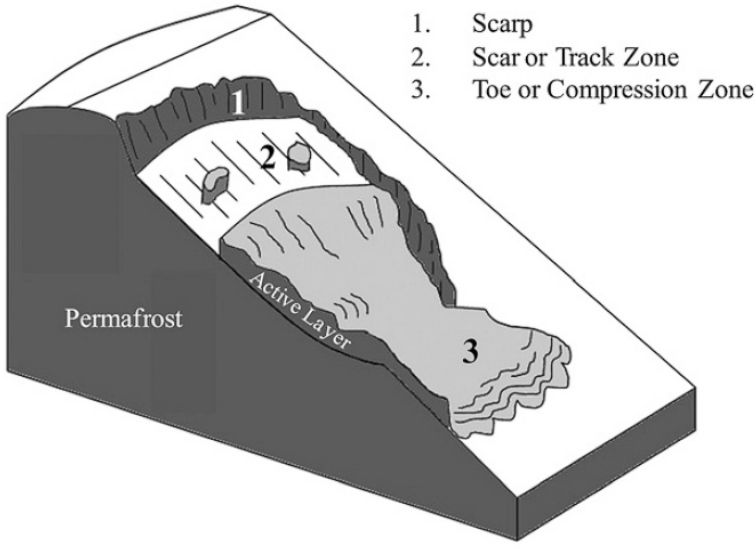

Figure 2.24 Conceptual diagram of an ALD and it's key characteristics. Adapted from Rudy et al. (2013).

providing some insight into the controls on ALD initiation. In the Mackenzie Valley, ALDs initiated on north-facing slopes (2005a). They found that north facing slopes were more likely to fail because: (1) lower amounts of solar radiation allow for permafrost to be more widespread and encourages greater amounts of ground ice, especially in the transition zone (Lewkowicz and Harris 2005a; Shur et al. 2005); (2) organic mats are thicker on north facing slopes allowing for a greater degree of thermal disturbance during forest or tundra fires; (3) variation in the thickness of frost susceptible glaciolacustrine silty clays within the valley meant that the likelihood of failure was greater in regions with greater thicknesses of frost susceptible soil (Lewkowicz and Harris 2005b). However, slope aspect might not be as important as other factors controlling the initiation of ALDs. At Big Top Creek on Ellesmere Island, ALDs initiated on east-facing slopes while at Hot Weather Creek on Ellesmere Island ALDs initiated on west-facing slopes (Lewkowicz and Harris 2005a). Both slope aspects recieve equal amounts of solar radiation (Lewkowicz and Harris 2005a). Lewkowicz and Harris (2005a) found that the slopes with the greater number of failures, regardless of aspect, had relatively greater ground-ice. Rudy et al. (2016) found that ALDs preferentially initiated on north-facing slopes and attributed this to preferential snow accumulation due to snow drifting, allowing for more moisture to accumulate in the soil during thaw.

2.4.4 Paleo ALDs

ALDs re-vegetate within five to fifteen years, becoming almost indistinguishable from adjacent topography (Swanson 2014; Balser et al. 2015). However, shear planes from paleo ALDs have been found within slopes consisting of clays in southern Britain (Hutchinson 1991; Ballantyne and Harris 1994), suggesting that these now stable slopes were once susceptible to active layer failure over ice-rich permafrost. In south-west France, remnants of a Pleistocene landslide have been

Figure 2.25 Satellite image taken in 2005 of an ALD (68.42 N, 158.54 W), 21 km to the north west of Feniak Lake, Alaska. Note the brown failure scar and the toe of damming the stream, forming a pool upstream and causing increased turbidity downstream. The image is orientated so that up is north. The length of the ALD is 200 m from head scarp to toe. Image from Google Earth.

observed within a 0.5 m layer of clay overlain by colluvium on a 3° slope (Bertran and Fabre 2005). The colluvium contained evidence of ice wedges, indicating past permafrost conditions (Bertran and Fabre 2005). Bertran and Fabre (2005) conducted slope stability analysis and determined that the slope could only have failed during undrained conditions similar to that of ALDs in the Canadian Arctic e.g. (Lewkowicz and Harris 2005b). The study by Bertran and Fabre (2005) show that ALDs occurred as far south as 45°N and that these mass-wasting processes may have been an indicator of a warming climate and an important geomorphological agent of denudation during the Pleistocene.

2.4.5 Triggers

Rapid late summer thaw

Swanson (2014) observed that ALDs mapped in Noatak National Preserve initiated during the unusually warm summer of 2004. Air temperature data showed that 2004 was the warmest summer on record (1950 to 2013). When Swanson (2014) compared the 2004 satellite imagery to 2007, he observed no more ALD activity. This could imply that ALDs require a pre-conditioning time period to allow segregated ground-ice to accumulate in the lower active layer/upper permafrost (Lewkowicz and Harris 2005a). Lewkowicz and Harris (2005a) demonstrated that late rapid summer thaw coincided with rapid thaw near the basal part of the active layer and ALD initiation. However, Lewkowicz and Harris (2005b) didn't attribute this as the sole cause. The thaw consolidation theory states that the rate of thaw should be the controlling factor for ALD initiation. However, Harris and Lewkowicz (2005b) observed high thaw rates at depth but no ALD initiation. This led to the conclusion that other factors contribute to the initiation of ALDs. These include: (1) pre-conditioning of the soil over consecutive years by plug-like solifluction which creates shear fabrics at the base of the active layer, reducing shear strengths close to residual values; (2) a development of an ice-rich layer at the base of the active layer from annual migration of moisture to the basal zone during autumn freeze-back (Harris and Lewkowicz 1993).

Forest/tundra fire

Lewkowicz and Harris (2005a) found that ALDs initiated weeks to months after the removal of forest and the insulating organic mat by fire. The removal of the organic mat allowed the thaw front to penetrate deeper into the active layer, reaching the ice-rich transition zone (Lewkowicz and Harris 2005b). In the Yukon, Lipovsky et al. (2006) found that the burning of the organic mat reduced surface albedo, and surface

shading from the tree canopy. Both act to increase the solar radiation absorbed into the ground surface. When comparing burnt and unburnt slopes, Lipovsky et al. (2006) demonstrated that burnt slopes were 3°C warmer. The absence of vegetation has another impact in that it reduces evapotranspiration and increases surface runoff, increasing the supply of moisture for the growth of ice lenses (Lipovsky et al. 2006). Swanson (2014) observed the presence of ALDs in satellite imagery after a forest fire in 2004 in the Yukon-Charley Rivers National Preserve.

Heavy rainfall

High rainfall can cause excess pore water pressures, an increase in soil moisture content, and thermal erosion. It can also act to precondition the active layer for failure the following summer. If rainfall occurs at the end of the summer and infiltrates to the base of the active layer then it won't completely drain away prior to autumn freezback. In this case, the concentration of ice lenses increases because there is a substantial source of moisture to feed their development. During the following summer, these ice lenses thaw releasing excess pore pressures greater than the capacity of the soil resulting in failure (Favero 2009).

Persistent and heavy rainfall in the Canadian high Arctic triggered mass-movements on slopes in the locality of Vendom Fiord in the eastern Queen Elizabeth Islands in July 1973 (Cogley and McCann 1976). On July 22, 49.4 mm of precipitation fell, with a total of 54.6 mm during the three-day storm. Mass-movements occurred on the margins of old alluvial terraces where the laminated silts were ideal for the production of thin lenses of ground ice. The exposure of massive ice and their subsequent melting led to a series of mass-movements, failing at the frost table (Cogley and McCann 1976). Other early studies noted the importance of summer precipitation for triggering mass-movements (Rudberg 1961; Pissart 1967). Larsson

(1982) observed multiple mass-movements on the slopes of the Longyear Valley, Svalbard after heavy precipitation in July 1972.

2.4.6 Importance of ALDs

Threat to infrastructure

An ALD in the village of Salluit, northern Quebec in September 1998 hit a new urban construction centre causing developers to abandon and remove twenty new houses (Allard et al. 2012). Longyearbyen (largest settlement on Svalbard) and is situated in the Longyeardalen glacial valley. In June 1982 a rainstorm event initiated 80 debris flows and multiple ALDs. No mass-movements reached Longyearbyen, but the close proximity of such mass-wasting events to a population centre demonstrated that extreme events such as rainfall could prove hazardous. In northern Canada, studies have highlighted the risk of ALDs to surface infrastructure for the transport of natural gas and oil, with some failures initiating beneath pipelines (Hanna et al. 1998; Lewkowicz and Harris 2005a).

Terrestrial carbon cycle

Permafrost contains twice the amount of carbon than that in the atmosphere (Zimov et al. 2006; Tarnocai et al. 2009). The top three metres is thought to contain 1,035+-150 Pg (1Pg = 1 billion tons) (Hugelius et al. 2014) (Figure 2.26). This carbon comes from the accumulation of plant and animal debris over millennia. In permafrost, carbon is stored as soil organic carbon (SOC) and is released during the summer by microbial decomposition as CO_2 and CH_4. Alarmingly, the Arctic is warming twice as fast as the global average (Stocker 2014). This is causing more frozen ground to thaw, and greater rates of organic matter decomposition and SOC release. The release of just a fraction of the stored CO_2 and CH_4 could increase the rate of future climate warming (Schuur et al. 2008; Schuur et al. 2015). Current research has

demonstrated the importance of thermokarst features such as ALDs as a mechanism by which permafrost carbon can become mobile (Jorgenson et al. 2006; Pautler et al. 2010). With a predicted increase in ALD frequency with a warming Arctic (Lewkowicz and Harris 2005a), ALDs are set to make a significant contribution to the release of carbon from permafrost. First, the movement of material from the top of the permafrost exposes that permafrost to warmer air temperatures. The thawing of the exposed permafrost encourages microbial activity. Second, the release of nutrients from permafrost into the Arctic stream network stimulates the growth of microbial activity (Pautler et al. 2010).

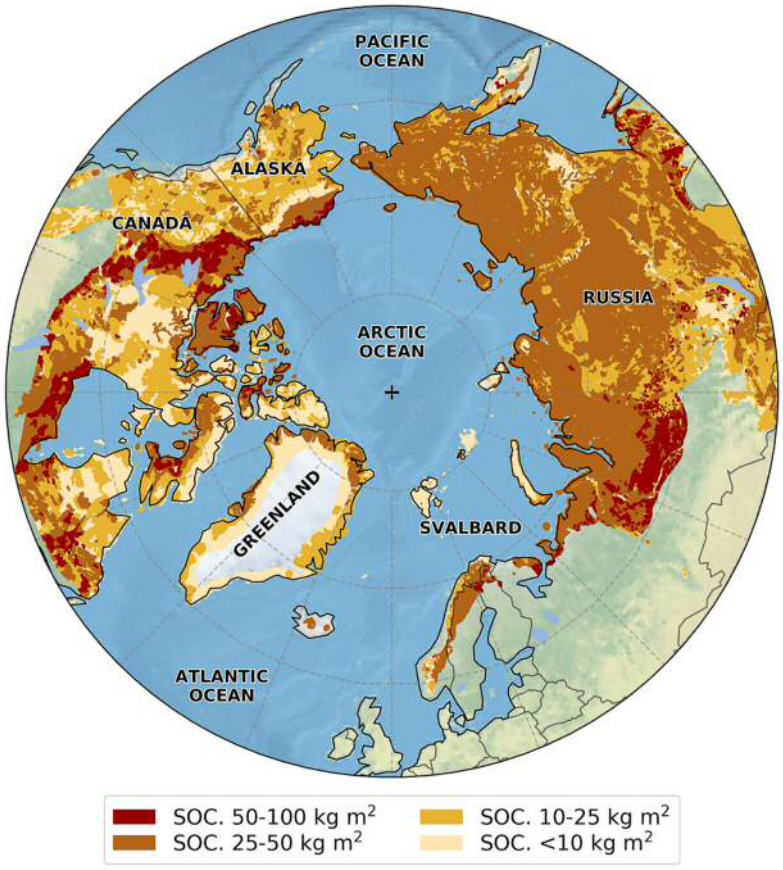

Figure 2.26 Map of soil organic carbon (SOC) in the top three metres of northern hemisphere permafrost. Data from Hugelius et al. (2013).

Sediment budget

ALDs are the dominant mass wasting-process on Arctic hillslopes in northern Canada (Lewkowicz and Harris 2005b). Transport rates are comparable to debris flows and slushflows in higher mountain environments (Lewkowicz and Harris 2005b). A study by Lamoureux and Lafreniere (2009) demonstrated that ALDs can have a significant impact on the sediment yield of two Arctic catchments in Cape Bounty, Canada. They found that ALDs act to dam river channels causing turbid pools of water to form upstream and along the slide track front. Measurements of water quality downstream showed that turbidity increased two to three days after the ALD event as each interconnected turbid pool broke through the soft sediment of the failed material and entered the stream network. Even though the area of mapped ALDs was small relative to the total catchment area, they had an observable impact on the sediment yield at the catchment scale Lamoureux and Lafreniere (2009). Furthermore, the slide tracks of ALDs expose permafrost to the ambient air. This encourages further thawing of the permafrost, generating secondary mudflows. The track depressions left by ALDs act as a trap for snow, enhancing the accumulation of snow. This results in greater meltwater and runoff, which increases soil erosion by surface wash (Kokelj and Lewkowicz 1999; Lewkowicz and Kokelj 2002).

2.5 Slope stability

Mass-wasting events occur because the forces trying to pull material downslope are greater than the forces resisting movement. Shear stresses are forces that act to pull material downslope, these are called the driving forces. Shear strength is a material's ability to resist the shearing forces, these are called resisting forces (Figure 2.27). The ratio between the driving and resisting forces is called the factor of safety ($FofS$) and can be expressed simply as

$$FofS = \frac{sum\ of\ resisting\ forces\ (\tau_r)}{sum\ of\ driving\ forces\ (\tau_d)} \tag{2.5}$$

If the $FofS$ is >1 then the slope is considered stable. When the $FofS$ is <=1 a slope is thought to be unstable. Many properties of soil on a slope can impact its likelihood of failure such as the stress history, soil type, soil thickness, geotechnical properties, water content, and slope gradient. In periglacial environments a further dimension of complexity is added because of thawing ice and the pore pressures generated.

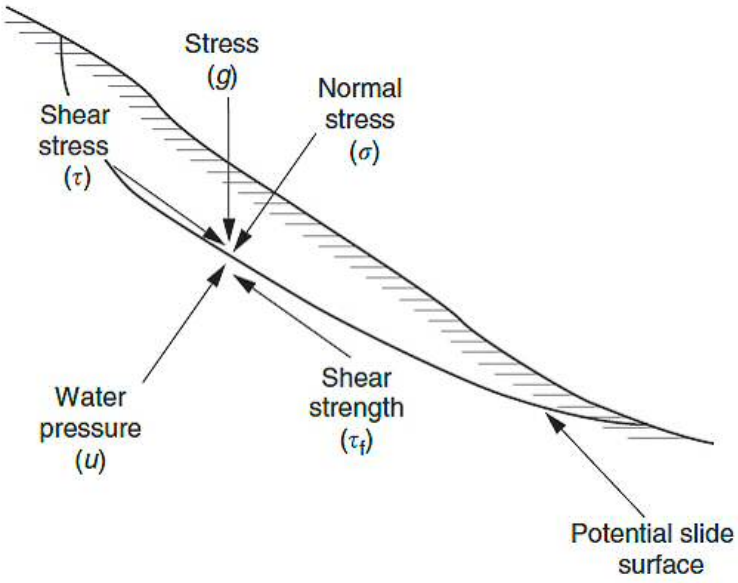

Figure 2.27 Resisting and driving forces acting on a slope. Adapted from Millar (2013).

Given the simple geometry of ALDs i.e. shallow and translational, it is possible to use an infinite slope model developed by Skempton and DeLory (1957) to assess the properties of thawing soils on slope stability. The shear stress of the soil acting parallel to the slope is given by

$$\tau_d = z\gamma \sin\beta \cos\beta \tag{2.6}$$

where z is the depth of the slip surface, γ is the unit weight of soil ($\gamma = \rho g$ where ρ is the soil density and g is the gravitational acceleration), and β is the slope gradient.

The pressure of the soil acting perpendicular to the slip surface is called the normal stress (σ)

$$\sigma = \gamma z \cos^2 \beta \tag{2.7}$$

To incorporate pore pressure generated by the weight of the soil:

$$\sigma' = \sigma - \mu \tag{2.8}$$

Where σ' is the effective normal stress and μ is the pore water pressure. The unit weight of water (γ_w) and the height of the water table above the slip surface (h) is included into the effective normal stress:

$$\sigma' = (\gamma z - \gamma_w h) \cos^2 \beta \tag{2.9}$$

The water table height can be expressed as a ratio of the height of the water table (m) above the slip surface (h) to the depth of the slip surface (z)

$$m = \frac{h}{z} \tag{2.10}$$

Therefore the effective normal stress can be re-written as

$$\sigma' = z(\gamma - m\gamma_w) \cos^2 \beta \tag{2.11}$$

The shear stresses are opposed by forces that try to stop movement, the shear strength of the soil τ_r (Figure 2.28). This is calculated based on the Mohr-Coulomb equation (Anderson and Richards 1987)

$$\tau_r = c' + \sigma' \tan \phi' \tag{2.12}$$

Where c' is the effective cohesion, σ' is the effective normal stress and $\tan\phi'$ is the angle of friction with respect to the effective normal stress. The $FofS$ equation in this study is expressed as

$$FofS = \frac{c' + z(\gamma - m\gamma_w)\cos^2\beta\tan\phi'}{z\gamma\sin\beta\cos\beta} \tag{2.13}$$

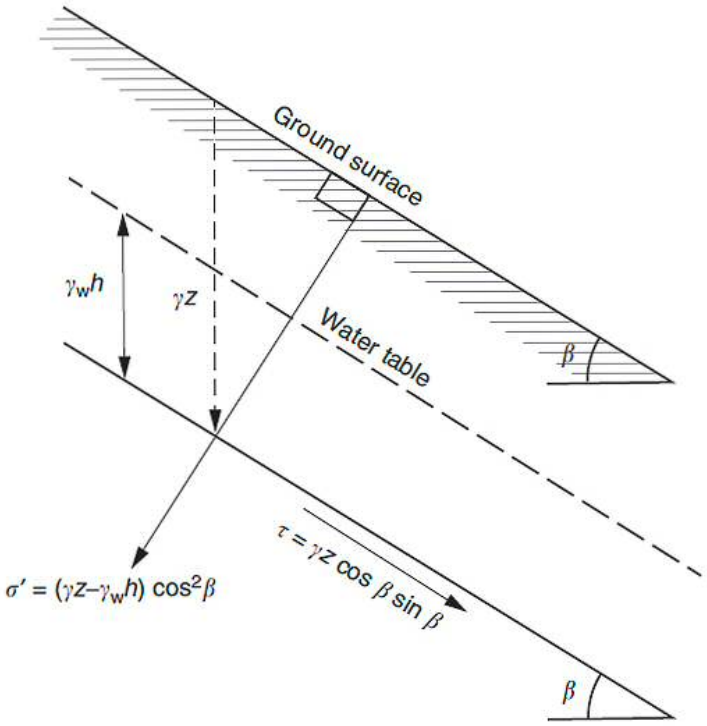

Figure 2.28 Shear stresses, including pore pressure, acting on a unit of soil on a slope. Adapted from (Millar 2013).

Cohesion (c') in the soils is created by the physio-chemical bonds between individual silicate minerals. Roots can offer some cohesion, but it has been observed that the failure plains of ALDs occur beneath the rooting depth of Arctic vegetation (Lewkowicz and Harris 2005b). Although, rooting systems can offer lateral cohesion. Sands and silts have no cohesion because the larger grain sizes have a smaller surface area thus there is less grain on grain contact. Friction is created by the interlocking of grains (Anderson and Richards 1987).

Chapter 3

Automated mapping of landforms in high Arctic mountains, Svalbard

3.1 Summary

A warming Arctic will lead to substantial changes in the rates and occurrences of the surface processes that generate and move sediment. The remote nature of mountainous Arctic landscapes leads to significant challenges in understanding the spatial distribution of these geomorphological processes. In this chapter, I develop a simple topographic classification of the geomorphological processes acting on Svalbard and use it to measure their spatial extent. I used Linear discriminant analysis (LDA) to determine the suite of topographic parameters that could most simply describe processes acting on the landscape. I validated and tested my results against detailed geomorphological mapping of two catchments in Svalbard (Endalen and Ringdalen). I found that slope gradient, relative position on the hillslope, and landscape roughness best described the spatial distribution of landforms in the area. Bedrock, solifluction, and blockfields were readily distinguished using this approach, with bedrock outcrops modelled at a higher resolution than was possible to map via remote sensing. Scree slopes were difficult to distinguish from the ubiquitous

vegetated allochthonous slopes, suggesting a similar origin for these deposits. The mapping demonstrates that in the region, solifluction and scree slope development are the dominant hillslope processes acting on this landscape and that sediment fluxes are greatest in solifluction.

3.2 Introduction

Arctic landscapes are particularly sensitive to changes in Earth's climate, as warmer temperatures, changing precipitation patterns, and more frequent extremes of precipitation and temperature (Jorgenson et al. 2006) can induce thawing of permafrost and increased rates of surface processes (Bonnaventure and Lamoureux 2013; Harris et al. 2009; Harris et al. 2001b; Lawrence and Slater 2005). For example, model predictions suggest that a 1°C increase in average monthly temperatures will reduce surface process rates by up to 33% in Finland (Aalto et al. 2014). Observations of recent significant hillslope erosion events have occurred because of extremes in weather, such as heatwaves or intense precipitation (Lamoureux et al. 2014). On Svalbard, solifluction rates increased in response to a particularly warm summer, where the active layer thickened such that ice lenses in the transient layer melted, and increased downslope sediment fluxes (Harris et al. 2011). Lamoureux and Lafreniere (2014) measured ALDs caused by exceptionally warm temperatures. Hence, the problem of sediment fluxes within Arctic landscapes relies upon both better understanding of erosion rates and the spatial distribution of the suite of processes that generate and transport sediment through these landscapes. Here, I seek to develop a method for automating the identification of different erosional processes in mountainous high Arctic landscapes, to identify the spatial distribution of each landform.

Identification of the spatial patterns of erosion across high Arctic landscapes has its genesis in the work of Anders Rapp (Rapp 1960b). The advent of readily available digital topographic models in GIS (Dikau et al. 1995; Evans 1972; Pike

1988) has allowed more detailed analysis of the shapes and spatial distribution of Arctic processes (Niessen et al. 1992) using a wide range of analytical methodologies such as statistical modelling approaches, including LDA (Giles and Franklin 1998; Hjort et al. 2014), logistic regression (Etzelmüller et al. 2001), and machine learning techniques, such as artificial neural networks (Aalto and Luoto 2014; Aalto et al. 2014; Hjort et al. 2014). These papers highlight the significant challenges associated with identifying and classifying landforms, particularly beyond the local scale. Therefore, wide ranges of topographic classifiers have been used to identify landforms, including elevation, slope gradient, slope curvature (and the many other elevation-based topographic derivatives), drainage area (and topographic wetness), slope aspect (and solar radiation) (Bartsch et al. 2002; Etzelmüller et al. 2001; Romstad 2001; Rudy et al. 2016) often used in combination with other remotely sensed information such as temperature measurements and vegetation characteristics (Aalto and Luoto 2014; Hjort et al. 2014).

Most classifications of the distribution of landforms tend to focus on one or a small number of processes and/or combining topographic data with climatic data and satellite-based imagery. I seek to develop a more generalised methodology, where I attempt to understand the spatial distribution of the major non-glacial geomorphological processes acting on a mountainous Arctic landscape and quantify the flux of sediment within the system.

Studies have shown how climate can have a profound impact on the erosion, storage, and deposition rates of periglacial landforms, impacting the sediment budget of landscapes (Matsuoka 2001a; Beylich 2008; Lewkowicz and Harris 2005a). To address this at a regional scale some studies have used a combination of remotely sensed data, field studies, and statistical analysis to model the distribution of landforms. There are few studies that have attempted to quantify the sediment flux of landforms on Svalbard (Hjort et al. 2014). This is important because Svalbard is an Arctic region already seeing rapid warming and geomorphological response to

current global warming (Akerman 2005). Having a tool with which to quantify current and future sediment fluxes will help our understanding of the future the topographic response to current global warming on Svalbard. In this chapter, I aim to combine field-based literature studies with my landform classification model to quantify the sediment flux in two glacial valleys on Svalbard, Endalen and Ringdalen. To do this I developed a landform classification model using topographic data only, to avoid issues with the interpolation of climate data and the interpretation of satellite imagery. I test the model against the geomorphological mapping of two catchments in Svalbard, Endalen and Ringdalen.

3.3 Study site

The 10 km^2 study sites are located in the Colesdalen and Adventdalen valleys, Svalbard (Figure 3.1). Svalbard is a high-Arctic semi-arid desert, with a mean annual temperature of -6.8°C (1961 to 1990, Svalbard Airport) and a mean annual precipitation of 190 mm. Permafrost is continuous outside of the glacier covered areas (Harris et al. 2009) and is typically 100 m thick in the valley bottom and 400 to 500 m thick at higher elevations (Humlum et al. 2003). The study area contains early Cretaceous to Eocene near-horizontally bedded sandstones, siltstones, shales and coal (Major et al. 2001). I developed the topographic model in Endalen, a north-east facing tributary valley to Adventdalen, 4 km south-east of Longyearbyen. I tested the model in Ringdalen, a west facing tributary valley to Colesdalen, 15 km south of Longyearbyen. These sites were chosen because a wide range of geomorphological studies provide information about the rates and mechanisms of the processes governing the development of Svalbard including studies of rockfall retreat (Akerman 1984; Andre 1997; Rapp 1960b; Siewert et al. 2012), debris flows and active layer detachments (Larsson 1982), solifluction (Akerman 2005; Harris

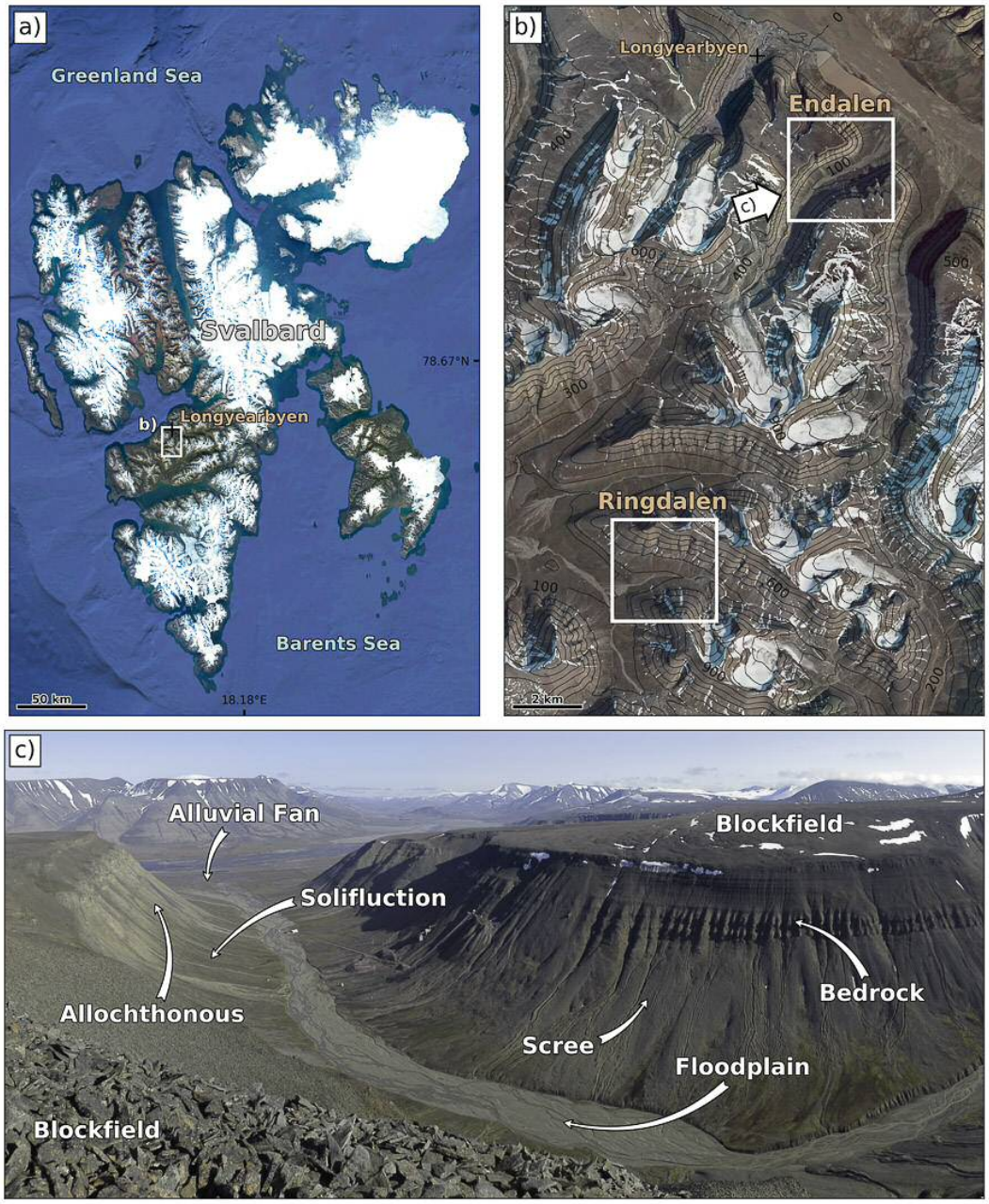

Figure 3.1 Study site location maps. a) Svalbard, satellite image from Google Earth. b) Endalen and Ringdalen, satellite image from Norsk Polar Institute. c) View of Endalen valley, image © Huw Mithan.

et al. 2011; Jahn 1967; Matsuoka and Hirakawa 2000) and alluvial and colluvial deposits (Haas et al. 2015).

Summit areas (600 to 700 m.a.s.l.) are typically flat plateaux composed of blockfields and patterned ground. Frost weathered sedimentary bedrock at plateau

edges (Eckerstorfer et al. 2013) lead downslope to steep planar (30° to 40°) deposits of scree and debris fans. Shallow (5° to 25°) concave slopes of solifluction sheets are found at the base of many hillslopes. Valley floors contain braided rivers that deposit sediment at valley mouths to form alluvial fans.

3.4 Materials and methods

I developed a method for automatically identifying landforms based on three readily available topographic parameters. This involved detailed geomorphological mapping of a catchment in Svalbard (Endalen and Adventdalen) to provide training and validation datasets. Deriving topographic metrics using LDA, I then validated the methods by applying them to an adjacent catchment in Svalbard (Ringdalen).

3.4.1 Geomorphology mapping

I created a 5 m resolution geomorphological map of Endalen to train the topographic model, then I mapped a smaller area of Ringdalen to use as a validation dataset. I first digitised a 1:100,000 scale geomorphological map of Svalbard (Tolgensbakk et al. 2000). However, I found the resolution of the mapping to be lower than was necessary for accurate identification of subtle landforms, such as bedrock outcrops. Instead, I mapped the same geomorphological units as Tolgensbakk et al. (2000) using higher resolution imagery (NPI 2014). In each photo, I focussed on the non-glacial landforms, defining each polygon using a reasonably coarse classification system of the following landforms; bedrock outcrops, floodplain, alluvial fan, block-field, scree/talus, solifluction, and allochthonous material. The coarse classification matches that used by Tolgensbakk et al. (2000) and are very similar to other classifications (Giles and Franklin 1998). I identified floodplains based on their multiple weaving channels caused by braided river incision. The floodplain boundary some-

times included a steep ridge or bank. Alluvial fans contained braided rivers but were arcuate with a distributary channel system located at the exit of a valley. The lateral margins are defined by a change in colour of the landform material and incised fluvial channels, respectively. Blockfields were flat areas found on the summit plateaus. Some individual angular blocks can be seen through the satellite imagery. Bedrock outcrops tend to be found at the margins of summit plateaus bounded by scree slopes. In imagery, bedrock is darker in colour and often contains significant shadow due to the steep nature of outcrops and low sun angle. Solifluction is found at the base of hillslopes, is vegetated and contains lobate deposits (Matsuoka 2001a). The areas of mapped 'solifluction' are zones of potential solifluction, and incorporate some lower slopes where debris cones fed by recurrent debris flows are the dominant landform. The area identified as 'solifluction' (or 'solifluction sheet') is, therefore, a maximum. Scree/talus slopes are non-vegetated deposits of blocky material located midway down a hillslope below exposures of bedrock. These deposits were either planar or slightly fan-shaped. Allochthonous material is defined simply as material that has moved downslope and is generally termed debris mantled slope. I identified this as the transition from active (grey in imagery) to a less active material (yellow-green in imagery) (Figure 3.2).

Tolgensbakk et al. (2000) used this term to indicate material that was found on side slopes that could not be obviously tied to a specific landform or process. I have continued to use this definition.

3.4.2 Topographic Analyses

I analysed the distribution of topography associated with the landforms described on the geomorphological map using initially a wide range of topographic descriptors, then used LDA to identify the most important topographic metrics for discriminating landforms. The analysis was carried out on a 5 m photogrammetry-derived DEM

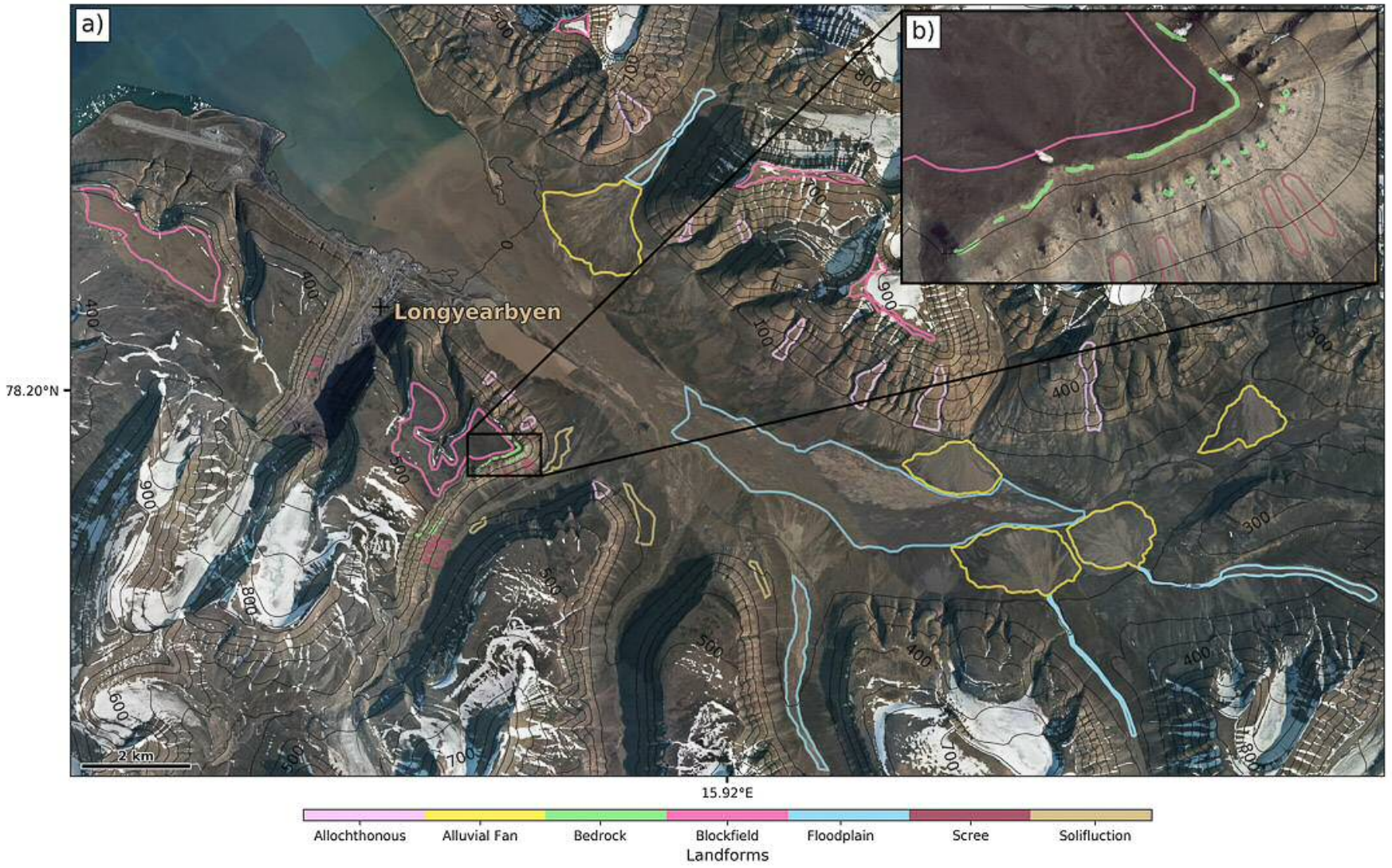

Figure 3.2 a) Landforms used to train the classification model. Satellite image from the Norsk Polar Institute. b) Inset map showing mapped bedrock in more detail.

(NPI 2014). From the DEM I removed anthropogenic infrastructure, water bodies, artefacts, pixels that were within the shadow shown in the satellite image, pixels that correspond to snow cover in the satellite image, glaciers and their features, and filled sinks in the raster surface.

I defined a range of topographic metrics that are commonly used in topographic analysis including ArcGIS-derived slope aspect, slope gradient, planform curvature, profile curvature, total curvature, topographic wetness index, as well as topographic openness (Yokoyama et al. 2002), a measure of roughness based on the directions of poles to planes on the surface (McKean and Roering 2004), and a relative local relief metric. Relative local relief (RLR) is the relative elevation of a pixel to the maximum and minimum elevation values within a 5 km diameter circular neighbourhood. RLR values vary from 0 (lowest elevation) to 1 (highest elevation) as

$$RLR = \frac{x - x_{min}}{x_{max} - x_{min}} \tag{3.1}$$

where x is the elevation of a pixel, x_{min} and x_{max} are the minimum and maximum elevations within a 5 km circular window. I used the topographic roughness method of McKean and Roering (2004), which has been demonstrated as an effective method for identifying landslide material (McKean and Roering 2004) and bedrock (Milodowski et al. 2015). The method uses the statistical variability in the poles to each DEM pixel within a square window of fixed size (in this case 3 x 3 pixels). I used the SR1 eigenvalue ratio (McKean and Roering 2004).

3.4.3 Automated analysis of landforms

I used the LDA method to automatically identify landforms. LDA is commonly used as a supervised machine learning tool and as a statistical method for dimensionality reduction (Giles and Franklin 1998). LDA finds the best linear combination of topographic parameters that (1) maximise the distance between the means of two or

more classes, while (2) minimising the scatter around the mean, within each class. LDA projects this information onto a new axis called LD1, LD2, etc. with LD1 representing the best linear combination of variables that fulfil (1) and (2).

LDA is useful because it has been widely and successfully applied to classify landforms, including a number of Arctic applications (Brenning 2009; Giles and Franklin 1998), and it is possible to compare the linear relationship with my expectations based on my physical understanding of the processes governing each landform. There are some weaknesses in the method. Firstly, it does not account well for processes with a non-linear relationship between variables, and secondly, there is an assumption that covariables follow multivariate normal distributions (Brenning 2009)

Using landform polygons from Endalen and Adventdalen I trained the classifier. For each landform polygon, I extracted its pixel values from the topographic parameter rasters. In order to assess the classifier's performance, I split the landform dataset into a 70% training set and a 30% testing set and evaluated the classification using an 'accuracy' metric (the ratio of the number of correctly predicted landforms divided by the total number of landforms multiplied by 100). I repeated this train/test split procedure ten times on different segments of the landform dataset and took the average accuracy score, a process called k-fold cross-validation. I used this test to ensure that the classifier didn't perform differently after being trained on different segments of the landform dataset. I used the training set in the LDA classifier module in Python's Scikit-Learn machine learning programme (Pedregosa et al. 2011) to train the LDA classifier.

I performed a recursive feature elimination analysis to automatically determine which three topographic parameters contribute the most to the predictive power of the LDA classifier. By recursively removing topographic parameters, recursive feature elimination analysis uses the model accuracy metric to identify the best combination of topographic parameters. This method helps to reduce over-fitting,

improve accuracy, and reduces training and testing time. I found that relative local relief, topographic roughness, and slope gradient to be the best performing topographic parameters.

I performed two further tests to assess the accuracy of the model. First, I tested the model in Ringdalen. I input the three 10 km^2 topographic parameter rasters (relative local relief, topographic roughness, and slope gradient) into the trained classifier. The classifier iterates through each x-y coordinate, taking the corresponding relative local relief, slope gradient, and topographic roughness pixel values and calculating their position on the linear discriminant (LD) axes. Where they are plotted on the LD axes determines which landform type is assigned to the group of three pixels. Once all iterations are complete, the product is a 10 km^2 raster where each pixel has a landform classification.

3.4.4 Accuracy, recall, and precision

To assess the quality of the classifier I used three metrics; accuracy, recall, and precision. Accuracy is the proportion of correct classifications (true positives and negatives from the overall number of cases.

$$Accuracy = \frac{T_p + T_n}{T_p + T_n + F_p + F_n} \tag{3.2}$$

Recall is the proportion of correct positive classifications (true positives) from the cases that are actually positive

$$Recall = \frac{T_p}{T_p + F_n} \tag{3.3}$$

Precision is the proportion of correct positive classifications (true positives) from cases that are predicted as positive

$$Precision = \frac{T_p}{T_p + F_p} \tag{3.4}$$

where T_p are the true positives, T_n are the true negatives, F_p are the false positives, and F_n are the false negatives. Therefore, the accuracy scores tells us how well the model performs overall. Precision answers the question, of all the landforms labelled as landform 'x', how many were actually landform 'x'? Recall answers the question of all landforms that are truly x, how many did the model label as x? (Figure 3.3).

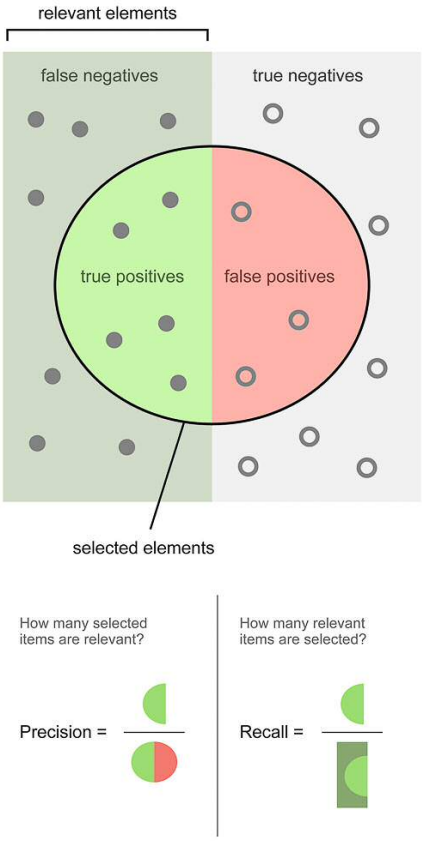

Figure 3.3 Conceptual diagram of precision and recall. Adapted from Walber (2017)

.

3.5 Results

3.5.1 Landform topography

Because of their similar genesis, floodplains and alluvial fans have similar topographies occurring on valley floors (average relative local relief of 0.04 for floodplain, 0.05 for alluvial fans), with rough channelized surfaces (average topographic roughness values of 0.02 for floodplain and 0.69 for alluvial fans), and shallow slopes (average values of 1°) (Figure 3.4 and Table 4.1). The significant number of summit plateaus meant that these landforms were easily distinguishable as features of low slope gradient (average value of 3.8°) located in the higher parts of the landscape (average relative local relief of 0.80), with an average roughness of 0.59. Bedrock is also found at higher elevations (average relative local relief of 0.59) on very steep slopes (average value of 56.8°) with average roughness values of 1.42. Solifluction lobes are found on lower parts of hillslopes (average relative local relief of 0.12) with low slopes (average value of 6.43°) and a roughness of 1.58. Scree/talus slopes and allochthonous slopes had very similar topography typically found mid-slope (average relative local relief of 0.23 for scree and 0.31 for allochthonous slopes) with similar slopes (average slope gradient) of 27.3° for scree and 25.7° for allochthonous) and smooth slopes (average topographic roughness values of 2.33 for scree and 2.24 for allochthonous slopes) (Figure 3.4 and Table 4.1).

3.5.2 Model training results

The LDA results show that more than 95% of the proportion of separation between landforms is caused by a combination of the LD1 (65.78%) and LD2 (33.63%) axes (Figure 3.5a). Relative local relief controls 98.87% proportion of separation between landforms along the LD1 axis. Along the LD2 axis slope gradient (10.14%) and topographic roughness (8.27%) have a greater influence but relative local relief remains

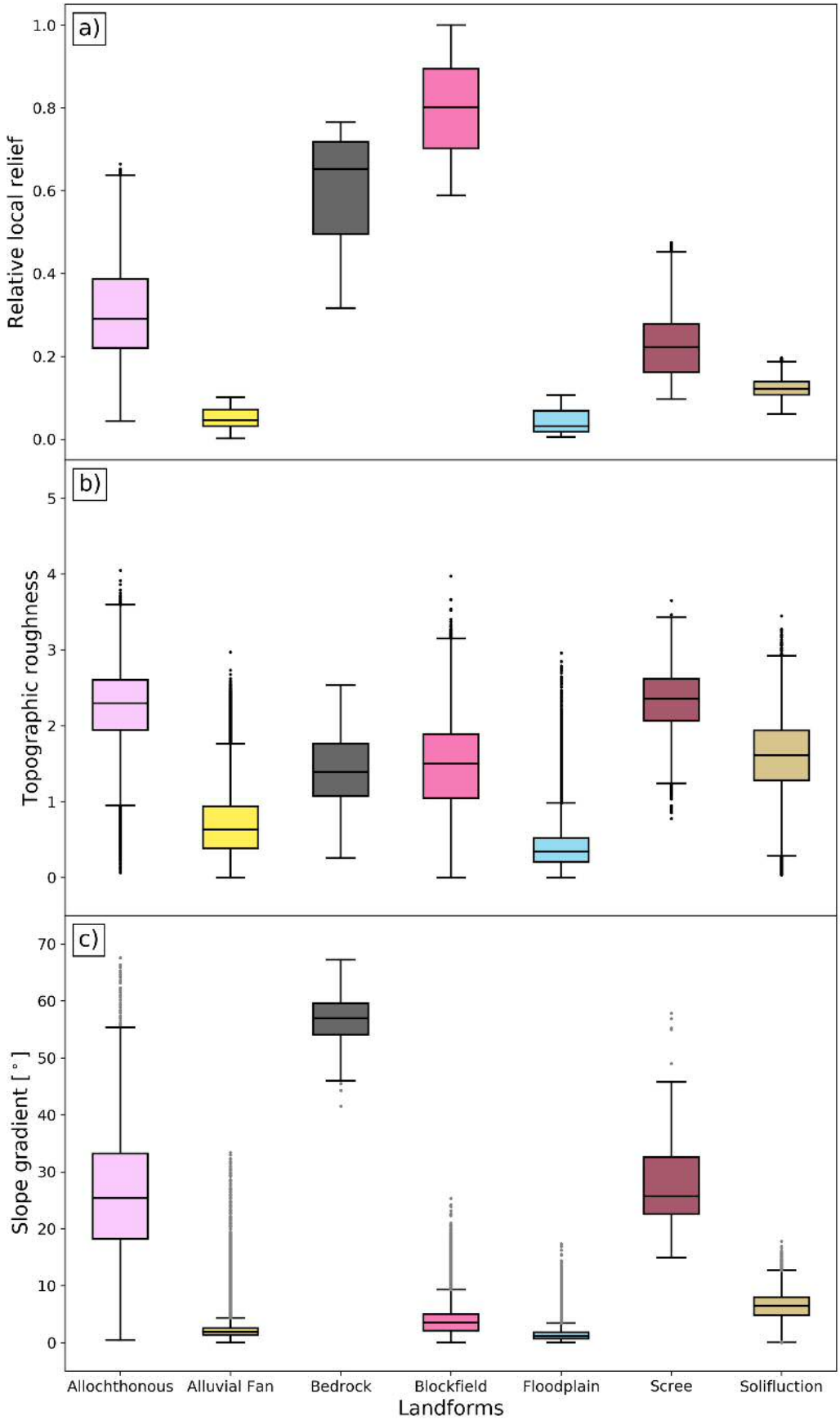

Figure 3.4 Box plots of landforms and their topographic parameters. a) Relative local relief. b) Topographic roughness. c) Slope gradient.

Table 3.1 Landform training data statistics. Relative local relief (RLR), topographic roughness (TRgh), Slope gradient (SGr).

			RLR		TRgh		SGr (°)	
Landforms	Polygons	[km^2]	mean	SD	mean	SD	mean	SD
Allochthonous	11	1.59	0.31	0.12	2.24	0.51	25.68	9.12
Alluvial fan	5	8.44	0.05	0.02	0.69	0.39	2.12	1.28
Bedrock	23	0.01	0.59	0.15	1.42	0.46	56.83	4.30
Blockfield	5	4.46	0.8	0.10	1.45	0.59	3.78	2.30
Floodplain	8	10.58	0.04	0.03	0.02	0.27	1.34	0.90
Scree	15	0.16	0.23	0.08	2.33	0.41	27.27	5.72
Solifluction	4	0.53	0.12	0.03	1.58	0.51	6.43	2.40

dominant (81.59%) (Figure 3.5b). These results demonstrate that a considerable amount of the predictive power of the model lies with a small number of variables, relative local relief, slope gradient, and topographic roughness. Relative local relief and slope gradient are the strongest landform separators when used together (Figure 3.6). How the LDA model defines linear boundaries between landforms after being trained is seen in (Figure 3.7).

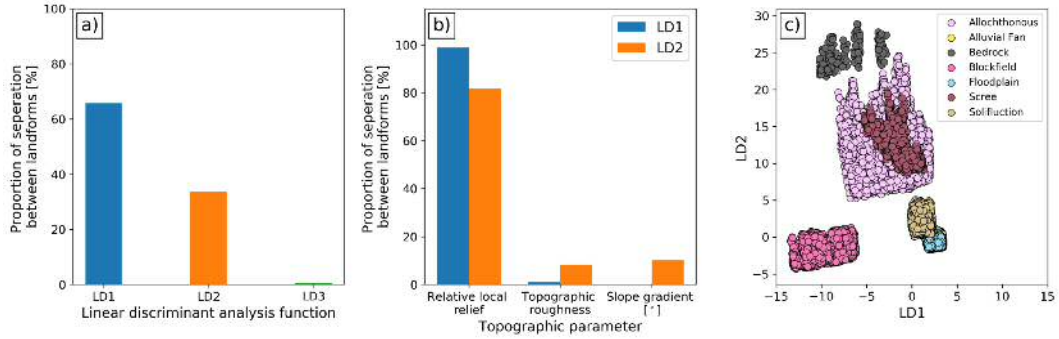

Figure 3.5 LDA results. a) Influence of each linear discriminant axis on landform separation. b) Impact of each topographic parameter on LD1 and LD2. c) How LD1 and LD2 separate landforms.

3.5.3 Model implementation and internal testing - Endalen

Initial internal testing of the model with a 70% training and 30% test datasets produced a mean accuracy score of 77.3 (± 0.2)%. More detailed analysis of

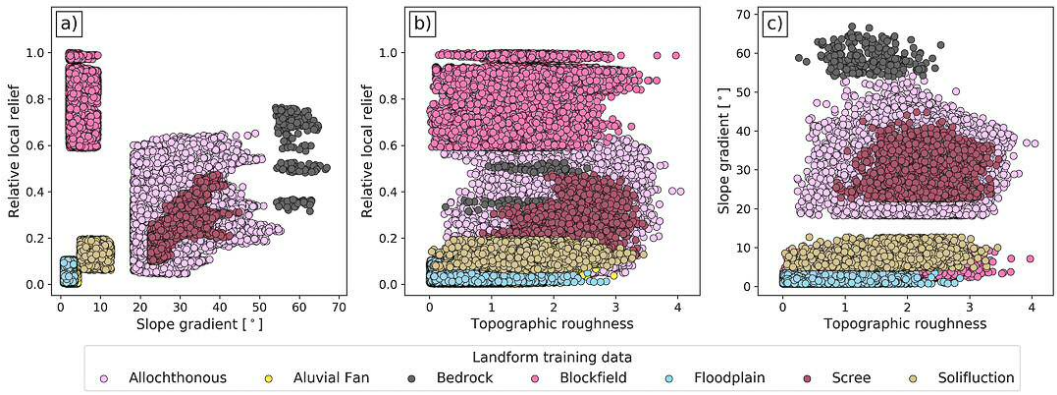

Figure 3.6 Plots showing how the training dataset relates to the three topographic parameters. a) Slope gradient against relative local relief. b) Topographic roughness against relative local relief. c) Topographic roughness against slope gradient.

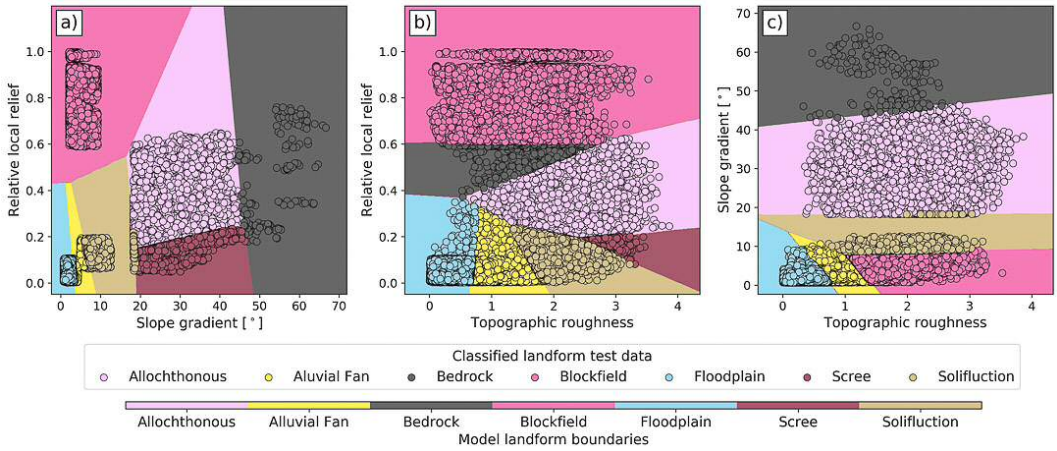

Figure 3.7 Bivariate plots showing how the model classified the test dataset. Polygons represent model landform boundaries. a) Slope gradient against relative local relief. b) Topographic roughness against relative local relief. c) Topographic roughness against slope gradient.

the recall (the ratio of true positives against true positives + false negatives) and precision (defined as the ratio of true positives against true positives + false positives and is a measurement of uncertainty) of the analysis demonstrates that reductions in accuracy are related to the misclassification of geomorphological units with similar topographies. The model performs best when predicting blockfields, solifluction, allochthonous areas. Blockfields have 100% recall and precision, suggesting a very accurate classification of these features. Solifluction sheets were also accurately identified (recall of 81%, precision of 95%), with the most common misidentification

being alluvial fans (recall of 18%). Allochthonous areas have a recall of 85% and a precision of 91% and were most commonly misidentified as scree. Bedrock has a high recall (100%) but low precision (54%) suggesting that the model classified most of the bedrock pixels within the test dataset, but 46% of the pixels it identified as bedrock pixels were mapped as allochthonous areas. Alluvial fans have a low recall (53%) and a high precision (74%) suggesting that the classification misidentifies alluvial fan pixels as either floodplain or solifluction. Scree has a very low recall (14%) and a low precision (9%) because the model usually misidentifies scree slopes as allochthonous surfaces.

The similarity in the topographies of alluvial fans, which are composed of sediment deposited predominantly by braided rivers, and floodplains themselves is not particularly surprising for a pixel-based classification. Similarly, a confused classification of areas of active scree slope and allochthonous material, which is typically found on similar slopes to scree and is mostly differentiated by vegetative cover. To test the effect of differentiating these similar landforms on classification accuracy, I ran the LDA classification for a dataset where floodplains and alluvial fans were combined into a "valley bottom" unit and allochthonous areas and scree slopes were combined into a "loose hillslope material" unit, the accuracy of this model increased to 99.1%. The low precision for bedrock areas may in some part be because the classification is better able to recognise bedrock that the geomorphological mapping missed. Bedrock outcrops are small, often a few pixels wide and are sometimes difficult to recognise on the aerial imagery I used to map them.

3.5.4 Model validation - Endalen test

A classified map for a 10 km^2 sample area portion of Endalen produced using the trained LDA model has an overall accuracy of 81.69%. The map demonstrates

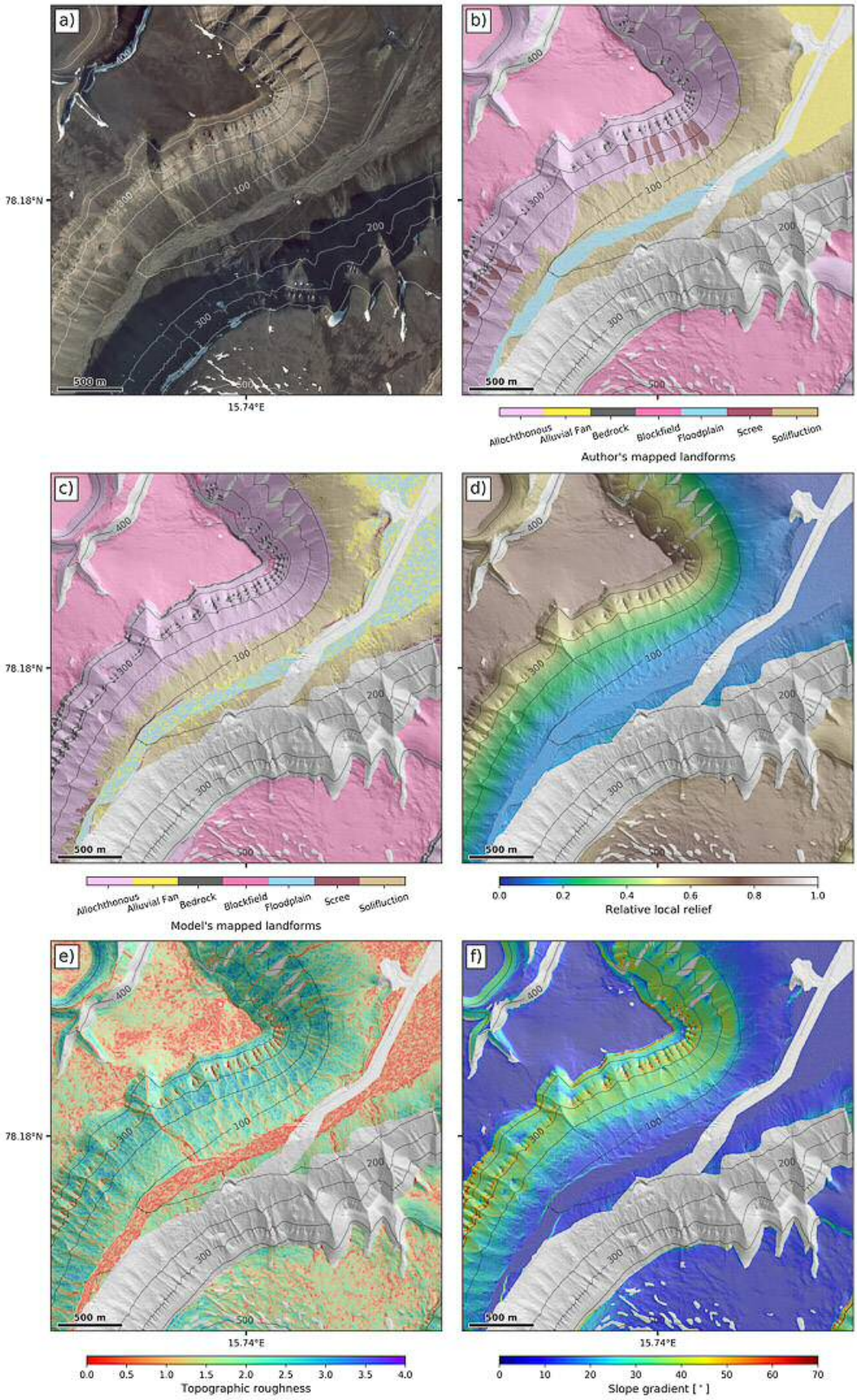

Figure 3.8 Maps of Endalen. a) Satellite image from the Norsk Polar Institute. b) Author's landform map. c) Model's landform map. d) Relative local relief. e) Topographic roughness. f) Slope gradient. Contours are in metres. Maps are underlain with a hillshade. Grey regions have no data.

the success of the classification scheme in identifying the spatial distribution of landforms within these areas (Figure 3.8).

Occupying the flat plateaus of Endalen are blockfields, and is the most extensive landform covering 3 km^2 (Figure 3.9). Bedrock is modelled at the plateau edge, contouring the top of the hillslopes but also 100 m downslope from the plateau edge. Bedrock covers the smallest area of c.a. 0.2 km^2. The mid-slopes are dominated by allochthonous material and are the second largest landform c.a. 2.1 km^2. Its upslope boundary is defined by the plateau edge, bounding solifluction at its downslope margin. Solifluction occupies an area of 1.1 km^2 the third most extensive landform. The downslope boundary of solifluction borders the braided river and alluvial fan. Solifluction is most extensive at the mouth of the valley. At the mouth of Endalen scree is classified on the slopes between solifluction and the alluvial fan. These classifications coincide with an area of steep slopes on the valley floor. As a result, scree only occupies 0.3 km^2 of the study area. Areas of solifluction adjacent to the centre of the valley contain pixels classified as alluvial fan. The extent of this increases toward the north-east. In the centre, running from the south-west to north-east is a mixture of pixels classified primarily as a floodplain but some are incoherent clusters of alluvial fan material (Figure 3.10).

3.5.5 Model validation - Ringdalen test

A classified map for a 10 km^2 of Ringdalen had an overall accuracy of 76.63% (Figure 3.10). This is lower than Endalen but still a successful application of the model (Figure 3.9). Blockfields and flat plateaus are less of a prominent feature, occupying an area of c.a. 0.4 km^2 (Figure 3.9). The occurrence of bedrock is restricted to the top of cirques in the north-east and small ridges 500 m to the west. Allochthonous material is the dominant landform occupying c.a. 5.3 km^2, and is extensive on north and south facing slope, extending 700 m downslope. Unlike in Endalen, the

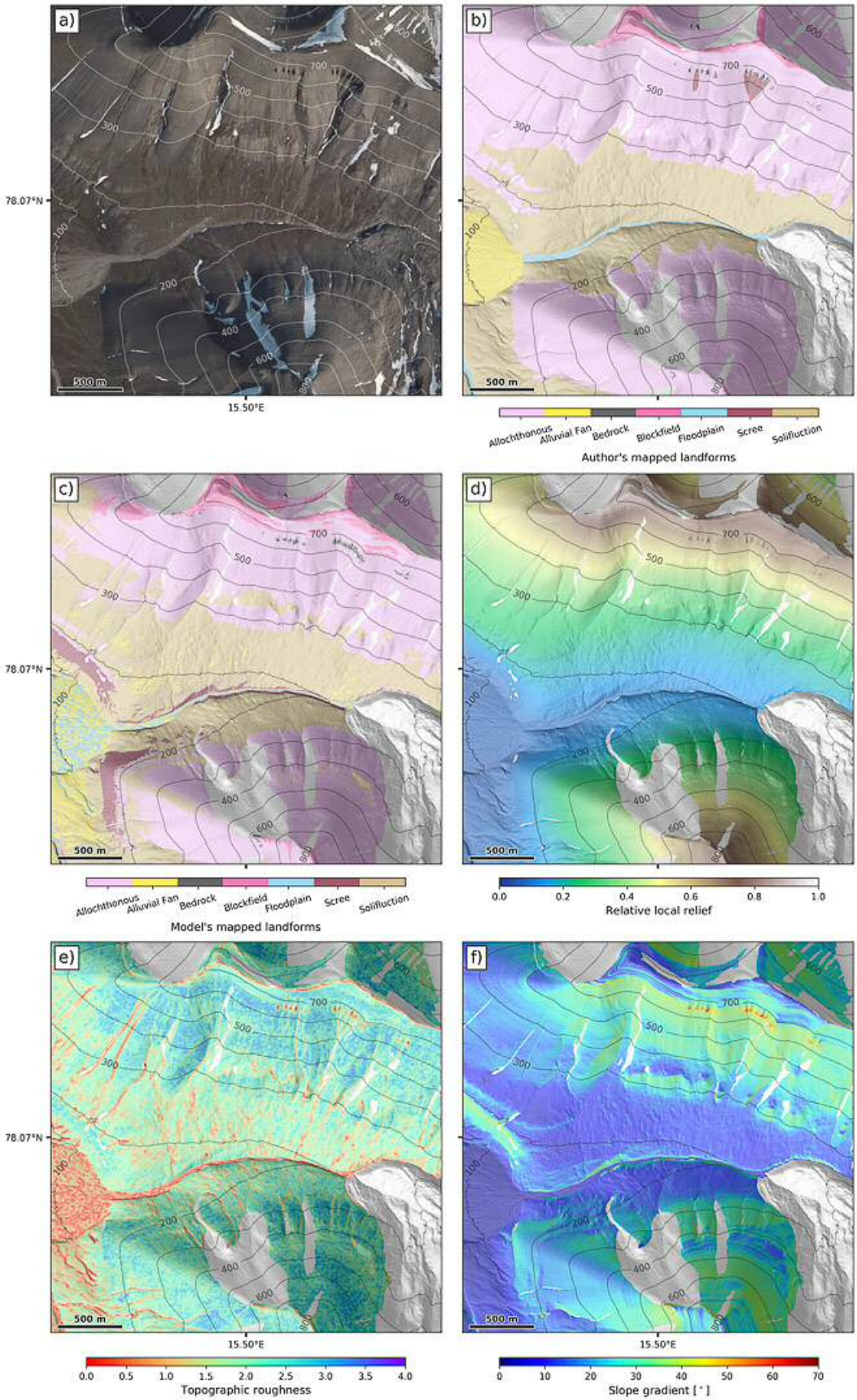

Figure 3.9 Maps of Ringdalen. a) Satellite image from the Norsk Polar Institute. b) Author's landform map. c) Model's landform map. d) Relative local relief. e) Topographic roughness. f) Slope gradient. Contours are in metres. Maps are underlain with a hillshade. Grey regions have no data.

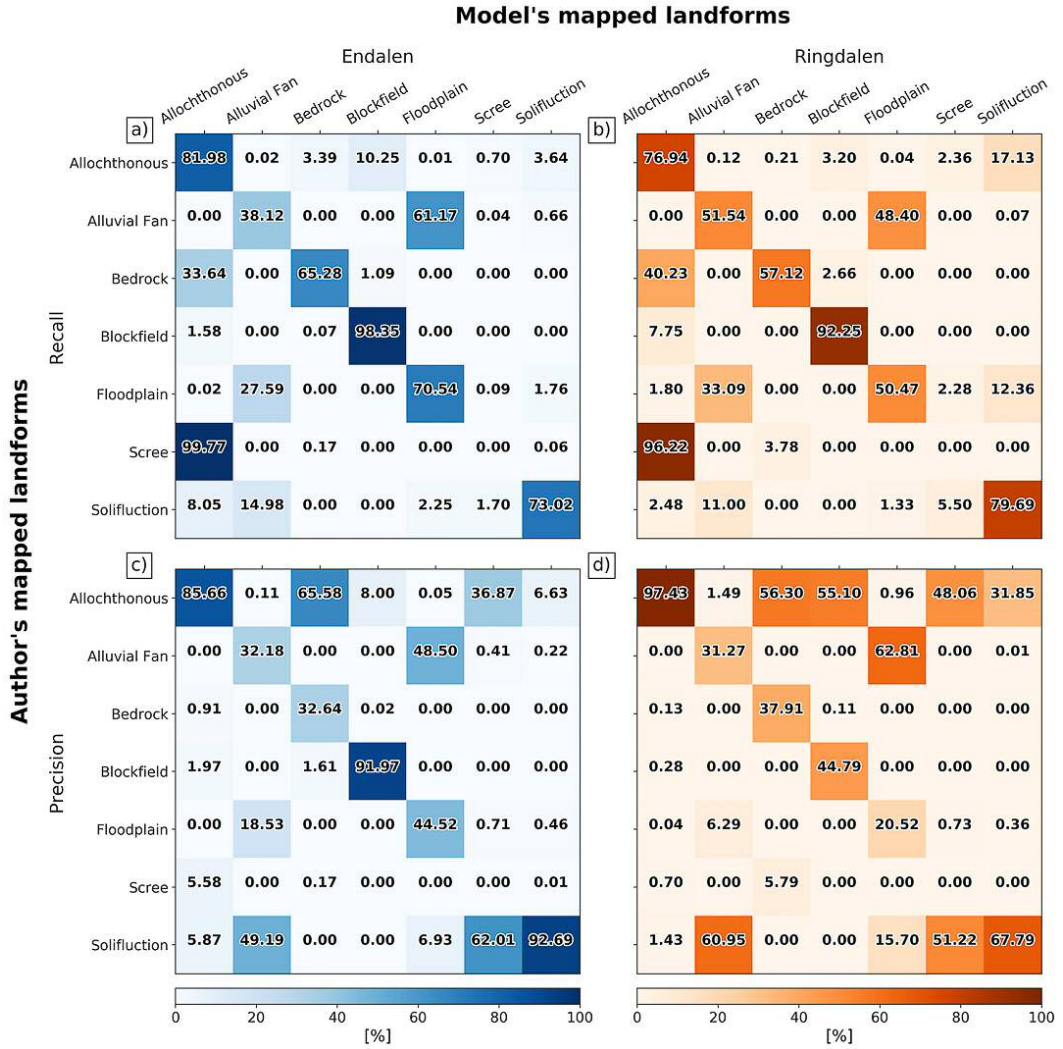

Figure 3.10 Confusion matrices comparing how the model performs against the author's landform map. a) Recall matrix for Endalen. b) Recall matrix for Ringdalen. c) Precision matrix for Endalen. d) Precision matrix for Ringdalen.

allochthonous material in Ringdalen doesn't reach the valley floor. Its downslope boundary is with solifluction, the second most dominant landform occupying nearly 3 km^2 of the study area. The model predicts solifluction to occupy the lower half of the hillslopes in the centre of Ringdalen and less in the south. Clusters of alluvial fan material are found on the mid to lower reaches of the solifluction material. These clusters become denser at the mouth of Ringdalen. Patches of solifluction occupy relatively flat sections of hillslope in the centre north. Scree slopes are absent on the upper slopes below bedrock outcrops. Instead, scree is found at the downslope

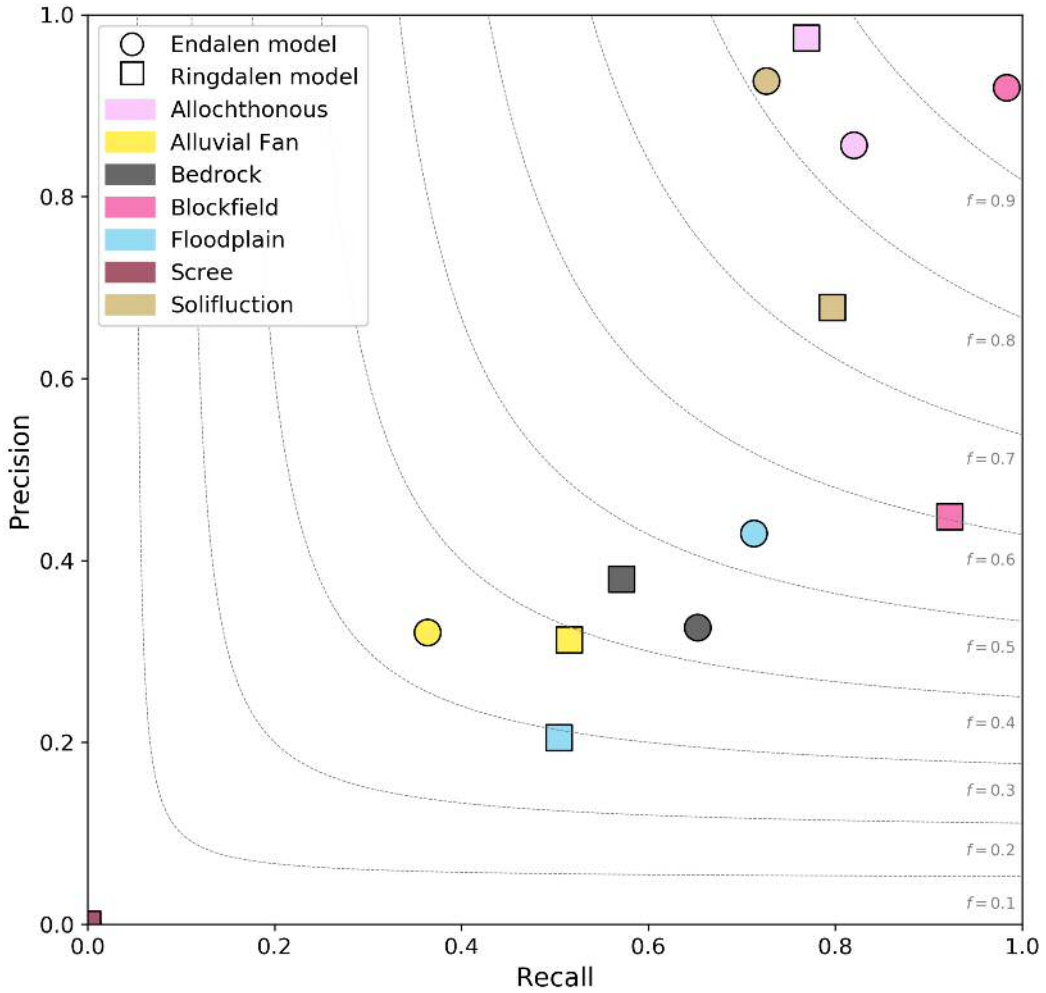

Figure 3.11 Plotting recall against precision for each landform in the Endalen and Ringdalen models. The grey dashed lines are f-measure contours, which is the weighted average of precision and recall: F-measure = 2 * (precision * recall) / (precision + recall).

boundary between solifluction and the braided river in the centre and east side of Ringdalen. Scree slopes either occupy the banks of the floodplain or the bounding slopes of the alluvial fan. Pixels classified as braided river are found in the central channel of Ringdalen and in the south-west corner. However, these channels are bounded by scree but also occupying where the alluvial fan should be. There appears to be less alluvial fan material where the alluvial fan should be and instead is found on adjacent solifluction slopes. Allochthonous material, solifluction and blockfield cluster in the top right corner of a precision-recall plot, demonstrating that the model is good at classifying these landforms (Figure 3.11).

3.6 Discussion

The model provides an insight into which topographic parameters best classify periglacial landforms. I observed that the combination of relative local relief and slope gradient had the greatest influence on the model. The results of the analysis suggest that the model can successfully classify bedrock, solifluction, allochthonous material, and blockfields. These results provide an insight into the direct and indirect influence of the chosen morphometric parameters on processes controlling the formation of periglacial landforms. Relative local relief and slope gradient are the drivers of the model, while relative local relief has the greatest impact on the model. This is expected because elevation governs environmental factors such as temperature and water availability, where and how sediment is formed and deposited, and the erosional history of a landscape, all of which help to control the processes forming landforms (Harris et al. 2011).

On Svalbard, blockfields are veneers of coarse regolith representing a non-glacial surface. They are areas of low gradient found at mountain summits or plateaus and are exposed to periglacial processes such as frost shattering. In Endalen there is evidence for the existence of a past glaciation on the plateaus (Landvik et al. 1998). Although, blockfields can remain undisturbed beneath cold-based glaciers but only form during periglacial conditions (Ballantyne 2010). The blockfields on Svalbard autochthonous because they form from in situ weathering of underlying bedrock (Goodfellow 2007) on the summits of mountains (Ballantyne 2010). Allochthonous blockfields are material derived from up-freezing of clasts in till or by the downslope movement of weathered material. According to Rea (2007) the transport mechanism defines the character of the landform as transport distances increase. The formation and preservation of blockfields are controlled by shallow slope gradient at high elevations (Rea 2007; Rixhon and Demoulin 2013).

Bedrock is exposed on the plateau edges of Svalbard because of a plucking mechanism caused by collapsing cornices formed from the accumulation of windblown snow by prevailing winds across the blockfields (Eckerstorfer et al. 2013). The annual removal of material maintains a steep rock surface. Bedrock has a high recall and low precision in Endalen and Ringdalen (Figure 3.10). This suggests that the model is classifying more bedrock than is actually there. I attribute this to mapping error because (1) many exposures are c.a. 10 m in length on the satellite imagery and therefore difficult to observe due to resolution, and (2) bedrock is mistaken for allochthonous material during interpretation of satellite imagery. Bedrock is frequently misclassified as allochthonous (Figure 3.10). Areas which have been identified as bedrock by the model are areas of steep slope where allochthonous material shouldn't form because regolith can't be retained on the hillslope (Figure 3.10). The main control on separating bedrock from other landforms is slope gradient (Figure 3.4). Studies by DiBiase (2012), Heimsath et al. (2012), Marshall and Roering (2014) have used a slope threshold to extract bedrock from high resolution elevation models. Milodowski et al. (2015) claim that a combination of topographic metrics such as slope gradient and topographic roughness can be used as a more robust feature extraction of bedrock from high-resolution data. Contrary to Milodowski et al. (2015) I found that topographic roughness had a small influence relative to slope gradient and relative local relief at classifying bedrock. However, in (Figure 3.8e) bedrock is detected to have low topographic roughness values on the slopes at the mouth of Endalen. This agrees with McKean and Roering (2004) observation that their roughness algorithm using the same eigenvector ratio as this study showed the presence of bedrock outcrops.

Of all landforms, the model couldn't classify scree correctly. In Endalen and Ringdalen scree is misclassified as solifluction and allochthonous material. Scree and solifluction share similar values of relative local relief and topographic roughness (Figure 3.4e). The classifier uses slope gradient to separate scree and solifluction.

Both scree and solifluction have different ranges in slope gradient (Figure 3.4). Despite this, the model can't distinguish between the two because their topographic positions are the same. In figure (3.10) the areas of solifluction which are classified as scree by the model are steep banks next to rivers. This is probably due to over-steepening of material by fluvial incision. Plug-like deformation is the dominant way in which solifluction moves in regions of continuous permafrost, and velocities decrease where gradient decreases downslope resulting in a pile-up of material (Matsuoka 2001a). The combination of similar hillslope gradient position and steep terrain are surface characteristics of scree, not discernible from solifluction.

I believe that active scree is being classified as allochthonous material and propose that these landforms are vegetated scree slopes (Figure 3.10). Both landforms share similar ranges of relative local relief, slope gradient, and topographic roughness values (Figure 3.12). Vegetated scree slopes have been observed in Tempelfjorden and have developed there because of a loss of source material, moisture, and fine-grained material from upslope (Rapp 1960a). Other studies have observed no difference in slope gradient between vegetated and non-vegetated scree (Hales and Roering 2005). The angle at which scree slopes form is dependent on the angle of residual shear of the parent material ranging from 30° to 40° (Sanders 2010). The location and activity of scree on a hillslope is dependent on a source of material from the bedrock above and therefore must occur lower on the slope. Rockfall is the primary process producing scree slopes. Rockfall onto scree slopes is either primary i.e. triggered by freeze-thaw activity on the rock face and subsequent downslope transfer of newly detached material i.e. rockfall. Secondary rockfall is where rockfall is dislodged by other rockfall, snow avalanches, water runoff or even cornice collapse. The cliff faces are dissected with channels that channel debris into accumulation corridors that open downslope into talus cones. Smaller rocks and finer material deposited onto the talus slope surface are washed or trapped in the interstitial voids between larger clasts.

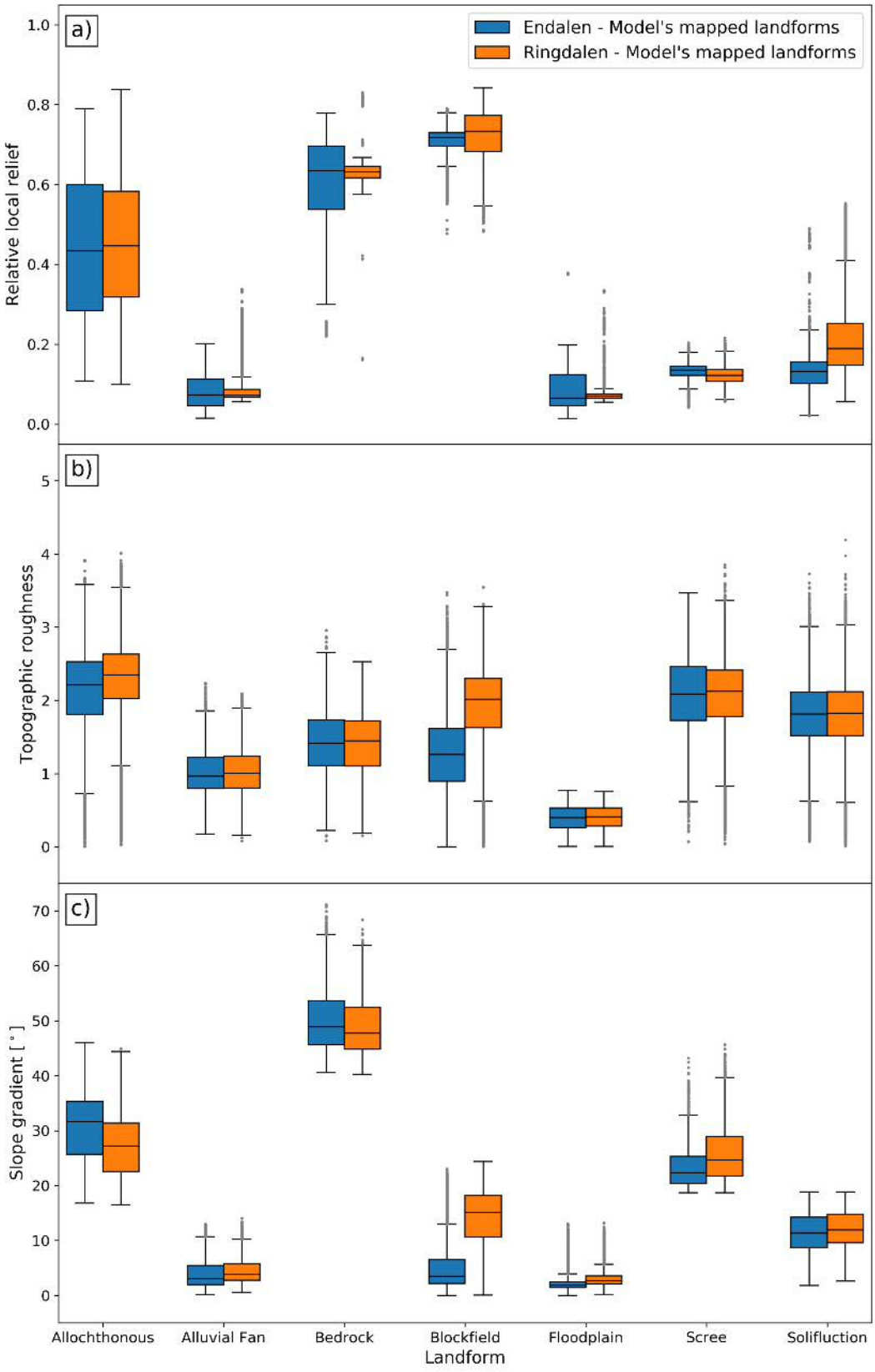

Figure 3.12 Box plots of landforms and their topographic parameters from the Endalen and Ringdalen models. a) Relative local relief. b) Topographic roughness. c) Slope gradient.

I found that the model could classify solifluction consistently well (Figure 3.10) and (Figure 3.11). Solifluction is classified at the base of hillslopes on low slope gradients (Figure 3.4), similar to field studies of solifluction on Svalbard (Akerman 2005; Harris et al. 2011; Matsuoka 2001a; Matsuoka and Hirakawa 2000; Akerman 1996). Other classification studies have found a slope and elevation niche for solifluction (Bartsch et al. 2002; Ridefelt et al. 2010) while others believe that slope is an important predictor because it is related to the potential energy and drainage patterns of the hillslope (Aalto and Luoto 2014). Relative local relief and slope gradient are closely linked to the mechanisms driving solifluction. Solifluction is more likely to occur where: (1) the substrate is a frost-susceptible non-cohesive soil. Bedrock above the solifluction sheets are composed of early Cretaceous sandstones, clay ironstones, and shales (Harris et al. 2011). The weathering of this bedrock produces large boulders/clasts and finer material of sand and silt. This weathered material is graded downslope so that the coarser material remains higher up the hillslope to form scree (Hinchliffe et al. 1998) while the finer material and some larger clasts are washed downslope to form a sandy-silt diamicton containing some sandstone clasts. This silty clay regolith is known to be frost-susceptible (Harris et al. 2011). A frost-susceptible soil is key for providing a medium for the growth of ice lenses; (2) Sufficient moisture is available for ice segregation and soil plastic limit. Soil moisture is dependent on the soil properties, ground ice accumulation, and surface/subsurface runoff (Matsuoka 2001a). With a shallow slope gradient, water doesn't drain away quickly and can accumulate. This has two effects, (a) continual water supply for ice lenses growth during autumn freeze back and (b) saturating the regolith to its plastic limit thus reducing the shear strength of the soil allowing it to deform downslope under its own weight; (3) Slope gradient is steep enough to initiate downslope self-weight shear stress. This has two effects on solifluction (a) it regulates the volume of sediment that can move and (b) controls the rate of sediment movement. During experimental simulations of solifluction it was found

that for a given slope gradient there is a positive correlation between the surface thaw settlement and surface downslope movements (Harris et al. 1996; Harris et al. 2008a; Harris and Smith 2003; Harris et al. 2008b). Too steep and the saturated soil will fail along a shear plane, become a debris flow, or water will drain away too quickly removing all the fine material and leaving the coarser material. Too shallow or no gradient and there will be an absence of the deformation component of gravity acting parallel to the slope i.e. no downslope movement. Therefore the soil will become waterlogged resulting in the possible formation of pore ice or other periglacial landforms. However solifluction has been found on gradients of up to 1° to 2° (Washburn 1980) while on Svalbard solifluction has been found to occur on slopes of between 2° and 36° (Matsuoka 2001a).

Alluvial fans and floodplains are indistinguishable according to the model. This is no surprise because both landforms exhibit similar topographic characteristics. The fluvial channels dissecting the surface of an alluvial fan are similar to the channels on floodplains. Both are at the base of the hillslope and have shallow slopes. The distinguishable characteristic between the two is their shape. Alluvial fans are fan shape while floodplains are linear. The classification model is pixel based and so to classify by shape requires an object-orientated analysis, which has proven successful in other studies (Dragut and Blaschke 2006; Ghosh et al. 2010).

The data shows that solifluction is one of the most extensive landforms within Endalen and Ringdalen (Figure 3.13). These study sites are favourable to solifluction because of regolith made of a frost-susceptible material, the wet environment caused by saturated ground encourages heaving during autumn freezback, and deep snow in the winter causes low-temperature gradients. Berthling et al. (2002) and Bartsch et al. (2002) believe it is an important mass-wasting process in cold environments, moving sediment through a catchment. The model is simple and uses parameters that reflect the important topographical controls on solifluction. Solifluction, a slow and continuous mass-wasting process, occurs in areas of continuous permafrost (Matsuoka

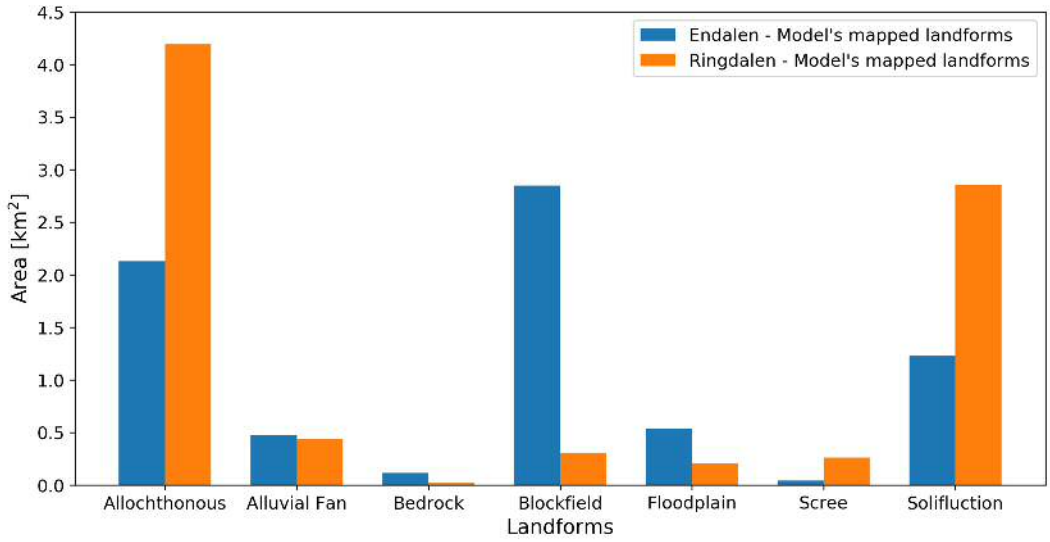

Figure 3.13 Bar chart showing the area occupied by each landform in the Endalen and Ringdalen models.

2001a). Back of the envelope calculations have shown that solifluction moves the greatest amount of material annually (Figure 3.15). I attribute this to a deeper active layer in Endalen (Harris et al. 2011). There are multiple ways in which the model can be improved. First, generalising the model by combining similar landforms into larger units. I briefly tested this by merging floodplains and alluvial fans into ''valley bottom" material and allochthonous material and scree into "loose hillslope" material. This improved model accuracy but at the expense of distinguishing more landforms. Second, additional landforms can be added by re-training the model. Other landforms which may be of interest to other researchers include moraines, debris cones, ice-wedge polygons, and avalanche deposits. However, adding more landforms would create more complexity. Third, I would add a step to remove misclassified pixels using a moving window to determine if the pixels surrounding the central pixel are the same. Nonetheless, the model developed in this chapter has a practical application for reconnaissance geomorphological mapping of large areas of unmapped terrain.

3.6.1 Sediment fluxes from Arctic landforms

Sediment flux was calculated using contact lengths that were >500 m between the landforms: (1) blockfield to allochthonous, (2) allochthonous to scree, (3) scree to solifluction, and (4) solifluction to fluvial (braided river and alluvial fan) (Figure 3.14). I used the following formula to calculate sediment flux

$$Sf = DVC \tag{3.5}$$

where Sf is sediment flux (m^3 a^{-1}), D is depth of movement (metres), V is velocity (m a^{-1}), and C is contact length between two landforms (metres); blockfields-allochthonous, allochthonous-solifluction and solifluction-alluvial fan/floodplain. In my calculation, I assume that sediment flux is caused by slow mass movement processes. At the blockfield-allochthonous contact, I chose a movement rate of 0.0025 m a^{-1} and a regolith thickness of 1 m, the average velocity and thickness of regolith on a blockfield in Wyoming (Anderson 2002).

To represent velocity and depth at the allochthonous-solifluction boundary I used a depth of 0.2 m and a creep velocity of 0.01 m a^{-1} (Rapp 1960a). For the solifluction-fluvial boundary I used a depth of 1.06 m and a velocity of 0.022 m a^{-1} (Harris et al. 2011). The data show that sediment flux increases downslope. Solifluction moves ten times the amount of sediment compared to other landform processes, making it a major denudating process (Figure 3.15). Studies in other periglacial regions have also found the same result concluding that solifluction is as important in sub-Arctic periglacial regions as mass-wasting processes are in alpine regions (Berthling et al. 2002; Ridefelt et al. 2010; Matsuoka 2001a). Other processes are known to transport sediment from blockfields such as cornice falls (Eckerstorfer et al. 2013) or from bedrock at the plateau edge (Siewert et al. 2012). There is a combination of processes such as bedrock fracturing by frost processes, avalanche falls, cornice falls, and fluvial erosion during summer months moving material to the lower slopes (Rapp

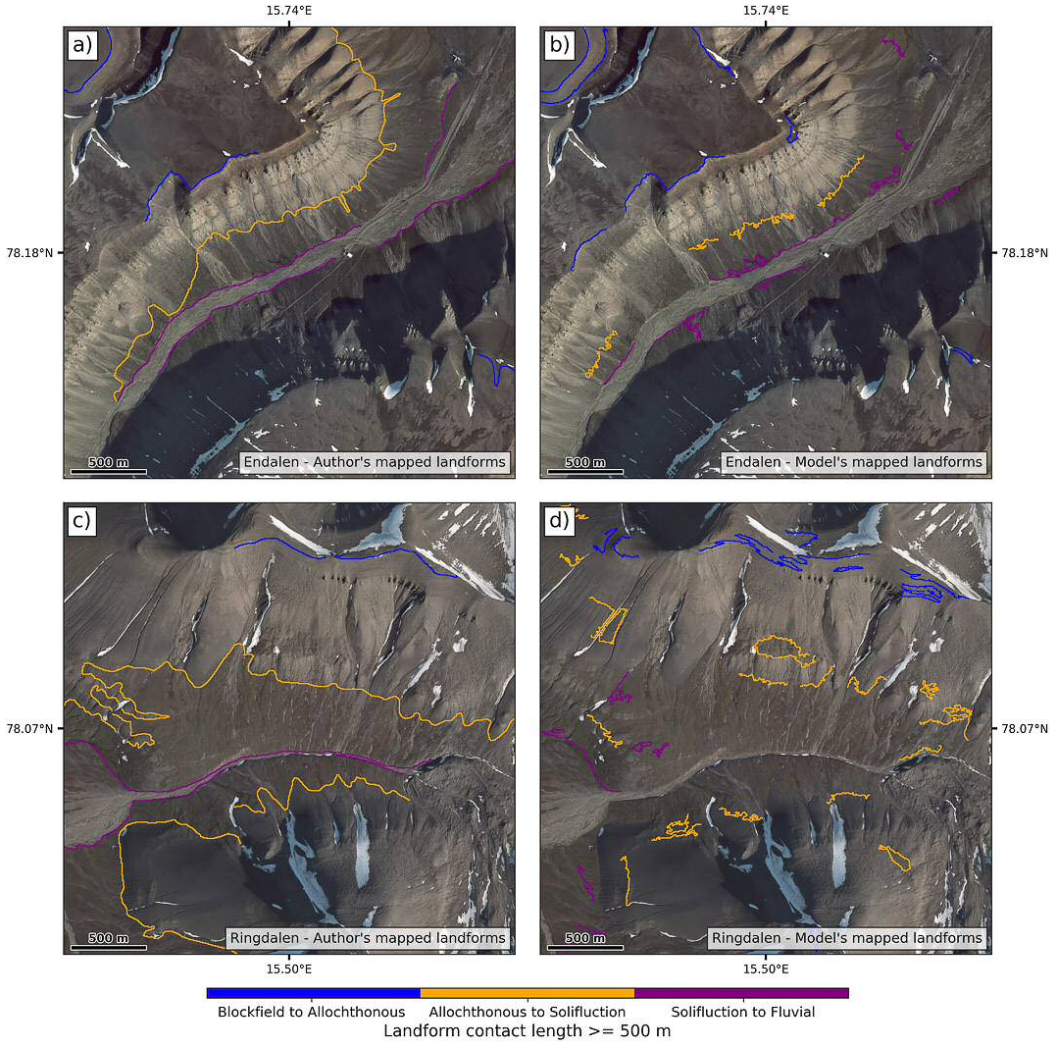

Figure 3.14 Series of maps comparing contact boundaries >500 m created from the author's maps and the model. a) Endalen author's map. b) Endalen model's map. c) Ringdalen author's map. d) Ringdalen models's map.

1960a), and rockfall caused by paraglacial debutressing (Ballantyne 2010) which I haven't taken into account in my calculations. These calculation are therefore an underestimate but still provide an insight into sediment routing in the Arctic. The major question is how can high fluxes of solifluction be sustained if the movement of sediment from upslope is so small? This could be because the deposit is glacial till with some input from periglacial erosion of bedrock. However, bedrock exposures are small according to the model and alone can't account for the large deposits today. Possibly frost-cracking was more intense in the past with more exposures

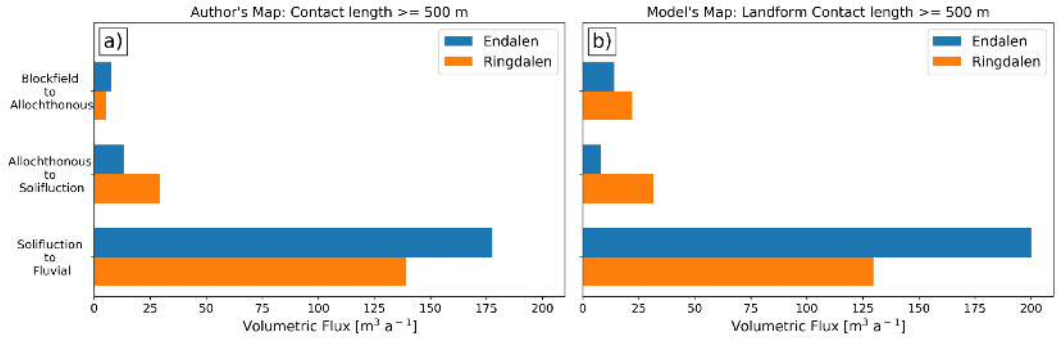

Figure 3.15 Bar charts comparing the sediment fluxes of each landform in Endalen and Ringdalen. a) Author's map. b) Model's map.

of bedrock at the top of the hillslopes. Other mechanisms can contribute to the flux of sediment downslope from allochthonous material and solifluction such as sheet slides, mudflows, slope wash, and rill erosion. I would expect that the flux of sediment to be greatest on the steepest slope i.e. in the allochthonous material.

The sediment moved by solifluction is greater in the model when compared to the author's map. The author's map generalises boundaries between landforms and assumes each landform as a uniform unit. The model classifies each pixel; therefore each landform unit isn't uniform and can contain clusters of pixels of a different landform, increasing the contact length between landforms. This exposes a weakness of the model. Conversely, these calculations are preliminary and an indicative estimate of sediment flux because they are based on velocity and depth estimates of uncertain representativeness.

3.7 Conclusion

The aim of this study was to create a simple and automated landform classification model using topographic parameters that reflect processes and quantify the spatial extent of landforms, and demonstrate that solifluction is an important denudating process in a mountainous periglacial environment. From this study I draw the following conclusions:

1. A combination of relative local relief, slope gradient, and topographic roughness in an LDA were the three topographic parameters that could best classify the study sites in Endalen and Ringdalen.

2. The model performed best at distinguishing blockfields, allochthonous material, bedrock, and solifluction. Scree couldn't be distinguished from the vegetated allochthonous material, suggesting a similar genesis for both landforms. Bedrock was mapped by the model at a higher resolution compared to manual mapping.

3. Distinguishing between alluvial fans and floodplains was problematic for the model. However, this could be resolved by combining the model with an object-orientated analysis to separate theses landforms based on shape.

4. In Endalen and Ringdalen solifluction and scree slope development are the most important denudating processes. However, this is based on preliminary sediment flux calculations and can only be an indicative estimate of sediment.

5. The model was a qualified success rather than an outright success and could be improved by applying a moving window filter to remove misclassified pixels or by lumping certain landform categories.

6. This work has the potential as a reconnaissance geomorphological mapping tool for large areas of mountainous Arctic landscapes.

7. Future work should focus on applying the model to a landscape in other continuous permafrost regions to find areas of solifluction and narrow search areas for ALDs.

Chapter 4

Spatial controls on the distribution of active layer detachments, Alaska

4.1 Summary

The Arctic is warming at twice the global average, bringing warmer and wetter weather, which facilitates the propagation of thaw fronts quicker and deeper into the ice-rich layers of cold permafrost. The thawing of ground ice at depth generates excess pore pressures which reduce the shear strength of soils causing failure along the thawing plane permafrost boundary. The frequency of these failures, called ALDs, are expected to increase in the future. In this chapter, I investigate the topographic constraints of ALDs and other landforms. To do this, I applied the landform classification model from chapter 3 to the Brooks Range, Alaska. I then developed a 2-D slope stability model to assess the impact of pore pressures on landscape stability. I found that the classification model performed well in regions of high relief but underperformed in low relief settings. Interestingly, mapped ALDs are coincident with convergent topography on soliflucting hillslopes. This suggests that the higher moisture availability feeds the growth of ice lenses, increasing ground

ice content. ALDs are more likely to initiate as thaw fronts reach deeper into cold permafrost.

4.2 Introduction

With the Arctic warming at twice the rate of the global average (Cohen et al. 2014) it is believed that more frequent extreme warming and precipitation events will occur in the Arctic (Lewkowicz and Harris 2005a; Bintanja and Andry 2017). Permafrost is thawing rapidly and the active layer has deepened across the Arctic (Akerman 2005; Pastick et al. 2015). Warmer and wetter weather facilitates the quicker and deeper propagation of thaw fronts into the ice-rich basal layer of the active layer causing rapid thaw of ground-ice and increasing hillslope instability (Lewkowicz and Harris 2005a). As a result, it is predicted that the frequency of landslides will increase with a warming Arctic (Lewkowicz and Harris 2005a). Understanding the spatial distribution of landslides in the Arctic is in its infancy, but may provide a useful tool for understanding how future warming may affect the spatial distribution of ALDs.

Statistical analysis and modelling of landslides is common in regions experiencing coseismic landsliding (Parker et al. 2017) and/or high rates of precipitation (Westen et al. 2008). In the Arctic, translational landslides called ALDs initiate in the summer after a long period of warm weather and/or high rainfall (Lewkowicz and Harris 2005b). Recent studies have discussed the topographic constraint on ALDs. Rudy et al. (2016) found that ALDs on Melville Island, Canada were more likely to occur on slopes of between 3° and 10° and on north-facing slopes. Balser et al. (2015) created an ALD suitability map of the Brooks Range in Alaska using landscape properties such as geomorphology, vegetation, topography, surficial geology, and lithology. They found that ALDs form on smooth low relief hillslopes with silty clay colluvium and in water tracks. Swanson (2014) mapped 2246 ALDs in the

Brooks Range and found that the majority occurred on slopes of between 5° and 39° on north-west facing slopes in glacial and solifluction deposits.

This chapter seeks to understand the distribution of ALDs across mountainous Arctic landscapes. I seek to test two hypotheses, (1) that ALDs are more likely to occur in areas of solifluction, and (2) that most ALDs form in areas of high topographic convergence, where ground ice concentrations are likely to be highest. To do this I modified the landform classification system I developed in chapter 3 for the Brooks Range, a region that has a historical record of ALD activity (Swanson 2014). Comparison of the landform model with the mapped distribution of ALDs allowed for the assessment of possible topographic characteristics that govern ALD initiation. After identification of areas of potential solifluction in the Brooks Range, I assessed the relationship between the channel network and the distribution of ALDs. Finally, I modelled the potential for ALDs in the topography of the Brooks Range using a slope stability model. In the model, I assumed that areas within the channel network had a higher ground ice content, and therefore higher excess pore pressures during warming.

4.3 Study area

4.3.1 Study area: Brooks Range

The Brooks Range, Alaska has a historical record of ALDs that have been part of a number of studies (Bowden et al. 2008; Balser et al. 2009; Gooseff et al. 2009; Osterkamp et al. 2009; Mann et al. 2010; Kokelj and Jorgenson 2013; Balser et al. 2015; Blais-Stevens et al. 2015) (Figure 4.1). Permafrost is continuous (Jorgenson 2009) and annual air temperatures are -8.2°, recorded at the Remote Alaska Weather Station (Swanson 2014). Much of the Brooks Range is mountainous with U-shaped

glacial valleys and steep topography. The topography is highest in the east and decreases in elevation and relief towards the west.

The central Brooks Range has low relief topography with gentle sloping hillslopes of sandstone, marine shale, limestone and chert (Wilson et al. 2015). To the north is the gently sloping and marshy Arctic coastal plain, which extends to the Arctic Ocean. Much of the Brooks Range was glaciated during the late Pleistocene c.a. (2.6 ma to 0.117 ma), with the most recent glacial event depositing till and lacustrine sediment on the valley sides and floor (Hamilton 2009). On steeper slopes a regolith of scree and glacial till exists, forming colluvium (Balser et al. 2015). Vegetation is absent or sparse on steeper terrain where scree production is active (Balser et al. 2015). On shallower terrain, vegetation is primarily alpine and sparse (Mann et al. 2010). On lower slopes where regolith is thicker, shrub and Arctic tundra vegetation often exists (Trochim et al. 2016a). I investigated two sites in the Brooks Range. The first, Saviukviayak (Figure 4.1), has a similar topography to Svalbard which provides an opportunity to test the landform classification model developed in chapter 3 to a different landscape. The second, Nukatpiat (Figure 4.1), is an area of extensive ALD formation. A limiting factor for choosing study sites in the Brooks Range was the availability of high-resolution satellite imagery and DEM coverage.

Study area 1 - Saviukviayak

The Saviukviayak study site is located in the eastern half of the Brooks Range (66.77° N 147.48° W) (Figure 4.1). The landscape is mountainous, with 600 m of relief and a wide range of mountain landforms (Figure 4.1). It is a mountain range that is qualitatively similar to Endalen and Ringdalen, Svalbard. A braided river system called Saviukviayak traverses the valley with steep slopes rising from the valley floor from 845 m to 1445 m at the ridge summits (Figure 4.1). Bedrock is mainly chert

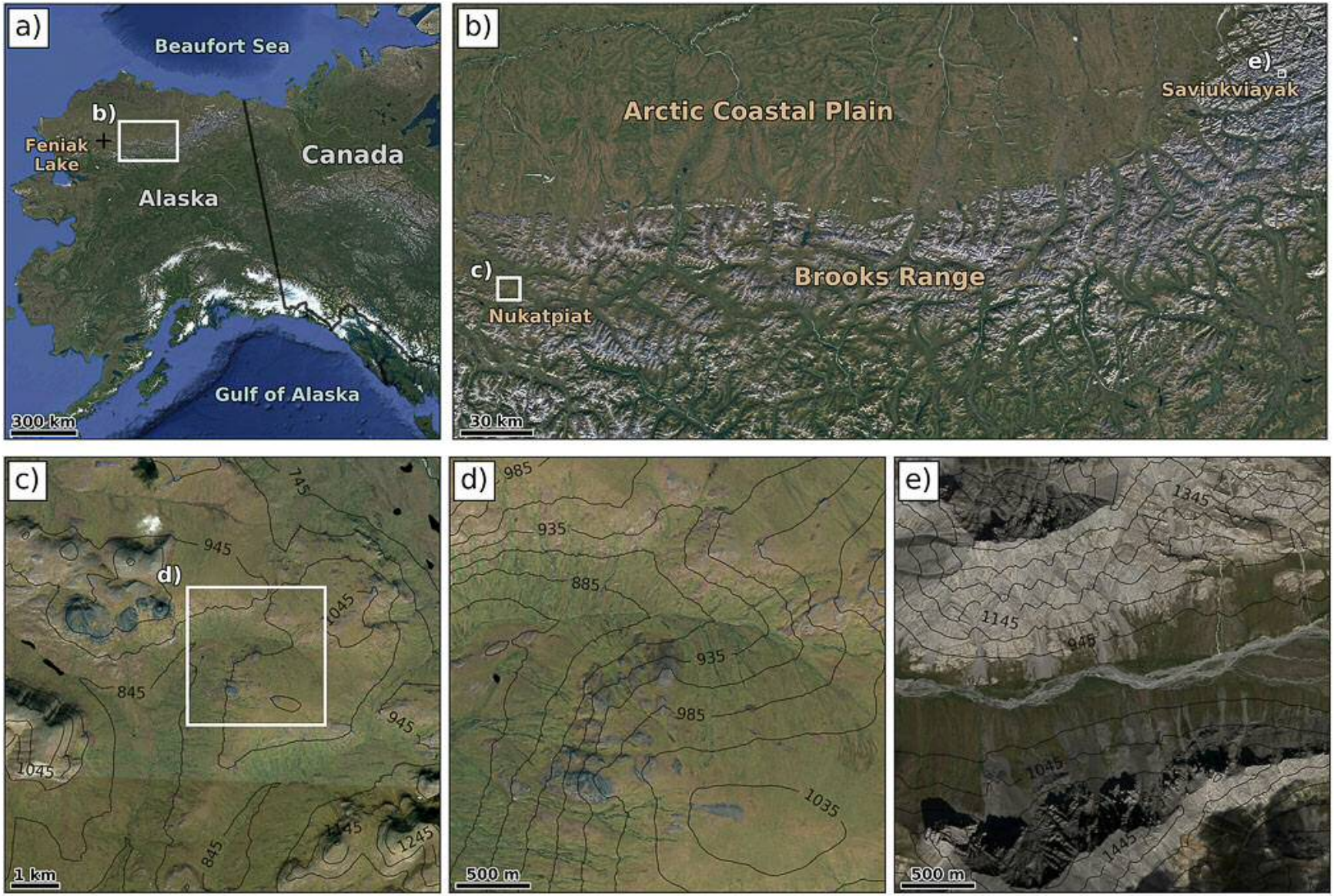

Figure 4.1 Location map. a) Alaska. b) Brooks Range. c) Nukatpiat 100 km^2. d) Nukatpiat 10 km^2. e) Saviukviayak 10 km^2. Contours are in meters. Satellite imagery from Google Earth.

and limestone with superficial deposits of glacial drift and colluvium (Wilson et al. 2015).

Study area 2 - Nukatpiat

The Nukatpiat (68.01° N 155.85° W) study site is 105 km south-east of Feniak Lake (Figure 4.1). It is a region of low relief with rounded hillslopes dissected by stream networks (Swanson 2010; Swanson 2014; Balser et al. 2015). In the 100 km^2 region topography rises from 645 m in the north-east to 1245 m in the south, although there are variations in relief across the area (Balser et al. 2014; Swanson 2014). Steeper slopes and higher relief exist as 'islands' amongst the smoother, lower gradient terrain. Lakes are spread out across the region and are found at the base of valleys (Balser et al. 2015). Vegetation consists of low shrub tussocks with water tracks of wet sedge meadow (Balser et al. 2015). An exceptionally warm summer in 2004 was measured at central Noatak National Preserve (Swanson 2014). This summer is thought to have triggered 2246 ALDs (Swanson 2014). No unusual precipitation event preceded ALD initiation (Swanson 2014), therefore I assume that ALDs in Nukatpiat initiated exclusively by pore pressures generated from the thawing of ice lenses.

4.4 Methods and materials

I investigated the spatial distribution of ALDs and solifluction by using the model developed in chapter 3. Observational evidence from Arctic landscapes suggests that areas of solifluction are particularly prone to ALD initiation (Harris and Lewkowicz 2000; Lewkowicz and Harris 2005b). I extracted areas of solifluction and developed a method for identifying ALDs using drainage area thresholds.

4.4.1 Topographically based landform modelling

To model the distribution of landforms as a function of topography, I used the LDA-based landform identification model from chapter 3. While the details are discussed in the previous chapter, I summarise the key elements here. I trained the LDA classifier using mapped polygons from Endalen and Adventdalen, Svalbard. Using the extracted pixel values for each landform, I ran the LDA classifier on a training dataset composed of 70% of the pixel values and validated it both on the remaining 30% of the training areas and across broader sections of Svalbard.

Using a five-metre resolution Interferometric Synthetic Aperture Radar (IFSAR) derived DEM (USGS 2015), I applied the model with the parameter values extracted from Svalbard. For the landform classification analysis of Saviukviayak, I used a 10 km^2 area (Figure 4.1). For the landform classification analysis of Nukatpiat, I sampled a 10 km^2 area from within the 100 km^2 area (Figure 4.1). I made one minor modification for the analysis in Nukatpiat; rather than use relative local relief, I used an absolute local relief metric (Ar), which is calculated as

$$A_r = x - x_{min} \tag{4.1}$$

where x is the elevation of a particular landform pixel and x_{min} is the minimum elevation within a 5 km radius of the focal point. The purpose of the absolute relief metric is to better represent the elevation dependent processes, particularly block-fields, which found at higher elevations in Arctic mountains and are not common in lower relief landscapes.

4.4.2 Analysis of ALD locations within Arctic drainage network

I tested the hypothesis that ALDs were more likely to initiate within or immediately upstream of the channel network by comparing the mapped extent of ALDs with

different drainage networks defined by different drainage thresholds (i.e. using the assumption that channel networks initiate at consistent drainage areas, Montgomery and Dietrich (1992)). This involved the derivation of a drainage network and mapping of ALDs for comparison with the distribution of channels.

First, I mapped 150 ALDs using 2008 satellite imagery from Google Earth within the Nukatpiat study area (Figure 4.1 and 4.5). An ALD was defined as a region of exposed earth, brown in comparison to the green vegetation, with a runout zone of compressed regolith. I mapped both the runout and exposed earth as one ALD polygon. The mapped ALDs represent those initiated during a single event that occurred during an unusually warm summer in 2004 (Swanson 2012; Swanson 2014). This is evidenced by the lack of change in the ALD count for images from 2006 and 2007.

I then assessed whether ALDs were more likely to occur within areas of convergent topography by comparing the distribution of ALDs with drainage networks of different sizes (Figure 4.2). I created a drainage area raster using the D8 flow algorithm in ArcMap (ArcGIS 2013). The D8 flow algorithm directs the flow down the steepest path in one of eight cardinal directions. I then used the threshold drainage area method (Montgomery and Dietrich 1994) to derive a stream network. I created stream networks using ten different drainage area thresholds from 12,500 m^2 to 125,500 m^2. ALDs have a width that is greater than the channel network, so to account for the proportion of the ALDs that is outside the channel network I introduced a buffer of varying widths to the channel network. I applied buffers around each stream network, varying in width from 10 m to 100 m in increments of 10 m.

For a given buffer and drainage area I calculated the total area of ALDs and study are captured.

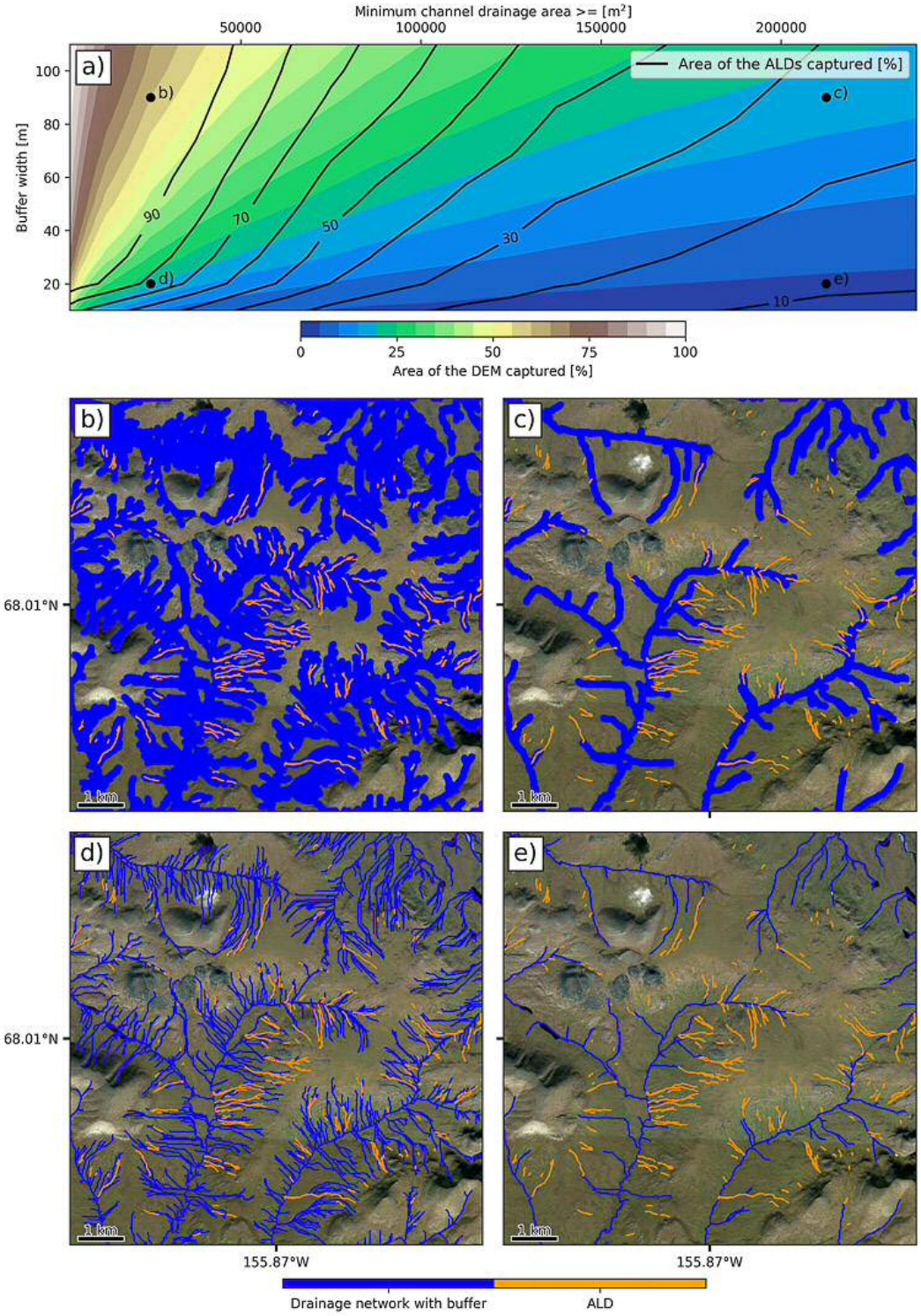

Figure 4.2 a) Contour plot showing the percentage area of the DEM captured by the buffer (in colour), and the percentage are of ALDs captured by the buffer (black lines). b to e) show varying buffer and drainage sizes, see 'a)' for their locations on the contour plot. Each is underlain with a satellite image from Google Earth.

4.4.3 Slope stability analysis

Once I had identified the distribution of ALDs relative to the channel network, I sought to understand whether the upper part of the channel network (I define as the 'buffer') was more prone to failure than other parts of the landscapes. Hence, I derived a spatially distributed slope stability model for ALDs, where I solved the infinite slope equation in space and varied the pore pressure as a function of presence or absence of a drainage network.

The planar infinite slope model is an effective tool for modelling ALDs, where the depth of the slide is small relative to the length of the slide plane (Skempton and DeLory 1957). The infinite slope model is governed by the balance of shear stress and shear strength and is commonly formulated as follows

$$FofS = \frac{c' + z(\gamma - m\gamma_w)\cos^2\beta\tan\phi'}{z\gamma\sin\beta\cos\beta} \tag{4.2}$$

where $FofS$ is the factor of safety, c' is effective cohesion, termed cohesion from this point onwards, ($ML^{-1}T^{-2}$), z is depth of the slip surface (L), γ and γ_w are the unit weight of soil and water respectively ($ML^{-2}T^{-2}$), β is the slope gradient, ϕ' is the effective angle of friction. The term m is the ratio of the height of the water table above the slip surface to the depth of the slip surface and is the representation of pore pressure

$$m = \frac{h}{z} \tag{4.3}$$

I vary m to simulate the excess pore pressures due to ice (essentially setting m to be up to 1.5).

I calculated $FofS$ across the landscape using a spatial distribution of parameter values that depended upon landform type and degree of topographic convergence. First, the landform model identified parts of the landscape that were likely to be

soliflucted material and those that were likely to be something else (usually bedrock, scree, or other allochthonous material). These generally contain coarse-grained sediments that cannot develop ice lenses (Harris and Lewkowicz 2000) and are unlikely to generate excess pore pressures. Whereas areas of solifluction can develop excess pore pressures, of up to 1.5 time hydrostatic (Harris and Lewkowicz 2000). Secondly, the distribution of excess pore pressures within solifluction varied as a function of convergence. Areas within the channel network (buffer), defined using a 20 m buffer and 25,000 m^2 minimum drainage density (Figure 4.2), were able to generate excess pore pressures of either 1 (static pore pressure), 1.2 (calculated from Harris et al. (2011)) or 1.5 (calculated from Harris and Lewkowicz (2000)). Those pixels that were identified as solifluction but were outside the channel network (buffer) were given values of 1, 1.032, and 1.29. The reduction of excess pore pressure reflects the observation of a 14% reduction in pore pressure for a soliflucting slope when compared with a slope at failure (Harris et al. 2011). Prior to analysis, I removed pixels from all rasters that included water bodies such as lakes and visible water channels in the satellite image (Figure 4.5).

I created a series of controlled experiments to assess the relationship between the amount of excess pore pressure generated from thawing ice lenses and the depth of ice lens thaw for different values of cohesion (Table 4.1). I then tested the difference in the distribution of $FofS$ as a function of thaw depth and excess pore pressure for different values of cohesion. Material parameters were kept constant across the landscape, based on measurements made by Harris and Lewkowicz (2000) and Harris et al. (2011). The material parameters given to each 'landform' is summarised in (Table 4.1).

Table 4.1 Model input parameters. Allochthonous values from [a]Lacerda et al. (2004) and solifluction values from [b]Harris and Lewkowicz (2000) and [c]Harris et al. (2008c)

Parameter	Unit	Allochthonous	Buffer	Solifluction
Cohesion in scenario 1	kPa	10[a]	0	0
Cohesion in scenario 2	kPa	10[a]	2[b]	2[b]
Cohesion in scenario 3	kPa	10[a]	4.8[c]	4.8[c]
Internal angle of friction	°	37[a]	19[b]	19[b]
Unit weight of soil	kN/m^3	16.46[a]	19.62[c]	19.62[c]
Unit weight of water	kN/m^3	9.8	9.8	9.8
Static pore pressure factor	-	1	1	1
Excess pore pressure factor 1	-	1	1.2	1.032
Excess pore pressure factor 2	-	1	1.5	1.29

4.5 Results and discussion

4.5.1 Landform Classifications: Svalbard versus the Brooks Range

The spatial classification of mountainous Arctic landscapes developed in Svalbard (chapter 3) performs extremely well when compared with a similar mountainous landscape, Saviukviayak, Brooks Range (Figure 4.3). I used the same classifiers in Saviukviayak as in Ringdalen and Endalen, which suggests that landforms in Arctic mountains are governed by processes that generate similar topography, regardless of the specific geography. Furthermore, the success of the classification across mountains that form in different climatic and tectonic settings, although with similar lithologies, suggests that topography can provide a useful first-order tool for understanding the distribution of Arctic landforms. However, the classification underperformed in Nukatpiat (Figure 4.4), where the terrain is shallower and rounded. This is likely one of scale, in that a classification designed for mountainous regions is choosing from a large number of potential landforms. When the number of landforms is reduced, the classifier still looks to classify a wide range of landforms when only one or two might exist. I will examine the details of the classification in each of the two locations in more detail.

In Saviukviayak (Figure 4.3), the spatial classification modelling results were very similar to those in Svalbard. Initially, when the model was run, separating landforms of similar topographies (e.g. allochthonous material and scree) the model performed poorly with an overall accuracy of 17.44%. This poor result is primarily because of the misclassification of 85.25% of mapped scree slopes as allochthonous material (Figure 4.3). The LDA model is only effective at separating first-order differences in developing a classification, so it will always have difficulty separating

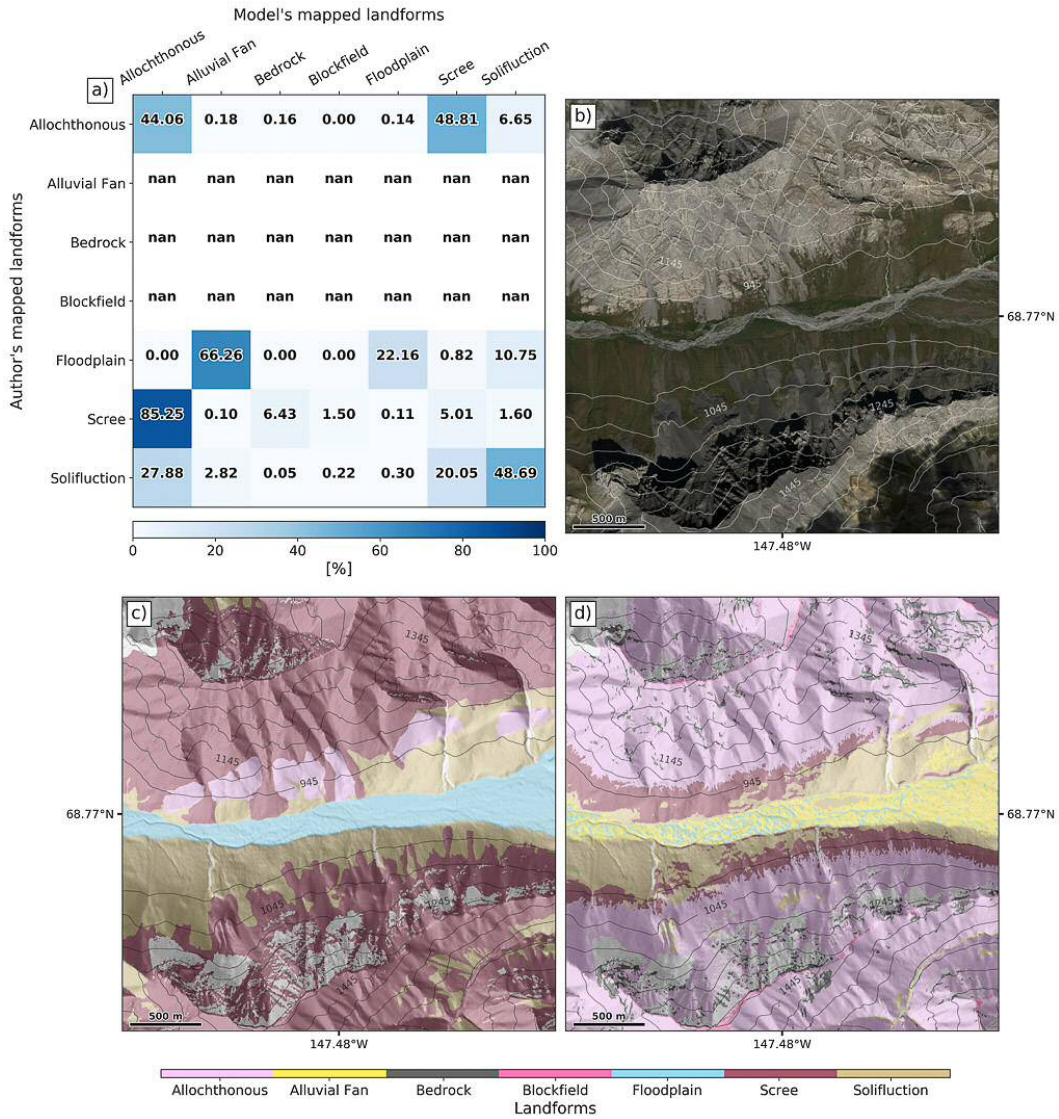

Figure 4.3 Saviukviayak results. a) Confusion matrix. b) Satellite image from Google Earth. c) Author's landform map. d) Model's landform map. Contours are in metres. Figures c and d are underlain with a hillshade. 'nan' are no data values.

these two parameters. When I pool allochthonous and scree classifications, the overall model accuracy increases to 70.32%. A surprising result of the model was the identification of blockfields, which in the geomorphological mapping are thought to be arêtes. Areas identified as blockfields are narrower than those on Svalbard but connect mountain peaks, suggesting that they may be an extant feature. As discussed in chapter 3, identification of bedrock from satellite imagery is challenging due to shadows and glare. The topographic roughness that defines bedrock may be a better indicator of the distribution of this landform. In Saviukviayak I found bedrock primarily amongst scree and allochthonous material (Figure 4.5). The model identifies bedrock within 500 m of the summit blockfields and ridges but none are found below the 1045 m contour which could depict a past glacial trimline (McCarroll and Ballantyne 2000) or the upper runout limit of weathered bedrock from the upper slopes. Bedrock is modelled at the top or on the side of cwms/gullies where I find the deposits of allochthonous and scree material. Solifluction sheets are the dominant landform on the lower slopes in the Brooks Range. However, in the mapping area solifluction was less common than in Svalbard. The model identified fluvial deposits at the base of the valley. However, 66.26% of the mapped floodplain deposits are misclassified as alluvial fan deposits and the other 10.75% as solifluction (Figure 4.3), because in the centre-right are areas of low slope and low roughness which is characteristic of floodplain and alluvial fan landforms.

The classification of landforms within the lower relief Nukatpiat site was less successful with an overall accuracy of 61.1%. The model misclassified 59.33% of the solifluction area as blockfield and 55.34% of the mapped allochthonous material as blockfield within the 10 km^2 study area. The geomorphological mapping identified two major landforms; solifluction and allochthonous material. In contrast, the classification included all of the major landforms except bedrock. This highlights a clear challenge of using a pixel-based classifier that is calibrated for a high-relief region on areas of lower relief. One of the obvious reasons for misclassification is

the reliance of the classifier on the relative local relief metric, which calculates the landform type based on the elevation of a pixel relative to the elevation of all pixels within a study area. There are four reasons for this: Firstly, this metric is the strongest driver of the classification of blockfields and fluvial landforms, forcing classification of the highest and lowest pixels of any landscapes as these landforms; Secondly, the relative local relief parameter was trained on Svalbard where topography is steeper and relief is greater, a contrast to Nukatpiat Mountain where topography is smoother with lower relief. Hence, many of the landforms identified on Svalbard do not exist in Nukatpiat Mountain; Thirdly, the model needs to classify every landform; Finally, the lack of an alluvial river system in Nukatpiat Mountain, means that channels cannot be readily identified.

Hence there is a challenge in comparing a mountainous, glaciated landscape, with cold permafrost landscapes with a history of continental glaciation. In the case of Nukatpiat Mountain the 'valley bottoms' are dissected by 5 m wide channels cutting into colluvium or glacial till and the valley sides are gradual, low gradient slopes.

I modified the classification system to adjust for the misclassifications caused by using an absolute local relief parameter. Pixels were classified based on their position relative to the total local relief (defined as the difference between the minimum and maximum elevations in a circular area with a 5 km radius), after Montgomery and Greenberg (2000).

The change in relief characteristics improved model performance by removing the need for the model to place blockfields at the highest elevations. The model correctly identified 73.92% of the mapped area of solifluction (Figure 4.4). However, 24.67% of the mapped solifluction is identified as alluvial fan deposits by the model, with the rest being floodplain (Figure 4.4). This issue of misidentifying lower pixels as alluvial fans and floodplains, when they should be solifluction near the base of hillslopes still exists. Beyond reclassifying this landscape to account for the lack

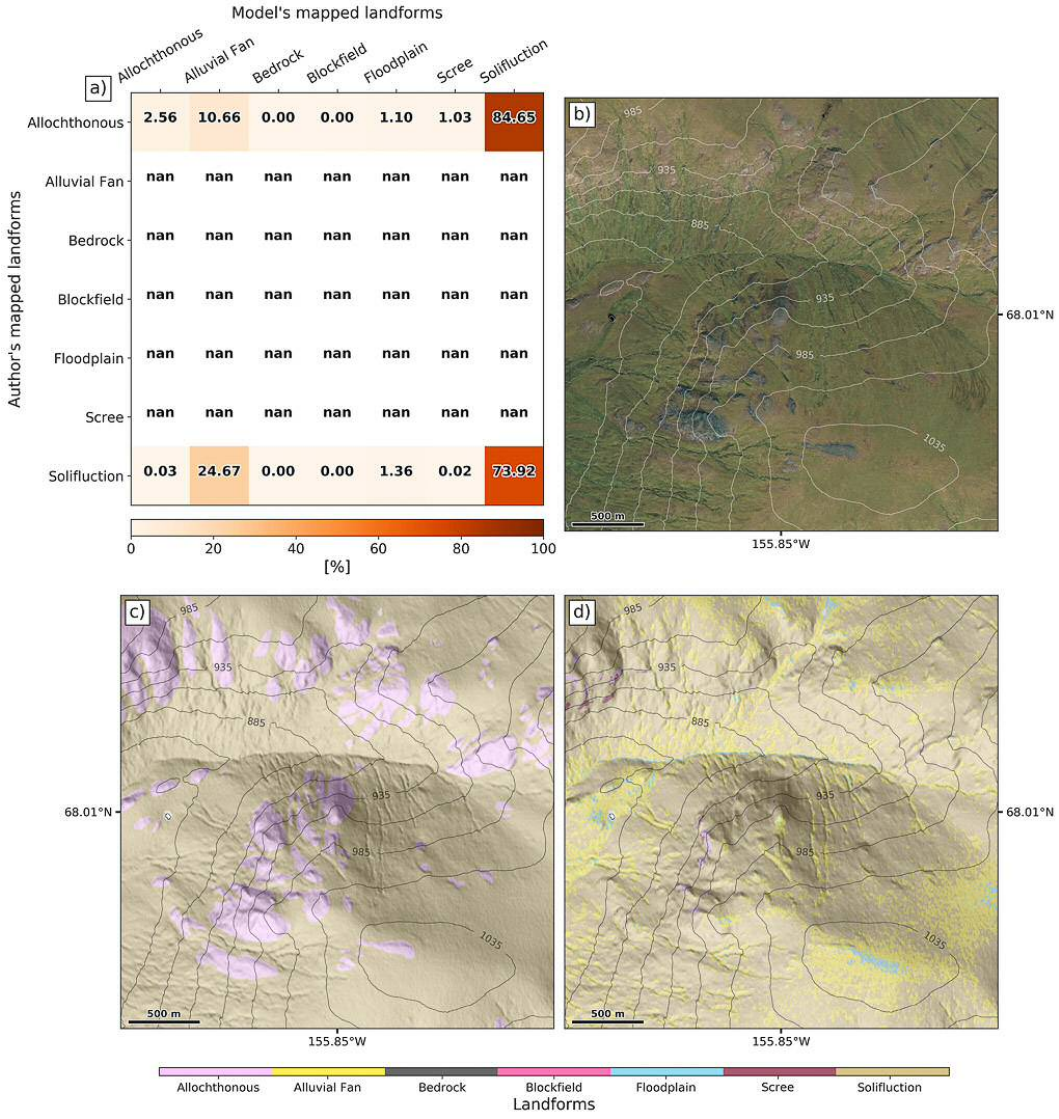

Figure 4.4 Nukatpiat results. a) Confusion matrix. b) Satellite image from Google Earth). c) Author's landform map. d) Model's landform map. Contours are in metres. Figures c and d are underlain with a hillshade. 'nan' are no data values.

of an alluvial river system, the impact of these misclassifications is small as they always misclassify solifluction pixels.

When I applied the model to an expanded, 100 km^2 area around Nukatpiat Mountain (Figure 4.1) the classifications became less accurate. At this scale, the total local relief of the area is of similar magnitude to Svalbard, despite being of lower relief. Hence, areas of solifluction were classified as blockfield. This is probably because in the north-east corner is a braided river system at an elevation

of c.a. 645 m (Figure 4.1). The highest point is at c.a. 1245 m, an elevation difference of 600 m (Figure 4.1). To improve the accuracy of the classifications for this area future researchers could re-train the model for a broad shallow gradient landscape or remove the elevation dependent variables and use elevation derivatives, such curvature, topographic openness (Prima and Yoshida 2010), slope aspect, and topographic wetness (Beven and Kirkby 1979). However, this would add more complications to the model and in chapter 3 I tested, by using a recursive feature elimination analysis, many topographic parameters and found that the top three were relative local relief, topographic roughness, and slope gradient. Due to this, I created my own geomorphology map of the 100 km^2 study area and used this in any further analysis (Figure 4.5).

4.5.2 Spatial Distribution of ALD

The purpose of utilising the landform classification model is to try and understand the distribution of ALD across the Brooks Range. A pixel-based classification for ALD is

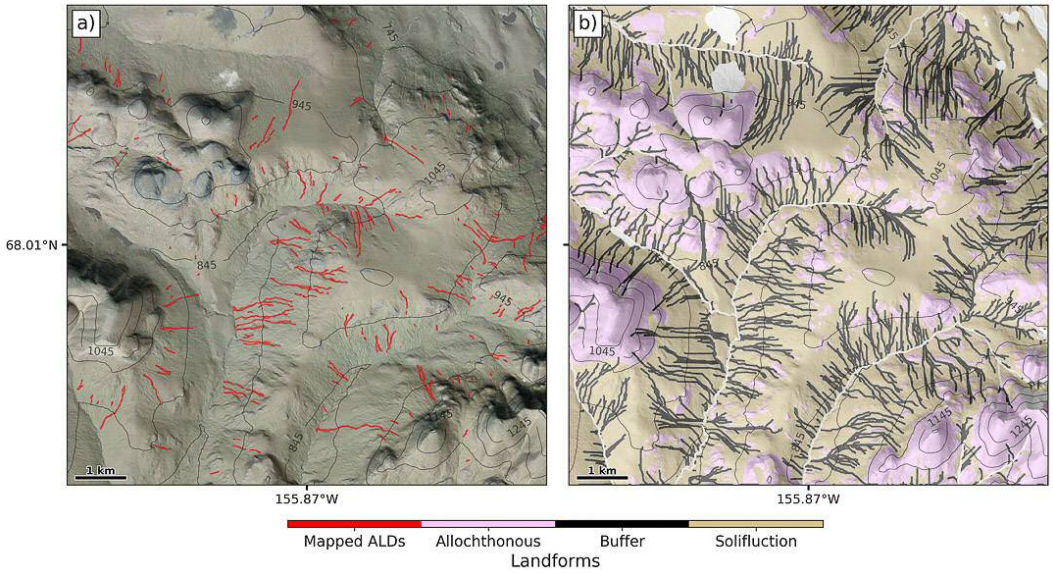

Figure 4.5 Nukatpiat 100 km^2. a) Mapped active layer detachments by the author. Satellite image from Google Earth. b) Landform map created by the author. The white area represents no data. Both maps are underlain with a hillshade.

difficult for three reasons: Firstly ALDs have a particular shape, many being elongate but also compact (Lewkowicz and Harris 2005a). A pixel-based classification cannot identify shapes, and would require an object-orientated analysis instead (Dragut and Blaschke 2006; Asselen and Seijmonsbergen 2006). However, in this study my aim was to understand the topographic controls on landforms rather than replicate their shapes; thus I didn't pursue the object-orientated method. Secondly, Swanson (2014) notes that many ALDs in the Brooks Range initiated during a warm period in the summer of 2004, re-vegetating within five years. The satellite imagery I used to map the ALDs are from 2008, while the IFSAR derived DEM is a combination of multiple IFSAR collections from 2006 to 2013. Therefore, some areas of mapped ALDs may have initiated after the DEM was captured. In addition, the topographic impression of ALDs is below the vertical resolution of the DEM, with failure scars only at maximum 3.5 metres depth (Balser et al. 2015). Finally, ALDs have similar topographic characteristics as solifluction at the pixel scale, making a pixel-based method inefficient for classifying ALD. The similar topographic characteristics combined with observations from satellite imagery, suggests that ALDs initiate on soliflucting hillslopes as observed in field studies (Lewkowicz and Harris 2005a).

A common observation in field studies of ALD initiation is that they have a tendency to form in areas of topographic convergence (Lewkowicz 1990). Hence, I compared the distribution of ALDs with the distribution of channels within the Nukatpiat Mountain area. This analysis demonstrated a strong spatial correlation between the channel network and the location of ALDs (Figure 4.2). Because the D8 method of deriving a channel network creates a network that is composed of individual pixels, I introduced a buffer around the drainage network. The buffer accounts for the width of ALDs being greater than a single pixel in the DEM. If ALDs are more common in the drainage network than outside of it, I would expect that the buffer width would be small, on the order of the width of an individual ALD (20 m to 50 m). In contrast, if ALDs were more common on hillslopes rather

than channels, then buffer widths would be high or the threshold drainage areas to create the drainage network would be low. Figure 4.2 presents a sensitivity analysis that compares the distribution of mapped ALDs relative to the critical drainage threshold and buffer width that is chosen. Unsurprisingly, as the critical drainage area increases fewer ALDs coincide with the channel network. This is because a lower critical drainage threshold is more likely to coincide with fluvial sediment transport, which is demonstrated by the coincidence of the channel network with evidence for channelization in the satellite imagery. At critical drainage thresholds of below 75,000 m^2 and low buffer widths, small changes in critical drainage area result in large changes in the number of ALDs that are found within the drainage network. For a given drainage area, increasing the buffer width does not cause a significant increase in the number of ALDs found within the drainage network. Taken together, the sensitivity analysis suggests that ALDs have a greater propensity to form in the upper part of the drainage network on soliflucting slopes.

Why would areas of topographic convergence be more likely to initiate ALDs? A similar relationship between convergence and landslide initiation can be seen in shallow landsliding systems in warmer climates (Montgomery and Dietrich 1994; Pack et al. 1999; Montgomery et al. 2000; Talebi et al. 2008). In these warmer climates, during prolonged, intense rainfall events, convergent topography drives a larger amount of throughflow (flow through the soil), which accumulates in unchannelised valleys and increases pore pressures within the soil column and drives landslide triggering (Montgomery and Dietrich 1994). As rainfall is only a secondary driver of ALD initiation, it is unlikely that this mechanism is the reason of a greater number of ALDs in convergent areas. I suggest that there are two possible mechanisms that could explain why convergent topography could enhance the propensity of ALD initiation. Firstly, melting of permafrost along a hillslope drives an enhanced throughflow that increases pore pressures in convergent topography, or secondly, increasing ground ice concentration in areas of convergence over time and when melted rapidly

by an extreme weather event generates excess pore pressures that drives failure. The key difference between these mechanisms is whether thawing permafrost across a hillslope and the movement of water towards the landslide initiation site generates the excess pore pressures, or whether the excess pore pressures are generated in-situ by melting ice that has accumulated progressively over a number of years.

Field evidence suggests that convergent topography is important for ALD initiation, but as ALD initiations are rare, the exact triggering conditions are poorly understood. For example, Balser et al. (2015) found that ALDs near Feniak Lake would initiate in water tracks, curvilinear stripes of saturated soil, usually 1 m thick, confined to shallow depths by the impermeable permafrost (McNamara et al. 1999; Trochim et al. 2016a).

Relatively recent studies have shown that other mechanisms of slope erosion, such as gullying, develops in water tracks from thermal erosion (Bowden et al. 2008; Gooseff et al. 2009). Ground ice contents of water tracks are extremely high with measured ice contents, from 50 to 90% (Ping et al. 2008; Trochim et al. 2016a). The field evidence lends support to the second hypothesis that high ground ice contents in areas of convergent topography drive ALD initiation.

Further support of the second hypothesis comes from the repeated mapping of ALD through many seasons. In Feniak Lake, ALD mapping occurred after the exceptional warm summer in 2004. Another warm summer occurred there in 2007 where the thaw front reached the same depth, yet no new ALDs were observed (Swanson 2012). This suggests that ice needs time to reform and/or the annual shearing by solifluction has not had long enough to reduce the shear strengths characteristics of the new active layer/permafrost boundary (Lewkowicz 1990; Harris and Lewkowicz 2000; Leibman et al. 2003).

I have demonstrated that drainage networks are important locations for ALD initiation sites. However, other factors such as aspect are also important. Research found that the distribution of ALDs were skewed towards north-facing slopes because

of less solar radiation (Swanson 2014; Niu et al. 2015; Rudy et al. 2017). This is attributed to uneven melting patterns causing less snow to thaw on north-facing slopes, insulating the permafrost below for longer from cold temperatures, allowing a deeper advance of a thaw front in the summer. On the other hand, north-facing slopes have been found to accumulate more transient layer ice (Shur et al. 2005). Despite this, our data show that the correlation of ALD with the drainage network greatly outweighs any aspect control.

4.5.3 The spatial distribution of ALD slope stability

I sought to understand whether it was possible to produce a spatially distributed model of slope stability that is appropriate for ALD initiation. I developed an infinite slope-based spatial model, in which I primarily varied the cohesion (and hence the depth of failure). The model assumes a buffer of 20 m and a minimum drainage threshold of 25000 m^2 and increases pore pressures within the channel network relative to the adjacent hillslopes.

I tested three scenarios (Table 4.1): Scenario 1, cohesion is 0 kPa (Harris and Lewkowicz 2000) representing residual conditions (Figure 4.6); scenario 2, cohesion is 2 kPa (Harris and Lewkowicz 2000) representing near peak conditions (Figure 4.7); and scenario 3, cohesion is 4.8 kPa (Harris et al. 2008b) for peak conditions (Figure 4.8). I kept the internal angle of friction at 19° (Harris and Lewkowicz 2000) for all scenarios. For each scenario, I produced a sensitivity analysis by varying the excess pore pressure generated in the channel network and the thaw depth (representing the potential depth of the flow). I generated a range of excess (elevated) pore pressure based on experimental values (Harris et al. 2008b), because there is no field data for the pore pressures generated by melting ice lenses. Field evidence does suggest that excess pore pressures are important for initiating ALD (Harris and Lewkowicz 2000). They suggest that high excess pore pressure would be required to generate slides on

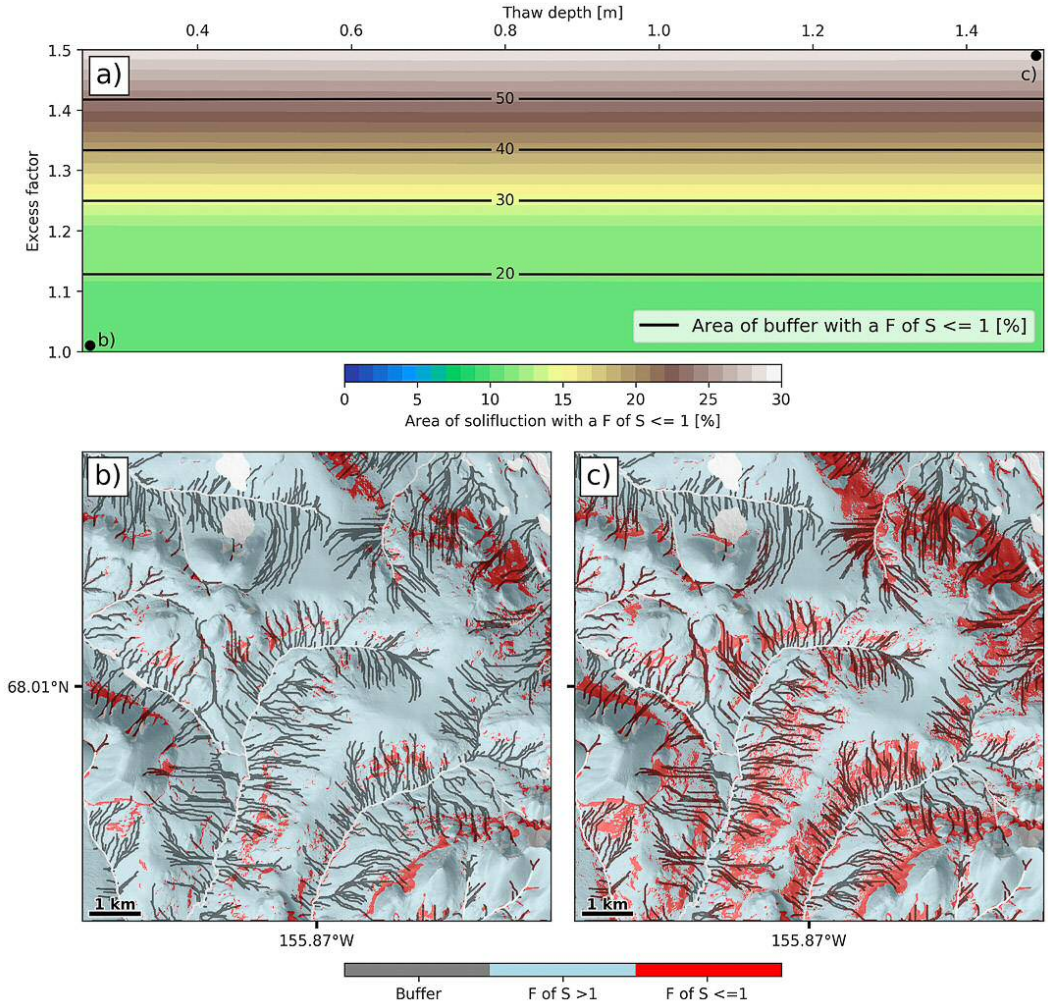

Figure 4.6 Scenario 1. a) Contour plot showing the percentage area of solifluction with a factor of safety (F of S) <=1, the threshold for failure (in colour). Black lines represent the percentage area of the buffer with an F of S <=1. b) Map showing the areas of failure (allochthonous, solifluction, and buffer) with an excess factor of 1 and a thaw depth of 0.25 m. c) Map showing areas of failure with an excess factor of 1.5 and a thaw depth of 1.5 m. Both b) and c) are underlain with a hillshade.

shallow slopes that maintain high internal angles of friction, which is typically 31° in silty-clay soils (Harris et al. 2008b; Nater et al. 2008). A study of ALD in the Brooks Range found ALD to initiate on slopes of between 6° to 24° (Swanson 2014). Even though excess pore pressures are associated with the gelifluction component of solifluction (Harris et al. 2011) these pressures need to be sufficiently high enough over a continuous area to reduce the basal shear strength of the active layer to initiate failure (Lewkowicz and Harris 2005b).

In all the scenarios, the spatial distribution of factors of safety below one does not correlate particularly well with the distribution of ALD. Consistent with predictions of the infinite slope model, scenario 1 (Figure 4.6) demonstrates that with no cohesion there is no depth dependence on slope stability. Spatially, there is a tendency for producing low stability values in the mid slopes, with very little dependence on the location of the channel network (Figure 4.6). In scenario 2 (Figure 4.7) with greater shear strengths significantly less of the landscape will fail for example at 1.5 excess

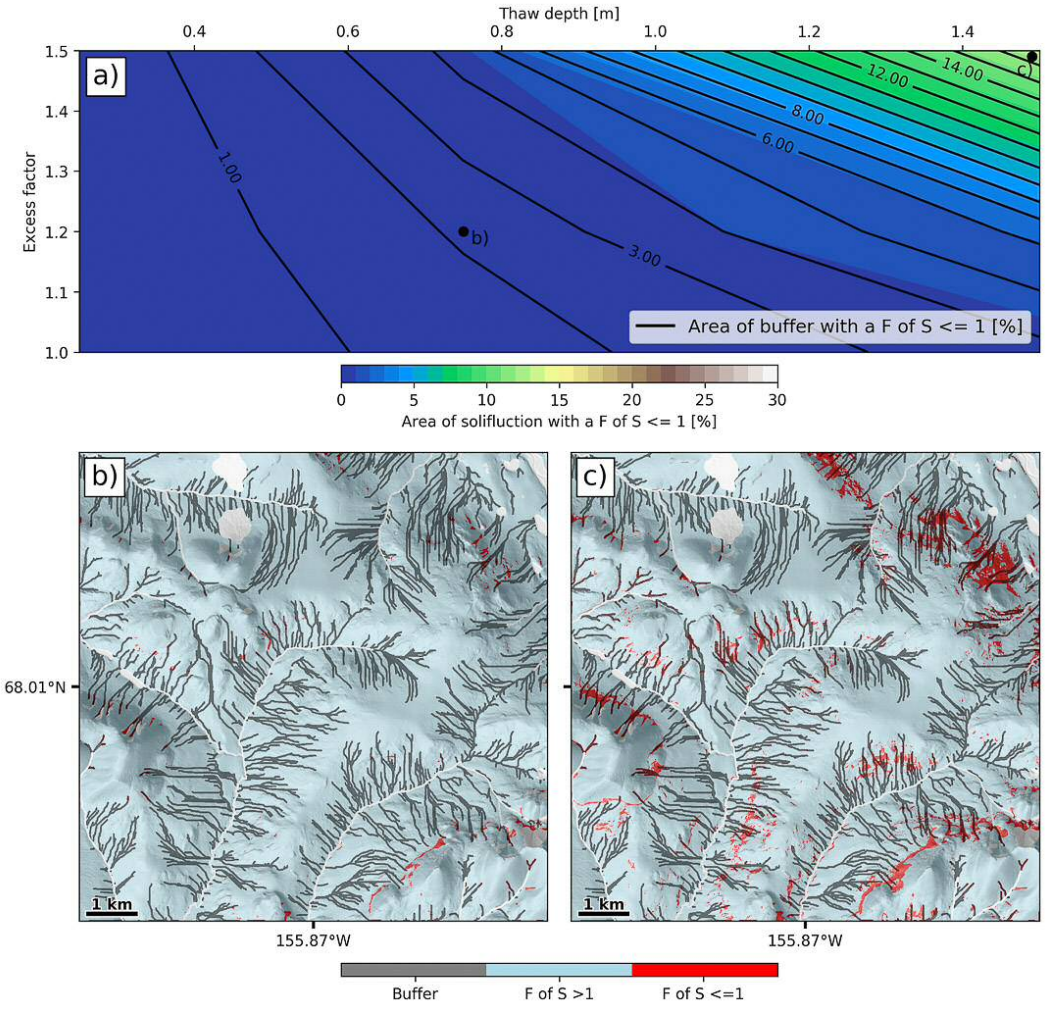

Figure 4.7 Scenario 2. a) Contour plot showing the percentage area of solifluction with a factor of safety (F of S) <=1, the threshold for failure (in colour). Black lines represent the percentage area of the buffer with an F of S <=1. b) Map showing the areas of failure (allochthonous, solifluction, and buffer) with an excess factor of 1.2 and a thaw depth of 0.75 m. c) Map showing areas of failure with an excess factor of 1.5 and a thaw depth of 1.5 m. Both b) and c) are underlain with a hillshade.

factor and 1.5 m depth only 16% of the buffer will fail. Adding shear strength to the soil of both solifluction and buffer produces a non-linear relationship between the excess factor and thaw depth. Spatially, this model does the best job of producing low slope stability values within the channel network (buffer). The reason for this is that the non-linear relationship between stability and depth exacerbates the effects of the excess pore pressures that are generated within the channel network (buffer). The final scenario (Figure 4.8) likely represents too much cohesion for this landscape. There is a similar spatial pattern to scenario 2, but less of the landscape failing. Importantly, you cannot generate failure depths of less than 0.75 m, regardless of the excess factor (Figure 4.7).

Our spatial modelling demonstrates that Arctic soils are likely to have a relatively small amount of cohesion. Cohesionless soils produce spatial patterns of ALD that are inconsistent with the distribution of mapped ALD. The importance of soil cohesion in initiating ALD has been discussed in the literature. Harris and Lewkowicz (2000) suggested that residual condition is caused by annual plug like solifluction that re-orientate clay particles and soil grains within the zone of annual shearing.

If this is true then there must be an element of pre-conditioning of the soil by annual solifluction before any failure can occur. Cohesion controls the failure depth, with solifluction depths of up to 1.06 m on Svalbard (Matsuoka 2001a; Harris et al. 2011). According to Balser et al. (2015) the depth of the active layer of an ALD failure in Fauna Creek, Noatak Basin was 1.1 m, similar to the maximum solifluction depths on Svalbard (Matsuoka 2001a; Harris et al. 2011) but deeper than the depth on Ellesmere Island of c.a. 0.75 m (Harris and Lewkowicz 2000). These relatively shallow initiation depths suggest that cohesion is low. For this particular example, I have modelled beyond 1.1 m, these scenarios may represent future scenarios in warmer climate (Akerman 2005). There are a number of interesting questions in this respect, including is there a depth limit to ALDs? and do the mechanisms of failure

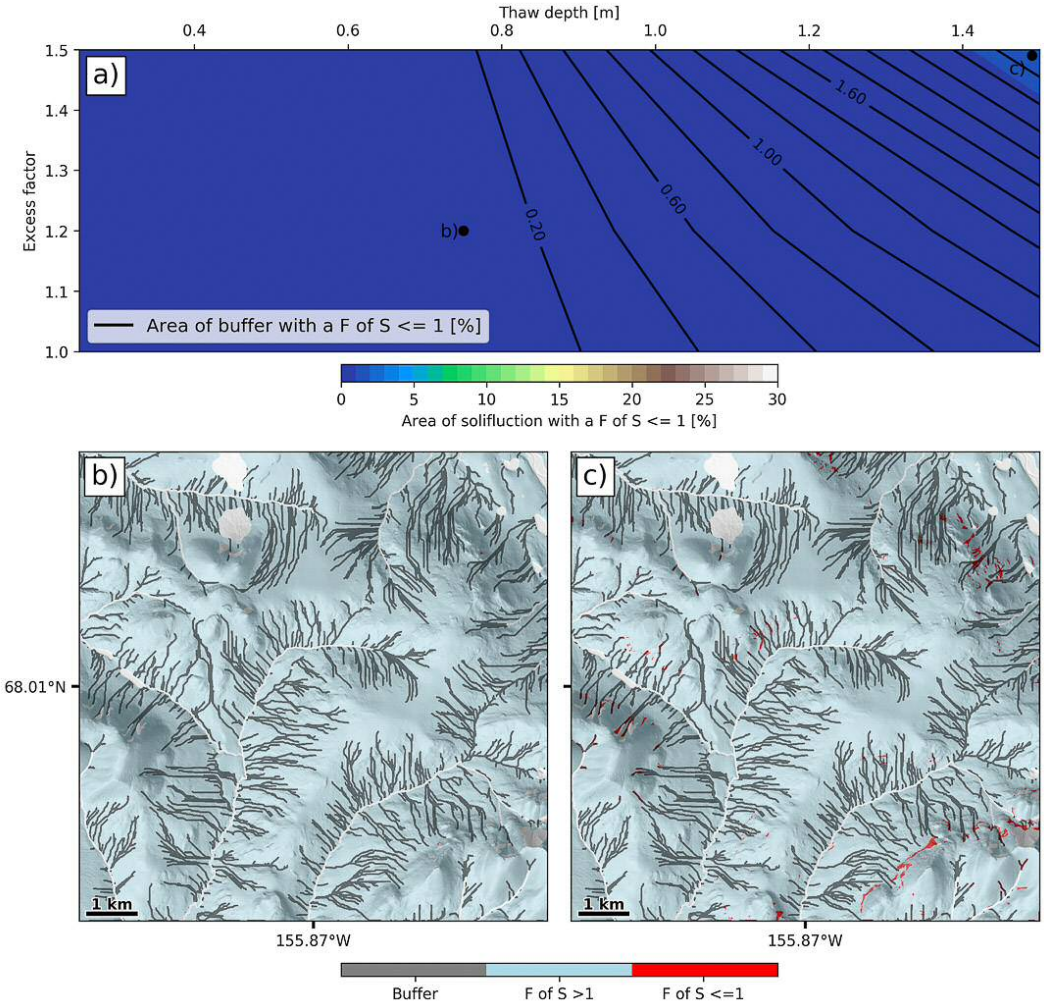

Figure 4.8 Scenario 3. a) Contour plot showing the percentage area of solifluction with a factor of safety (F of S) <=1, the threshold for failure (in colour). Black lines represent the percentage area of the buffer with an F of S <=1. b) Map showing the areas of failure (allochthonous, solifluction, and buffer) with an excess factor of 1.2 and a thaw depth of 0.75 m. c) Map showing areas of failure with an excess factor of 1.5 and a thaw depth of 1.5 m. Both b) and c) are underlain with a hillshade.

change at a particular depth? To consider how realistic the three scenarios are I can look at the area of mapped ALD relative to the area of buffer and solifluction (Table 4.2). If the mapped ALDs have an area of 1 km^2 then this is equivalent to c.a. 5% of the area of the buffer and c.a. 2% of solifluction. I find that scenario 1 is unrealistic because too much of the landscape fails. Both the ALD percentage area of buffer and solifluction can't be plotted on the contours of (Figure 4.6).

Table 4.2 Geometry of landforms

Landform	Area [km^2]
Allochthonous	26.05
ALD	1
Buffer	18.8
Solifluction	51.27
No data	3.88

In scenario 3 the opposite is true and too little of the landscape fails relative to the percentage area of ALDs (Figure 4.6). What is more realistic is scenario 2 (Figure 4.7). If I assume that in 2004 the maximum depth of thaw was 1.1 m, to account for the 5% of the buffer failing would require an excess factor of 1.5 times that of the hydrostatic which is equivalent to 16.17 kPa. Similarly, for solifluction, the excess factor would need to be higher than 1.5 or the shear strength parameters would need to be lower. So how realistic is 16.17 kPa? Using measurement taken by Harris et al. (2011) for a soliflucting slope in Endalen, Svalbard I can calculate that the excess factor at the time of thaw and which coincide with solifluction movement was c.a. 1.2, if excess pore pressures needed to be 14% higher to cause ALD failure (Harris et al. 2011) i.e. 15.09 kPa. However, even at shallower depths and lower excess factors, the model shows that failures can still occur, but there will be fewer.

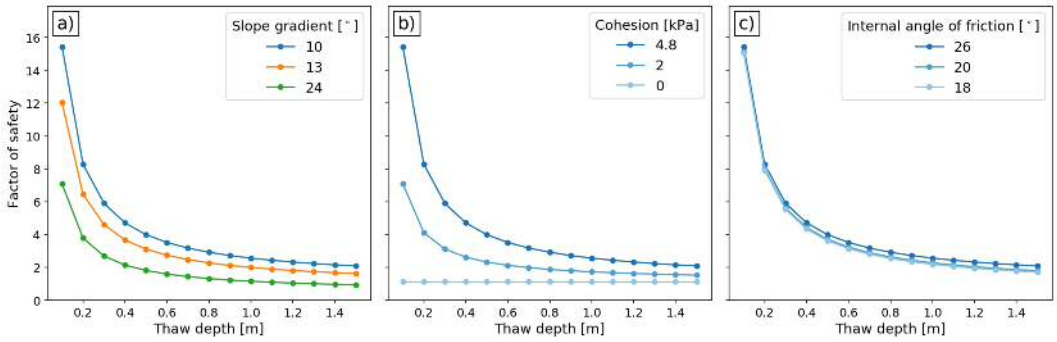

Figure 4.9 Factor of safety plots derived from an infinite slope analysis. a) Testing the impact of slope gradient where c' = 4.8, ϕ= 26°. b) Testing the impact of cohesion (c') where ϕ = 26°, β = 10°, and m = 1.18. c) Testing the impact of the internal angle of friction (ϕ) on the factor of safety where c' = 4.8 kPa, β = 10°, and m = 1.18. The blue line and its colour gradation represent the use of a slope gradient of 10°.

If thaw fronts are expected to advance deeper into the already warming permafrost than our model suggests it will require less excess pore pressures i.e. fewer ice lenses to initiate failure. For example, let's assume that a thaw front advances to 1.5 m. Therefore, scenario 2 is the most realistic scenario for the pore pressures which caused failure during the unusually warm summer of 2004. To cause 5% of the buffer to fail would only require an excess factor of 1.4 compared to 1.5 at 1.1 m depth (Figure 4.7). I base the success of my model on whether the activation zone coincides with modelled ALDs. However, scenario 1 (Figure 4.6) could offer the best correspondence because it depicts zones of potential failure, but not all such areas experience ALDs. This is not an anomaly, because other factors need to be taken into account by the model such as aspect (Rudy et al. 2017), soil frost susceptibility (Harris et al. 2008c), and thaw history (Lewkowicz and Harris 2005a). Slope aspect, for example, can influence the likelihood of ALD failure because thaw is likely to be greater on west, south, and east-facing slope than north-facing slopes. Further analysis of the impact of varying resisting forces such as the internal angle of friction and cohesion demonstrated that cohesion controls the depth of failure (Figure 4.9).

In this chapter, I have demonstrated that ALDs are associated with watercourses (topographic convexities) which may be attributable to denser concentrations of ice lenses in such locations. However, an alternative explanation is that some ALDs occur along the banks of first-order streams where slope gradient is steeper. Google Earth imagery shows that the failure zone of some ALDs in Nukatpiat extend to the banks of first-order streams which is evidence for failure caused by steeper banks and/or thermo-erosion from flowing water. It is known that ALDs initiate because of thermo-erosion or bank instability caused by fluvial undercutting (Harris and Lewkowicz 1993). However, the evidence in this chapter doesn't support this. Firstly, there are some ALDs that are not connected to first-order streams and have therefore initiated in the absence of thermos-erosion or bank instability. Secondly, ALDs caused by bank instability are thought to be pre-cursors to retrogressive thaw slumps

(Balser et al. 2015). However, no retrogressive thaw slumps are present in Nukatpiat. Third, the headscarp of ALDs connected to first-order streams is located over 500 m from the corresponding stream and the material from the track zone either dams the stream or is partially removed. Finally, many of the track zones of ALDs are interconnected and correspond to the DEM-derived stream network.

This analysis has demonstrated that to a first order, a simple, rules-based spatial model can have predictive power in understanding the distribution of ALD across Arctic landscapes. It would be interesting in the future to understand whether the critical drainage threshold for ALD initiation is consistent for other geographical areas. If so, this method could be used to develop hazard models for Arctic landscapes that are prone to ALD initiation.

4.6 Conclusion

The landscape classification model performs well in high relief environments but must be modified for low relief topography. Despite not being able to separate ALDs from landforms, I have observed that ALDs are coincident in areas of solifluction. Within areas of solifluction, regions of convergence are where I find ALDs. These areas of convergence allow for a supply of water ice for lenses to grow. As not all areas of convergence show ALD activity there must be a more fundamental aspect I do not yet understand about ALD dynamics; this I will explore in the next chapter.

Chapter 5

Modelling the impact of permafrost ice distribution on hillslope stability

5.1 Summary

Shallow permafrost landslides called ALDs threaten infrastructure and are an important mechanism for delivering sediment, carbon, and other nutrients to Arctic streams. Little is currently known about the ground ice conditions needed to generate ALDs on soliflucting hillslopes. I modified a two-dimensional slope stability model to assess the temporal and spatial impact of excess pore pressures generated by thawing ice lenses on ALD initiation. More ice distributed along the failure plane decreased stability, but this varied depending on the position of ice lenses. The two-dimensional distribution of ice lenses and the thaw rate had only a minor effect on slope stability. Our results demonstrate that ALDs are most likely to initiate a failure plane in areas of high ground ice concentration. Therefore, I suggest that future ALD potential may be better understood through field measurements of ground ice distribution on Arctic hillslopes.

5.2 Introduction

The potential for hazardous landslides is a consequence of future rapid warming of the Arctic (Lewkowicz and Harris 2005a). Higher latitudes are warming at double the global average rate, resulting in more frequent extreme summer temperatures that drive heat deeper into permafrost soils and snowfall that insulates the soil from freezing (Stocker 2014). Higher heat fluxes increase the depth of the active layer resulting in more vigorous hillslope surface processes such as ALDs (Lewkowicz and Harris 2005a), rockfall (Gruber et al. 2004), and solifluction (Harris et al. 2011). More active hillslope surface processes will also increase fluxes of sediment (Lamoureux et al. 2014) and nutrients (Lamoureux and Lafreniere 2014) into Arctic streams. Hillslope process rates are strongly governed by the interaction between extreme temperatures and ground ice distributions in permafrost soils (Harris et al. 2011). A better understanding of the mechanics of this interaction can lead to the generation of more robust models of Arctic hillslope processes.

This chapter focuses on understanding the conditions that generate shallow translational landslides called ALDs (Gooseff et al. 2009; Harris and Lewkowicz 2000; Lafreniere and Lamoureux 2013; Leibman et al. 2003; Lipovsky et al. 2006). ALDs are thought to initiate by reducing shear strength in an ice-rich zone at the base of the active layer (Harris and Lewkowicz 1993; Mackay 1981). Excess pore pressure that generates downslope movement occurs during the collapse of pore space associated with the melting of ice lenses, a process known as thaw consolidation (McRoberts and Morgenstern 1974). However, high pore pressures alone cannot generate ALDs. If ground ice is sporadic or ice lenses are at shallow depths, the loss of shear strength during thaw may not be enough to exceed earth pressure or apparent cohesion and allow the establishment of a continuous slip plane. In that case, there may be more creep-like failure or solifluction (Harris et al. 2008c). Apparent cohesion in Arctic soils is governed by the distribution of clays, the penetration of the

roots of Arctic vegetation, and clay alignment associated with previous downslope movements (Harris et al. 2008c). Hence for a given soil, the difference between whether a slope will progressively develop downslope shear strains (solifluction) or fail catastrophically (ALDs), appears to be governed by the spatial distribution of excess pore pressures generated on the slope.

In permafrost regions, the distribution of ground ice varies through time as a function of soil moisture and temperature conditions. In regions of permafrost, ground ice distribution is governed by two-sided freezing (Mackay 1981), where downward and upward freezing causes liquid water to migrate towards the surface and base of the active layer, leaving a central desiccated zone. However, the history of temperature conditions at a site is also important in governing ground ice distributions, as relatively cool summers may see a net increase in the total ice volume in a soil, while particularly warm summers may see a net loss in ice lenses. Lewkowicz (1990) suggested that it is an approximately decadal cycle of ice lens accumulation and melting that drives ALDs. Shallow groundwater conditions, such as those governed by topographic convergence (e.g. water tracks) may also increase the total volume of ground ice in a soil (Balser et al. 2009; Lamoureux and Lafreniere 2009).

A wide range of climatic conditions has been suggested to cause ALDs. They are all characterized by mechanisms that drive heat beyond the average active layer depth and into the ice-rich transitional zone. The most common mechanisms include early thaw, thick winter snow depths, extremely high summer temperatures that persist for days to weeks, and high rainfall (Balser et al. 2015; Lamoureux and Lafreniere 2009; Lewkowicz and Harris 2005a). Non-climatic mechanisms for ALD initiation include forest fires, lateral river erosion and engineering processes (Harris and Lewkowicz 2000; Jolivel and Allard 2013; Niu et al. 2015; Wang et al. 2014). Apart from mechanisms related to physical undercutting at the toe of a slope, all ALD initiations depend on heat transfer within the active layer. While geotechnical conditions are also important, the coincidence of solifluction and ALDs on the same

hillslopes and in the same soil types points to thawing ground ice playing a key role. Hence, I examine how differences in the distribution of ground ice may affect ALD initiation.

5.3 Material and Methods

I sought to understand the conditions that promote ALD failure for differing ground ice volumes, distributions of ice with depth, and rates of thaw penetration. To do this I used a two-dimensional plane strain slope model of a thawing slope based on well-constrained laboratory tests of ALD initiation (Harris et al. 2008c) (Figure 5.1). I modelled a laboratory slope to avoid uncertainties in the material parameters and failure dimensions for a natural slope. The modelled thawing slope is 15 m × 7 m with a gradient of 24° and a maximum active layer thickness of 1.5 m (normal to the surface), below which is permafrost (Harris et al. 2008c). I used a geotechnical software, GeoStudio (Krahn 2004), to model the impact of temporal and spatial distribution of excess pore pressures during thaw on the factor of safety against failure using the limit equilibrium based Morgenstern-Price method of slices (Morgenstern and Price 1965). For each test, I defined the permafrost layer as an impermeable rigid material. Thawed soil had a unit weight of 19.62 kN m^{-3}, cohesion of 3.5 kPa and an internal angle of friction of 31° (Harris et al. 2008c). Pore pressure values measured for thawing ice lens in (Harris et al. 2008c) experiments were on average 20% greater than the hydrostatic pore pressure value, a value that I chose for all but one test. I sought to understand the conditions that promote slope failure by considering how differing ground ice conditions affected the factor of safety of our slope in three tests: (1) a test where I varied the volume of ground ice along the permafrost-active layer boundary, (2) a test using differing distributions of ground ice with depth in the active layer, and (3) a test where I allowed pore pressures to dissipate, simulating different rates of thaw front propagation. First, I tested the impact of varying ice

lens density by calculating the factor of safety for a thaw front depth of 1.5 m. Here I assume that thawing along the slide plane generates excess pore water pressures (an assumption I relax for later tests) for between 0% and 100% of the slide plane. To understand the impact of our assumption of a 20% excess pore pressure, I also randomly varied excess pore pressures in the ice lens cells between 0 and 20% of the hydrostatic value. For our second test, I sought to understand the role of realistic

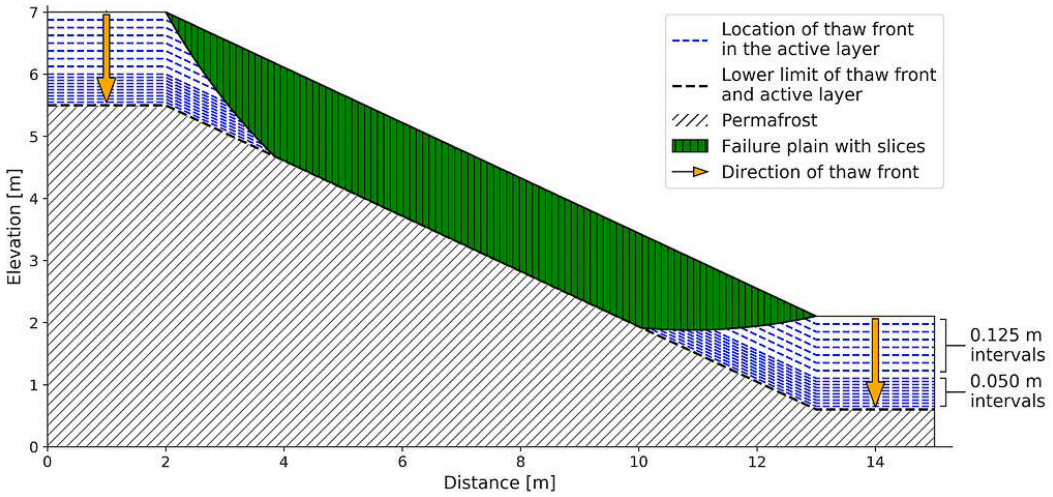

Figure 5.1 A conceptual model showing the thawing intervals (blue dashed lines) where the factor of safety was calculated and subsequent failure plane generated. The green striped area represents the failure plane at 1.5 m depth along with slices used in the Morgenstern-Price method to calculate the factor of safety. The slope gradient is 24° with an active layer thickness of 1.5 m.

depth distributions of ground ice to failure within the model. The three common distributions of ground ice that I tested were uniform, linear, and power law (Figure 5.2). Excess ice volumes of greater than 60% of the soil mass are rare in the field (Allard et al. 1996; Harris et al. 2011; Kokelj and Burn 2003; Morse et al. 2009), so I chose this as a maximum value for all tests. For each test, I assumed undrained conditions i.e. pore pressures did not dissipate (again I relax this condition later), and calculated slope stability when the thaw front was at various depths in the soil column. Between 0 and 1 m, thaw depths were considered at intervals of 0.125 m and below 1 m at intervals of 0.05 m (Figure 5.1). For each analysis, the thaw front depth defined an interface between an upper layer of thawed soil and a lower layer of

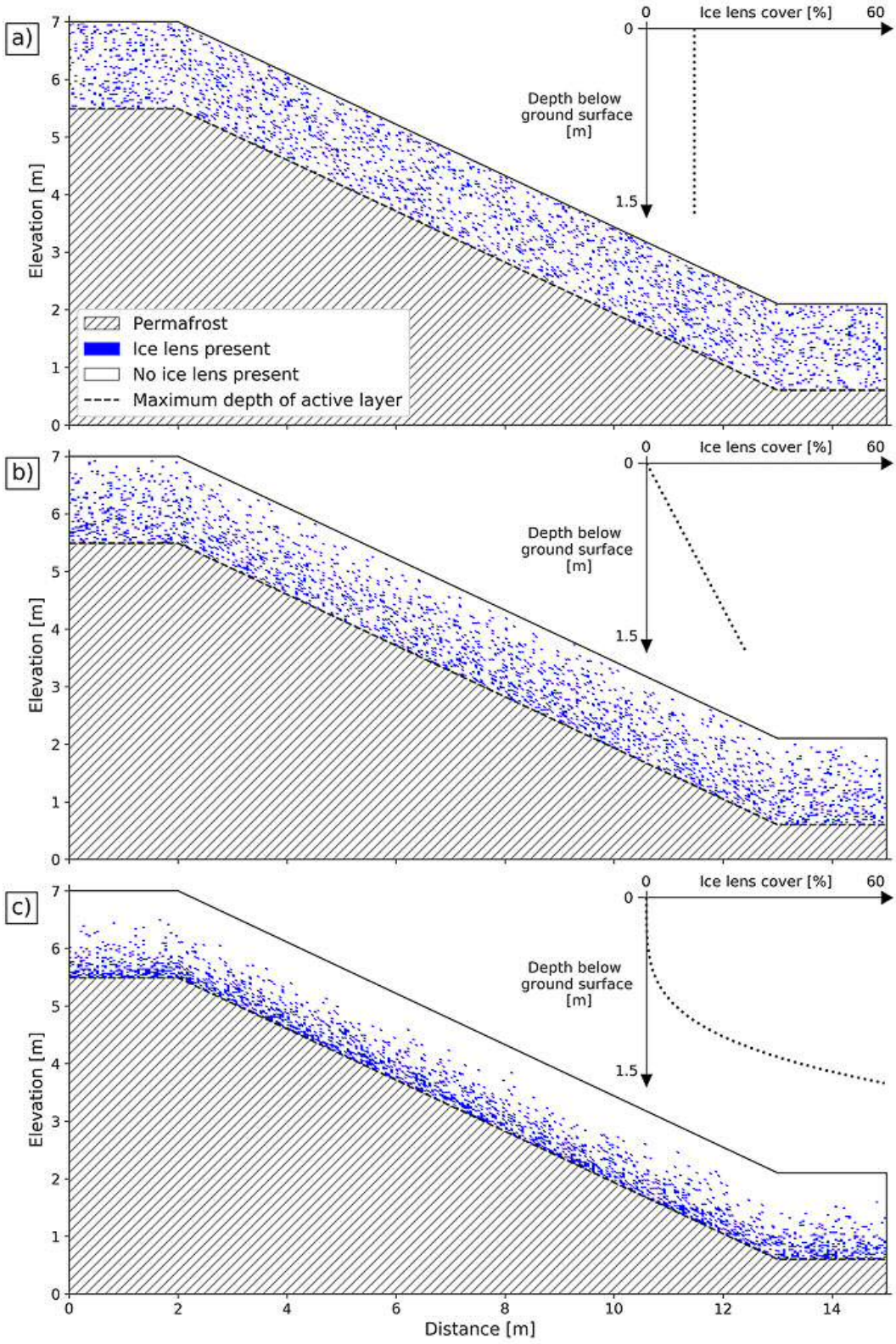

Figure 5.2 The distribution of 2230 ice lenses in our modelled hillslope for different scenarios. a) Uniform distribution, b) linear distribution, and c) power law distribution.

permafrost. I randomized, at any particular depth, the location of cells that represent ice lenses termed hereafter as ice lens cells. For our uniform distribution, I randomly assigned 60% of the cells as ice lens cells (Figure 5.2). For our linear distribution, I increased linearly with depth the number of cells assigned as representing ice lenses from 0% at the surface to 60% at a depth of 1.5 m (Figure 5.2). I fitted a power law distribution function of the form:

$$EI = 11.841z^{3.9947} \tag{5.1}$$

to field data from Kokelj and Burn (2003), (Figure 5.2), where z is depth (metres) and EI is the excess ice by the soil mass (%) and is used to define the percentage of cells assigned as representing ice lenses, (from 0% at the surface to 60% at 1.5 m). Again I randomized the location of the ice lens cells at each depth. For each of these scenarios, two cases are considered: the first with a fixed number, 2230, of ice lenses in the active layer; and the second with a varying number of ice lenses for each distribution to produce 60% of cells containing ice lenses at a depth of 1.5 m.

Finally, I tested the effect of thawing and excess pore pressure dissipation rates on the factor of safety through consideration of three separate scenarios designed to represent no, moderate, and fast dissipation rates. In scenario 1, I assumed that the thaw front advanced rapidly so that the pore pressures of 1.2 times that of hydrostatic assigned to the ice lens cells did not dissipate at all. For scenario 2, the thaw front was assumed to progress at a moderate pace, so that the region of thawed soil where excess pore pressures have not dissipated, termed hereafter as the excess pore pressure layer, was limited to those ice lens cells within 0.125 m of the thaw front. While in scenario 3, the thickness of the excess pore pressure layer was decreased to 0.025 m to represent slow thaw front propagation. To contextualize the thickness of the excess pore pressure layer data from Harris et al. (2008), figure 19b p.452, the line labelled ‘1.3 m (lower)’ can be considered. From this, I calculated the average

dissipation time of 43.97 hrs for excess pore pressures and combined this with the reported average thaw rate of 1.48 mm hr^{-1} to predict that their experiment had an excess pore pressure layer thickness of 0.06 m. I represented the dissipation of pore pressure by returning pore pressures to hydrostatic values once outside of the excess pore pressure layer.

5.4 Results and Discussion

Our analysis shows that as the proportion of ice lenses increases along the failure plane the factor of safety decreases linearly (Figure 5.3). For slopes with a constant excess pore pressure of 17.6 kPa, the minimum factor of safety was 1.005, while variable excess pore pressures yielded a higher minimum factor of safety of 1.065. To understand how the factor of safety might vary with different distributions of lens width, I randomly varied ice lens cell location, and thereby the resulting distribution of ice lens width (which is a function of the occurrence of collocated ice lens cells) within five tests (shaded areas in figure 5.3). Random distributions of ice lens width affect factor of safety most when the proportions of ice lenses along the failure plane are between 20% and 80%. At low and high proportions the variability in ice lens size is small, as all ice lenses are either very small (single pixels) or very large. For intermediate proportions of ice lenses, lower factors of safety are associated with more frequent wide ice lenses. This suggests that having wide lenses with larger gaps between them produces lower factors of safety than evenly spaced, but narrow ice lenses. These results highlight the importance of both the width of ice lenses and of the values of excess pore pressures generated by the consolidation of ice lenses. It is only when there is a large network of wide ice lenses that are consistently generating high excess pore pressures that I generate factors of safety close to the stability limit. This implies that slow and prolonged freezing of this zone (which is liable to produce thicker, more continuous lenses) may precondition

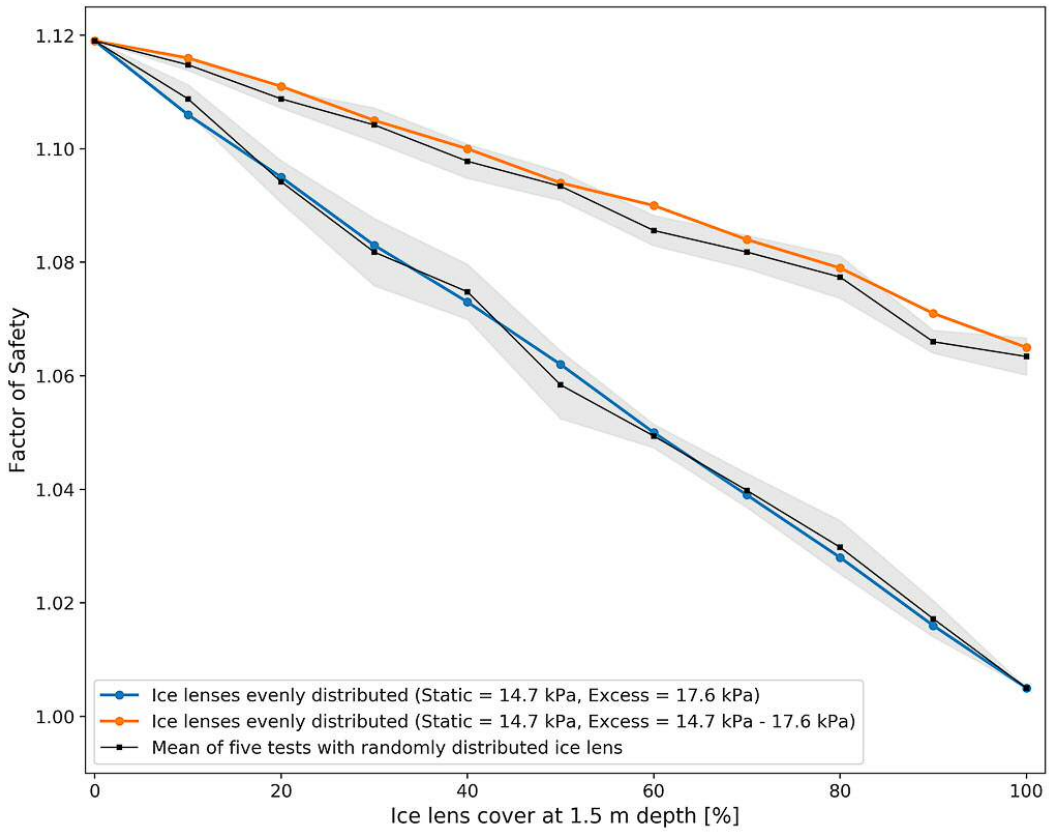

Figure 5.3 The impact of varying ice lens cover along a failure plane at 1.5 m depth. The blue line represents a controlled distribution of ice lenses. The black line represents a mean of five tests with ice lenses randomly distributed. The grey shaded area is the standard deviation of the five tests. Cohesion is set at 3.5 kPa.

ALD sites to failure by increasing ice content and thus raising pore-water pressure well above the hydrostatic. Of the three variables tested in this experiment (width, ice lens size distribution, magnitude of excess pore pressure), the modelled slope is most sensitive to the magnitude of excess pore pressure generated by each lens. For example, with an average excess pore pressure value of 16.1 kPa, our random scenario generates a factor of safety of 1.063, compared with a factor of safety of 1.005 for an excess pore pressure of 17.6 kPa. In comparison, differences in the proportion of ice lenses along the failure plane from 0 to 100% represent a difference of 0.056 in the factor of safety, while the difference in the distribution of ice lens width represents an average difference of 0.002 in the factor of safety. These results suggest the threshold for ALD failure (rather than solifluction) is extremely sensitive

to the amount of ice along the failure plane and the excess pore pressures that it generates. This observation is consistent with experimental evidence of Harris et al. (2008). They found that when using a simple silty soil, ice lenses were generated along a single layer, resulting in consistent ALD failures. To create solifluction, Harris et al. (2008) modified the material (by adding kaolinite) to allow ice lens generation throughout the soil column. Field evidence suggests that high excess pore pressures are common on solifluction slopes (Harris et al. 2011), yet the slopes where these high excess pore pressure were measured did not fail catastrophically. The modelling evidence presented here suggests that the difference between high excess pore pressures generating solifluction or ALD may be primarily due to the connectivity of ice lenses.

The absolute depth of a failure, and therefore the influence of ground ice will depend on the cohesive properties of the soil. The non-linear shape of the curve of the factor of safety against thaw depth (Figure 5.4) demonstrates the importance of the cohesion value in governing the depth of the failure. In our modelling effort, I fix cohesion at 3.5 kPa to keep it consistent with the experiments of Harris et al. (2008). However, in natural settings ALDs can initiate at shallower depths (Lewkowicz and Harris 2005b), suggesting that apparent cohesion may be lower than 3.5 kPa in the field. In the field, cohesion may also vary with time as annual plug-like solifluction re-orientates soil grains and clay flakes (Harris and Lewkowicz 2000). Also, the role of vegetation, which is often shallowly rooted in providing cohesion to Arctic soils is uncertain, but likely to be small (Lewkowicz and Harris 2005a). Instead, soil structure, particularly clay content may represent a significant source of cohesion and suggest a role for geology in governing the distribution of ALD initiation (Harris and Lewkowicz 1993). The results indicate that the depth distribution of ice lenses has a significant role in defining the stability of high latitude hillslopes. First, I kept the number of ice lenses constant and varied their distribution within the soil column (Figure 5.2). When I distribute ice lenses uniformly or linearly with depth in the

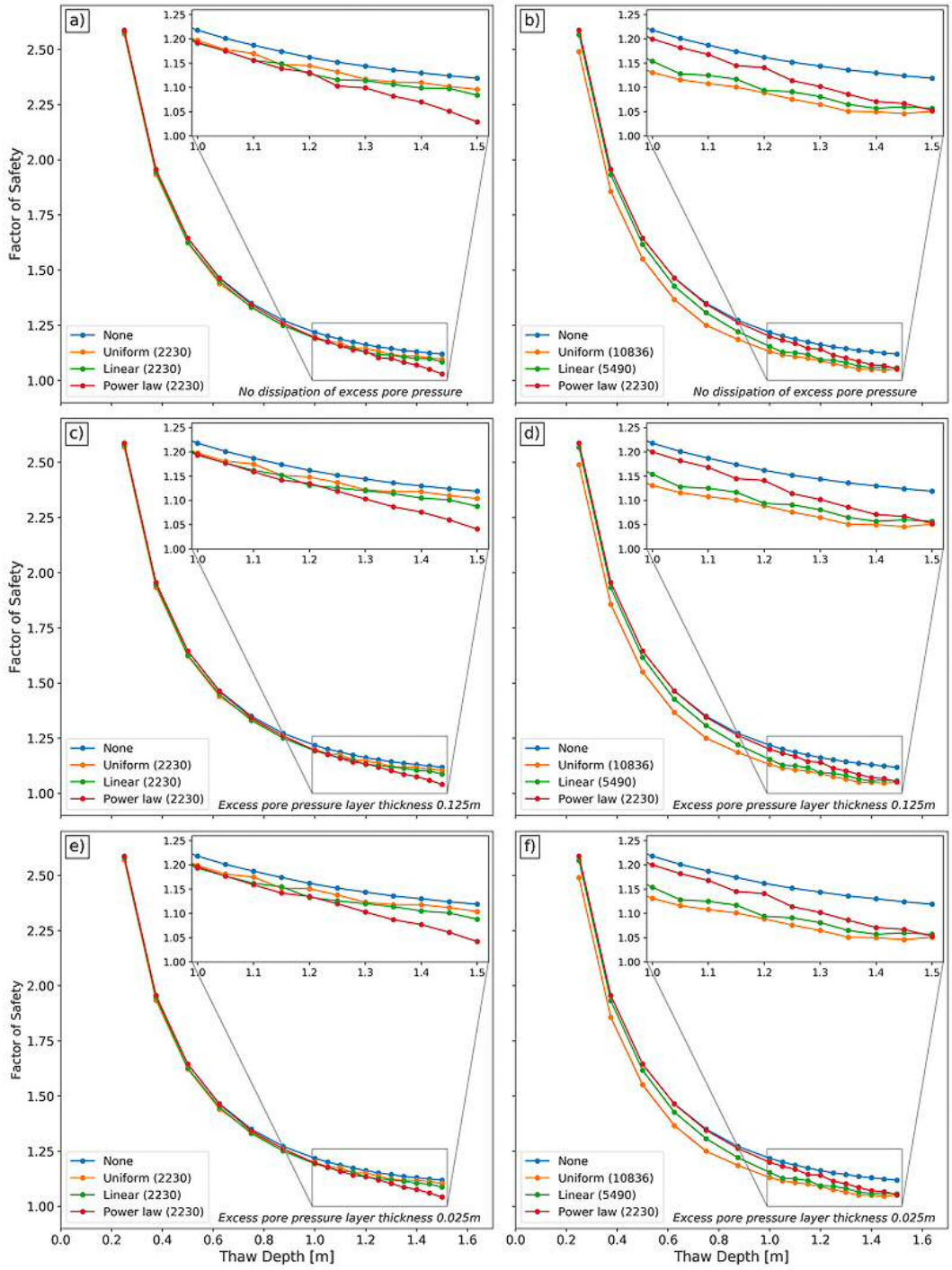

Figure 5.4 Model results showing thaw depth against the factor of safety. (a, c, and e) are model runs that restrict the number of ice lenses in the active layer to 2230. (b, d, and f) are model runs with varying number of ice lenses for each distribution. (a, b) are model runs where there is no dissipation of pore pressure (scenario 1). (c, d) are model runs where the region of thaw is 0.125 m thick (scenario 2). (e, f) are model runs where the region of thaw is 0.025 m thick (scenario 3).

soil column, soils are considerably more stable than when ice lenses are distributed non-linearly (Figure 5.4a, c, e). The proportion of the failure plane covered by ice lenses at a depth of 1.5 m is considerably less for the uniform (12%) or linear models (25%), resulting in a lot of narrow ice lenses distributed across the failure plane. Whereas the power law model has a greater proportion of ice lenses (60%) where the failure plane is likely to propagate. For the next experiment, I varied the number of ice lenses in the soil column such that each different distribution had a maximum of 60% ice lenses at any depth (Figure 5.4b, d, f). Here, all distributions were considerably more unstable than the no ice lens scenario and converged to a single factor of safety at 1.5 m. What these experiments show is that it is not the total volume of ice lenses in a soil that governs stability, instead, it is the proportion of ice lenses found along likely failure planes. The distribution of ground ice on hillslope soils is very poorly constrained, as are the spatial controls on the variability in ground ice. However, a number of authors have noted the propensity for ALDs to initiate in areas of topographic convergence (Balser et al. 2009). Areas of convergent topography accumulate water, making them good candidate sites for high ground ice concentrations at depth.

Finally, I examined the role of thaw propagation rates on slope stability. I did this, by assuming that slow-moving thaw fronts will have a narrow excess pore pressure layer. When I compare the results of our slow-moving thaw front experiments (Figure 5.4c and d) to those with no pore pressure dissipation there is no difference in the factors of safety. This suggests that pore pressures generated at the thaw front govern the generation of a failure plane. Field evidence suggests that extreme weather events cause ALD initiation, leading to a number of authors suggesting that it is the rate of thaw penetration that causes ALDs (Lewkowicz and Harris 2005b; McRoberts and Morgenstern 1974). For example, Lewkowicz and Harris (2005b) measured rates of thaw propagation of >10 mm day^{-1} for two weeks before ALD initiation. Our modelling evidence suggests that in this scenario the high rates of

thaw propagation themselves did not initiate an ALD as the distribution of high pore pressures within the soil column does not play a significant role in ALD initiation. Instead, the high rates of thaw propagation caused the thaw front to penetrate to deeper than average depths, where ice lenses could melt and generate a failure plane. Interestingly, in this example, fewer ALDs initiated in an extreme weather event the following summer, possibly because ice lens concentrations had changed after melting during the previous summer (Harris and Lewkowicz 2000).

Our modelling effort constrains the role of ground ice in governing ALD initiations. ALDs are most commonly found in areas of solifluction (Harris and Lewkowicz 2000; Lewkowicz and Harris 2005b), where you find frost susceptible soils and permafrost. However, solifluction is more frequently observed in the field than ALDs, suggesting the conditions that ALDs initiate are not commonly found on Arctic hillslopes (Harris and Lewkowicz 2000; Lewkowicz and Harris 2005a). However, when ALDs do initiate it is common to get tens to hundreds of landslides initiating in a single event (Rudy et al. 2016). This study suggests that the conditions needed to initiate ALDs require very high proportions of ground ice concentrated at depth in the soil column. Where ground ice distributions have been measured, high proportions of ground ice are relatively uncommon (Zhang et al. 1999). This suggests that the ground ice conditions needed to initiate an ALD are also uncommon, except during extreme events that penetrate into permafrost or an ice-rich transitional layer. Our work suggests that a better understanding of the spatial distribution of ground ice on hillslopes would improve our ability to estimate the susceptibility of slopes to ALD initiation.

Improving the model would involve an additional scenario where ice lenses are concentrated at the top and bottom of the active layer, replicating the field situation from two-sided freezing.

5.5 Conclusion

In this study I have focused on the impact of thawing ice lenses on the stability of a modelled hillslope. Cohesion controls the absolute depth of failure because the impact of ground ice will depend on the cohesive properties of the soil. Our analysis shows that to generate factors of safety close to the stability limit, a large network of wide ice lenses is needed along with a sufficient magnitude of pore pressure during thawing. If ice lenses are too small or have larger gaps between them the hillslope remains relatively stable. When I kept ice lens volume the same I found that a uniform and linear distribution of ice lenses produced a more stable slope compared to a non-linear distribution. Therefore, the proportion of ice lenses along the failure plane is more important than ground ice volume at initiating failure. Testing the impact of thaw propagation rates showed no difference in the factors of safety between high and low rates. Based on our model results I suggest that the conditions required to initiate ALDs is the rapid thawing of highly concentrated ground ice at depth. Future research should focus on field measurements of ground ice distribution on Arctic hillslopes and their relationship with ALDs.

Chapter 6

Discussion and future work

6.1 Overview and synthesis

To understand what impact a warming Arctic climate (Cohen et al. 2014) will have on periglacial landforms in permafrost regions requires quantifying their spatial extent at a regional scale. Many insightful studies have demonstrated the mechanisms controlling periglacial landform processes at a local scale such as the formation of blockfields (Ballantyne 2010), movement of solifluction (Harris et al. 2008c), formation of scree slopes (Hinchliffe et al. 1998), and other periglacial processes (Humlum 2000; Christiansen 2005; Ross et al. 2007). However, only a few studies have tried to quantify landforms at a regional scale in mountainous arctic landscapes (Bartsch et al. 2008; Bartsch et al. 2009). In this thesis, I addressed the current knowledge gap by researching (i) the role of topography, at a regional scale, in affecting the spatial distribution of periglacial landforms and sediment fluxes (ii) the impact of pore pressures on hillslope stability at a regional scale and within the active layer. This research was spread over three chapters. In chapter 3, I used digital elevation models of Svalbard to create a landform classification model to understand the relative spatial distribution of periglacial processes and make estimates of sediment fluxes from these landforms. In chapter 4, I applied the

classification model in the Brooks Range, Alaska. In addition, I examined the spatial distribution of active layer detachments to understand the topographic controls for their initiation. In chapter 5, I examined the triggering conditions required to initiate ALDs. I tested the following hypotheses:

6.1.1 Hypotheses

H1: *The relative spatial distribution of periglacial landforms and their impact on sediment fluxes in mountainous Arctic landscapes can be quantified by automating the classification of landforms using topographic parameters derived from digital elevation models.*

I developed a statistical model that classified two study sites, Endalen and Ringdalen, into seven landform types; Allochthonous material, Alluvial fan, Blockfield, floodplain, bedrock, scree, and solifluction, based on three topographic parameters; relative local relief, topographic roughness, and slope gradient. I found that bedrock, solifluction, and blockfields were readily distinguished by the model, with bedrock outcrops modelled at a higher resolution than was possible to map via remote sensing. Scree slopes were difficult to distinguish from the ubiquitous vegetated allochthonous slopes, suggesting a similar origin for these deposits. My mapping demonstrates that on Svalbard, solifluction and scree slope development are the dominant hillslope processes acting on this landscape and that sediment fluxes are greatest in solifluction. In the Brooks Range, the classification model performed well in a region of high relief, similar to Svalbard. However, the model had to be modified for low relief topography. Even then, separating the fluvial landforms and solifluction was not possible but solifluction was successfully modelled.

H2: *Active layer detachments occur in convergent topography on soliflucting hillslopes.*

Using an infinite slope analysis I was able to model hillslopes stability at different depths, pore pressures, and shear strength parameters. Despite not being able to separate ALDs from landforms using my classification model I have observed that ALDs are coincident in areas of solifluction in Nukatpiat, Alaska. In terms of shear strength of the active layer, low levels of cohesion are important for reducing stability but conversely they also prevent widespread failures. ALDs in Nukatpiat strongly correlate with the drainage network and are rarely found in isolation but cluster in regions of convergence where solifluction occurs. Areas of convergence are known to form water-tracks and reflect the drainage work of the region (McNamara et al. 1999). Field studies have demonstrated that water-tracks are found extensively in the foothills of the Brooks Range; these convergent regions have elevated ice contents of 50% to 90% (Ping et al. 2008; Trochim et al. 2016a; Trochim et al. 2016b). Given that Nukatpiat is located in the Brooks Range with the same topographic characteristics as other study sites in the same region e.g. (Trochim et al. 2016a), I believe that these ALDs were caused by excess pore pressures from thawing ice lenses and reduced shear strength form annual solifluction that reduces the effective cohesion to near residual (Harris and Lewkowicz 2000). The model showed that with a deeper active layer, less excess pore pressure is needed to cause instability.

H3: *The spatial distribution of ground ice in the active layer and its location along the failure plane control hillslope instability.*

I tested this hypothesis by parameterising a 2-D slope stability model called GeoSlope (Krahn 2004), which calculated slope stability using the Morgenstern and Price method of slices (Morgenstern and Price 1965). I varied the distribution of ice lenses and demonstrated that a power law distribution of ice lenses causes greater instability compared to a linear increase and uniform distribution of ice lenses throughout the active layer. I then show that the more connected ice lenses are the greater the impact

they have on stability, this reflects the importance of soil hydrology during thaw (Dyke 2004).

6.2 Importance and wider implications

6.2.1 ALDs and permafrost degradation by a warming climate

Across the Arctic, the rate of permafrost thaw is increasing (Osterkamp 2007). This has been linked to a warming climate (Stocker et al. 2013; Pastick et al. 2015). A consequence of thawing ice-rich permafrost is thermokarst which is the collapse, subsidence and/or mass wasting of the ground surface creating landforms such as ALDs, retrogressive thaw slumps, thermal erosion gullies, thermokarst lakes, pits and troughs (Kokelj and Jorgenson 2013). In chapter 4, I demonstrate quantitatively that ALDs in Nukatpiat occur in clusters and are hydrologically connected to the regional drainage network. I attribute this observation to the tendency of drainage networks to have wetter conditions that promote a more ice-rich transition zone between the permafrost and active layer. This hydrological connectivity demonstrates the potential of ALDs to impact the nutrient and sediment budget of Arctic catchments. Balser et al. (2009) calculates that on average, each ALD near Feniak Lake (only 100 km south-east of Nukatpiat) has an area of 12,500 m^2 and displaces 37,500 m^3 of active layer material. Lewkowicz and Harris (2005a) found that ALDs on Ellesmere Island generated the same amount of geomorphic work as other mass wasting processes in high mountain environments over a period of 100 - 200 years. ALDs are known to increase sediment yields and dissolved solutes into streams (Lewkowicz and Kokelj 2002). However, the total mass of sediment and solute released and the impact of such releases depends on the hydrological connectivity of active layer soils to the stream network (Lamoureux and Lafreniere 2009; Dugan et al. 2012; Lewis et al. 2012). Currently, Arctic rivers carry less sediment than

their lower latitude counterparts (Gordeev 2006) because of more frozen ground that prevents erosion, a higher proportion of snowfall than rainfall, fewer storms (Syvitski 2002), and a short runoff season (French 2007). As the Arctic warms and the ground thaws a limiting factor (frozen ground) is reduced, causing an increase in sediment flux because greater discharge can entrain more sediment (Syvitski 2002). A study on the paleo sequences of fluvial deposits in the Brooks Range revealed that increased sedimentation during warmer and wetter conditions in the Pleistocene-Holocene transition from c.a. 12.75 to 11.5 ka BP was due to increased ALD activity caused by deeper thaw and greater precipitation (Mann et al. 2010). Mann et al. (2010) claimed that warmer summers increased thaw depth which increased soil pore pressure which in turn caused widespread mass wasting on hillslopes. The small streams of the Brooks Range were overwhelmed with sediment from mass wasting events that caused rapid aggradation (Mann et al. 2010). Despite their significant contribution to the delivery of sediment and organic carbon to the streams, ALDs are unaccounted for in global climate models. The slope stability model from chapter 5 can be used to assess the susceptibility of a landscape to mass-wasting events.

6.2.2 ALD and hazard

In this thesis, I have conducted a regional scale analysis of disturbances and provide useful information to the geo-hazard community about the risks to infrastructure development. ALDs pose a low direct threat to communities of the Arctic because the majority of ALDs occur in the foothills of mountainous landscapes where human habitation is low. There are exceptions of course, on the 5th of October 2016 the slopes adjacent to Longyearbyen (inhabited by 2000 people) experienced multiple mass-wasting events. Prior the event Svalbard had experienced milder than average autumn temperatures and periods of heavy precipitation. On the day, precipitation was 18 mm, triggering 5,000 m^3 of material downslope onto the road on the valley

side, damaging infrastructure (Setsa 2016). A similar event in July 1972, triggered by prolonged heavy rainfall and warm temperatures caused 7,054 m^3 of material to move downslope onto the town of Longyearbyen (Larsson 1982). These mass-wasting events demonstrate that landsliding in the Arctic can be triggered by high precipitation rather than thaw. However, by developing physical models such as the one in chapter 5 we can better understand the extent of the landslide hazard. In Salluit, the Canadian Arctic, ALDs that initiated between 1998 and 2005 were caused by an increase in active layer thickness due to increasing number of warmer summers (Allard et al. 2012). On the 5th of September 1998, an ALD initiated close to an urban development project. As a result, 20 new houses were demolished and the land declared unsafe for habitation (Allard et al. 2012). Using slope stability models such as the one in chapter 5 would help developers determine the potential stability of hillslopes adjacent to infrastructure development, avoiding demolition of infrastructure projects.

In the Brooks Range the greatest hazard that ALDs pose is to the Dalton highway and the adjacent Trans Alaska oil pipeline. The Dalton highway is the only road that links Prudhoe Bay on the north coast of Alaska to Anchorage on the southern coast of Alaska. Prudhoe Bay is dependent on the highway for importing resources during the winter. Construction of the adjacent oil pipeline began in 1975 and currently transports 2 million barrels of oil a day (Walker et al. 2008). Mass wasting events have been observed close to the highway and pipeline (Bowden et al. 2008; Walker et al. 2008; Daanen et al. 2012). In Arctic Canada, near the Great Bear Lake, is the Norma Wells pipeline that transports 30,000 barrels of oil per day (Hanna et al. 1998). Shortly after the 1994 and 1995 forest fires ALDs were observed to initiate just downslope to the pipeline route (Hanna et al. 1998). The ground around the ALD sites was stabilized with geoengineering techniques. Models such as the one in chapter 5 can be used to help determine regions where the ground can be stabilised before can ALDs occur, with a focus on infrastructure.

6.2.3 ALDs and organic carbon

ALDs increase the input of solutes and organic carbon into the stream network during mass wasting events (Lafreniere and Lamoureux 2013; Lamoureux and Lafreniere 2014). Much of the organic carbon in permafrost is either mineralised or released as CO_2 and CH_4. If the organic carbon escapes degradation it can be eroded, transferred to rivers and deposited in marine sediments. Here it can contribute to long-term geological CO_2 sinks (Hilton et al. 2015).

Beamish et al. (2014) found that the short-term impact of ALDs on the carbon balance was minimal. In chapter 2, I demonstrated that regions of convergence such as water tracks are prone to failure. As a result catchments with such areas are most prone to experiencing greater input sediment, solute, and organic carbon potentially causing ecological change.

ALDs act to introduce nutrients into arctic streams that provide optimal conditions to stimulate microbial activity and promote the release of more CO_2 and CH_4 into the atmosphere, amplifying the climate change impact on the Arctic, leading to more microbial activity and ALD activity and so a positive feedback loop is created (Pautler et al. 2010).

6.2.4 Extent of landform processes in the Arctic

Currently, the amount of data collected by remote sensing is greater than the amount that can be processed and analysed. The Polar Geospatial Centre in October 2017 released over 50 TB of 2 m, 5 m, and 8 m high-resolution digital elevation data for all land area north of 60° N latitude, a dataset that is continually growing (Showstack 2017). The analysis of large datasets by professional geomorphologists can be time-consuming, which at a regional scale is not feasible and automation is needed. Automation allows for larger areas to be covered faster (Hjort et al. 2014). Other benefits of automation include reducing human error (but introducing machine error),

facilitating comparable results and model transferability, and reducing processing time (Romstad 2001; Dragut and Blaschke 2006; Hjort and Luoto 2006). Many studies have used statistical analyses to automate the classification of DEMs into landform units (Etzelmüller et al. 2001; Luoto and Seppala 2002; Hjort and Luoto 2006; Prima et al. 2006; Bartsch et al. 2008; Marmion et al. 2009; Ridefelt et al. 2010; Aalto and Luoto 2014; Hjort et al. 2014). Some use complicated algorithms (Romstad and Etzelmüller 2012), others use multiple DEM derived topographic parameters (Rudy et al. 2017), or have developed models that are site-specific (Luoto and Seppala 2002). In chapter 3, I developed a model that classifies a DEM into seven landforms based on the landform's linear relationship with three topographic parameters. I then successfully transferred this model to a different Arctic region underlain with cold permafrost, the Brooks Range in Alaska. Creating a transferable classification model of multiple landforms hasn't been attempted. Current studies have tried to fit non-linear trends between geomorphological landforms and environmental factors but this has produced unrealistic and complex models that are non-transferable.

Solifluction has been modelled in previous studies (Etzelmüller et al. 2001; Ridefelt et al. 2010; Hjort et al. 2014). However, there are few studies that model landforms to understand their spatial extent of landforms, and their role in the sediment budget of mountainous landscapes (Bartsch et al. 2002; Bartsch et al. 2009). I demonstrated in chapter 3 the potential benefits of creating an automated classification. Using this landform classification model I was able to quantify the spatial extent of landforms on Svalbard and in Alaska. On Svalbard, I found that solifluction was one of the major landforms to dominate the landscape in terms of extent and contribution to sediment flux. Solifluction rates and processes have been measured at a local scale (Rapp 1960a; Matsuoka 2001a; Harris et al. 2011) but these don't explain the regional variability of solifluction. With the ability to map solifluction at the regional scale it will be possible to establish the quantitative relationship between solifluction and climate (Ridefelt and Boelhouwers 2006; Aalto

and Luoto 2014; Aalto et al. 2014). One way of accomplishing this is by repeated topographic surveys called difference digital elevation models (DoD). DoDs can help determine geomorphic change and estimate sediment budgets. It has been successful at estimating denudation for rivers in the Scottish highlands (Wheaton et al. 2010), monitoring the movement of sediment along shorelines (Brock and Purkis 2009), and movement of sediment in Arctic mountainous environments using repeated scans from a terrestrial laser scanner (Kociuba 2017). The landscape classification model from chapter 3 can be used in conjunction with DoDs to quantify how landscapes are changing over time. Therefore, establishing the impact of a warming Arctic on landform processes rates and spatial extent.

6.2.5 GIS and Python as a tool for periglacial geomorphologists

DEMs are now freely available at 2 m and 5 m resolution for the entire Arctic (Showstack 2017) and programming languages can process large datasets in a short amount of time. This permits patterns of instability to be modelled at a regional scale, limited by DEM resolution. It is now possible to expand on the knowledge of local empirical studies e.g. (Ballantyne 2010; Harris et al. 2011; Ballantyne 2013) to create a more precise physical model of processes at regional scales. I have shown that it is possible to integrate freely available geospatial datasets into the free open-source data analysis environment of Python (Van Rossum and Drake 2003), making the spatial modelling of periglacial landforms more attractive to future researchers.

6.3 Research opportunities and future work

6.3.1 Quantify the distribution of ground ice along a hillslope profile

In chapters 5 and 6, I assessed the impact of the spatial distribution of ice lenses on the stability of a hillslope based on laboratory experiments by Harris et al. (2008c). The model demonstrated that the likelihood of landsliding increased when segregated ice was concentrated at the active layer/permafrost boundary and when there was a higher proportion of bigger ice lenses along the hillslope. Many studies have taken borehole measurement to quantify ground ice concentration (Mackay 1981; Kokelj and Burn 2005). However, there is a lack of field data on the spatial distribution of ground ice along the length of hillslopes. Harris and Lewkowicz (2000) observed that pore pressures were highest at mid-slopes, indicating that ice lenses are either concentrated at the centre of the slope or that groundwater from thawing ice lenses at the top of the slope is moving downslope and concentrating at the mid-slopes. In addition, the head scarp of mapped ALDs from satellite imagery in chapter 3 are located not at the top but three-quarters the way up the hillslopes. This suggests that the lateral distribution of ground ice along a hillslope is the next step to understanding ALDs. To do this I would suggest geophysical surveys before the summer thaw. Geophysical surveys have the potential to be powerful tools for constraining the thermal and structural characteristics of the active layer, because of the large contrast between the electromagnetic properties of ice, water, and sediments (Moorman et al. 2003; Ross et al. 2007; De Pascale et al. 2008). Ground penetrating radar allows for quantifying ground characteristics and stratigraphy over a large area in a short amount of time. Moorman et al. (2003) used ground penetrating radar (GPR) to map the depth of thaw along a transect parallel to the Norman Wells Pipeline. They were able to determine that subsidence was caused by the presence of ice-rich soil.

However, the added complication of quantifying ground ice volume in the active layer is the addition of other materials with different resistivity's. To prevent this I suggest calibrating the GPR using borehole data.

6.3.2 Modelling the impact of tundra fires on ground ice thaw and hillslope stability

In this thesis, I have modelled the impact of thawed ice lenses on slope stability. This is the mechanism driving ALDs. However, what I have overlooked are the triggers of this mechanism such as days of bright sunshine, warm weather, rainfall, and tundra fires. Each of these triggers is a source of heat that can propagate a thawing front into the active layer. Tundra fires initiate ALDs because they remove the insulating organic mat/vegetation cover and expose the permafrost/mineral soil beneath. This has three effects: (1) increases the surface soil conductivity; (2) reduced surface albedo; (3) increases insolation on the ground surface (Liljedahl et al. 2007) thus causing more heat to conduct deeper into the permafrost, reaching the ice-rich transient layer. Some studies have observed ALDs initiating months after a fire (Lewkowicz and Harris 2005a). Hanna et al. (1998) observed failures adjacent to the Norman Wells pipeline in Alberta, Canada. These failures occurred 'shortly' after a fire in 1994 (Hanna et al. 1998), although the authors did note that ALDs initiated during the following spring.

Mann et al. (2010) claim that as summers become warmer and drier, fire-prone shrubs will expand across the tundra in the Brooks Range (Tape et al. 2006). This will increase the frequency of tundra fires that remove soil organic horizons, exposing the mineral soil beneath (Mann et al. 2010). Even though this mechanism is well known, e.g. Liljedahl et al. (2007), there is still a research gap for quantifying the amount of heat and ground ice required to thaw enough ground ice to cause instability. From chapter 3 we know that a high concentration of ground ice at depth is needed but

not how much. As it is difficult to assess the ground ice conditions prior to a slope failure. Modelling would provide much-needed insight by allowing researchers to quantify the amount of burning that is needed, how thick an organic mat needs to be, and how much ground ice is needed to initiate ALDs. Nishimura et al. (2009) modelled changing ground ice conditions in cold regions in response to climate change. They synthesised climate change predictions, DEMs and remote sensing data to produce regional maps of future geocryological conditions which aided in producing regional maps of expected geohazards caused by thawing permafrost. Nishimura et al. (2009) used a thermal finite element model to understand the non-linear geothermal conduction caused by the soil properties, latent heat effects, insulation effect of snow cover, and the stratigraphic variation in soil properties. Such a study on the impact of tundra/forest fires on Arctic hillslopes would provide an insight into their future impact with a warming Arctic climate.

Chapter 7

Thesis conclusion

I developed a landform classification model that uses a combination of three topographic parameters; slope gradient, relative local relief, and topographic roughness, to best model the spatial distribution of periglacial landforms in the mountainous landscape of Endalen and Ringdalen on Svalbard and the Brooks Range, Alaska. Bedrock, blockfields, and solifluction were identified with a high degree of accuracy, with bedrock outcrops modelled at a greater resolution than was possible to map using satellite imagery. Scree slopes were difficult to separate from the ubiquitous vegetated allochthonous slopes, suggesting a similar genesis for these landforms. The model demonstrated that on Svalbard, solifluction and scree slope development are the dominant hillslope processes acting on this landscape and that sediment fluxes are greatest in solifluction. In the Brooks Range, the classification model performed well in a region of high relief, similar to Svalbard. However, the model had to be modified for low relief topography. In both Svalbard and the Brooks Range, separating fluvial landforms from each other was problematic due to similar topographic signatures.

There are multiple ways to improve the landform classification model. First, an additional step is needed to remove misclassified pixels within a region of correctly classified pixels for example by using a smoothing algorithm. Second, by the

addition of other landforms such as debris cones. Third, by switching my pixel-based model to an object-orientated model would increase process time. However, to improve classification accuracy, greater concern should be given to exploring the relationship of topographic parameters to landform shape and spatial extent. This and other similar DEM-based models can be used for reconnaissance geomorphological mapping of large study areas.

A combination of manual ALD mapping, solifluction modelling, and infinite slope analysis in the Brooks Range revealed that instabilities are coincident with convergent topography on soliflucting hillslopes. I attribute this to higher moisture availability that feeds the growth of ice lenses at the permafrost active layer boundary, called the transient layer. Furthermore, small amounts of cohesion in modelled active layer soils prevent widespread hillslope failure. This implies that soil cohesion must be reduced to near residual by annual solifluction to cause failure coincident with mapped ALDs. As active layer depth increased, less excess pore pressures were needed to cause failure. However, not all modelled instabilities corresponded to mapped failures. A 2-D slope stability analysis revealed that failure can only occur under certain ground ice conditions. When ice lenses were concentrated at the base of the active layer hillslopes became more unstable. This type of ice lens distribution produced a large network of wide ice lenses along the failure plain. During thaw, this generated high levels of excess pore pressure. This suggests that the proportion of ice lenses along the failure plain was more important than volume at initiating instability, with cohesion acting as the limiting factor for the depth of failure. The stability modelling results here reflect the conclusions of field-based studies (Harris and Lewkowicz 2000; Lewkowicz and Harris 2005a; Harris et al. 2008c).

Due to a warming Arctic, permafrost is expected to continue thawing, creating an ever more dynamic active layer. Consequently, the relative regional extent of periglacial landforms in mountainous Arctic environments is expected to change. Arctic hillslopes will become more unstable during summer thaw. ALDs appear to

act as a dominant process in shaping future Arctic landscapes. ALDs will also pose a greater hazard to Arctic infrastructure and act as a major force for environmental change. Future research should focus on combining repeated remote sensing surveys with landform classification models to understand what impact thawing permafrost will have on landform processes and sediment/solute fluxes at a regional scale. I believe that, by quantifying sub-surface ground ice conditions below convergent topography in Arctic hillslopes with field measurements, it would be possible to validate the models presented here and help establish the role of thawing ground ice as a triggering mechanism for active layer detachments.

References

Aalto, J. and Luoto, M. (2014). Integrating climate and local factors for geomorphological distribution models. *Earth Surface Processes and Landforms* **39**, 1729–1740.

Aalto, J., Venalainen, A., Heikkinen, R. K., and Luoto, M. (2014). Potential for extreme loss in high-latitude Earth surface processes due to climate change. *Geophysical Research Letters* **41**, 3914–3924.

Abellan, A., Calvet, J., Manuel Vilaplana, J., and Blanchard, J. (2010). Detection and spatial prediction of rockfalls by means of terrestrial laser scanner monitoring. *Geomorphology* **119**, 162–171.

Akerman, H. J. (1984). Notes on talus morphology and processes in Spitsbergen. *Geografiska Annaler Series a-Physical Geography* **66**, 267–284.

Akerman, H. J. and Johansson, M. (2008). Thawing permafrost and thicker active layers in sub-arctic Sweden. *Permafrost and Periglacial Processes* **19**, 279–292.

Akerman, H. J. (2005). Relations between slow slope processes and active-layer thickness 1972–2002, Kapp Linné, Svalbard. *Norsk Geografisk Tidsskrift-Norwegian Journal of Geography* **59**, 116–128.

Akerman, H. (1996). Slow mass movements and climatic relationships, 1972–1994, Kapp Linné, West Spitsbergen. *Advances in hillslope processes* **2**, 1219–1256.

Allard, M., Caron, S., and Begin, Y. (1996). Climatic and ecological controls on ice segregation and thermokarst: The case history of a permafrost plateau in northern Quebec. *Permafrost and Periglacial Processes* **7**, 207–227.

Allard, M., Lemay, M., Barrette, C., L'Hérault, E., Sarrazin, D., Bell, T., and Doré, G. (2012). Permafrost and climate change in Nunavik and Nunatsiavut: Importance for municipal and transportation infrastructures. *Nunavik and Nunatsiavut: From science to policy. An Integrated Regional Impact Study (IRIS) of climate change and modernization*, 171–197.

Andersen, J. L., Egholm, D. L., Knudsen, M. F., Jansen, J. D., and Nielsen, S. B. (2015). The periglacial engine of mountain erosion-Part 1: Rates of frost cracking and frost creep. *Earth Surface Dynamics* **3**, 447.

Anderson, M. G. and Richards, K. S. (1987). Slope stability: geotechnical engineering and geomorphology. John Wiley & Sons.

Anderson, R. S. (2002). Modeling the tor-dotted crests, bedrock edges, and parabolic profiles of high alpine surfaces of the Wind River Range, Wyoming. *Geomorphology* **46**, 35–58.

Anderson, R. and Anderson, S. (2010). Geomorphology: The Mechanics and Chemistry of Landscapes. Cambridge: Cambridge University Press, 637.

Andersson, J. G. (1906). Solifluction, a component of subaerial denudation. *The Journal of Geology* **14**, 91–112.

Andre, M. F. (1997). Holocene rockwall retreat in Svalbard: A triple-rate evolution. *Earth Surface Processes and Landforms* **22**, 423–440.

ArcGIS, E. (2013). 10.2. Environmental Systems Research Institute. *Inc Redlands, CA*.

Armstrong, R. N. and Martz, L. W. (2003). Topographic parameterization in continental hydrology: a study in scale. *Hydrological Processes* **17**, 3763–3781.

Asselen, S. van and Seijmonsbergen, A. C. (2006). Expert-driven semi-automated geomorphological mapping for a mountainous area using a laser DTM. *Geomorphology* **78**, 309–320.

Ballantyne, C. K. (2013). A 35-Year Record of Solifluction in a Maritime Periglacial Environment. *Permafrost and Periglacial Processes* **24**, 56–66.

Ballantyne, C. K. (2002). Paraglacial geomorphology. *Quaternary Science Reviews* **21**, 1935–2017.

Ballantyne, C. K. (2010). A General Model of Autochthonous Blockfield Evolution. *Permafrost and Periglacial Processes* **21**, 289–300.

Ballantyne, C. K. (2018). Periglacial Geomorphology. John Wiley & Sons.

Ballantyne, C. K. and Harris, C. (1994). The Periglaciation of Great Britain. CUP Archive.

Balser, A., Gens, R., Mack, M., Walker, D., Jones, J. J., and Wagner, D. (2015). Retrogressive thaw slumps and active layer detachment slides in the Brooks Range and foothills of northern Alaska: terrain and timing. Thesis.

Balser, A., Gooseff, M., Jones, J., and Bowden, W. (2009). *Thermokarst Distribution and Relationships to Landscape Characteristics in the Feniak Lake Region, Noatak National Preserve, Alaska.* Report. National Park Service Arctic Network.

Balser, A. W., Jones, J. B., and Gens, R. (2014). Timing of retrogressive thaw slump initiation in the Noatak Basin, northwest Alaska, USA. *Journal of Geophysical Research-Earth Surface* **119**, 1106–1120.

Barlow, J., Franklin, S., and Martin, Y. (2006). High spatial resolution satellite imagery, DEM derivatives, and image segmentation for the detection of mass wasting processes. *Photogrammetric Engineering and Remote Sensing* **72**, 687–692.

Barsch, D. (1993). Periglacial geomorphology in the 21st-century. *Geomorphology* **7**, 141–163.

Bartsch, A., Gude, M., and Gurney, S. D. (2008). A geomatics-based approach for the derivation of the spatial distribution of sediment transport processes in periglacial mountain environments. *Earth Surface Processes and Landforms* **33**, 2255–2265.

Bartsch, A., Gude, M., and Gurney, S. D. (2009). Quantifying sediment transport processes in periglacial mountain environments at a catchment scale using geomorphic process units. *Geografiska Annaler Series a-Physical Geography* **91A**, 1–9.

Bartsch, A., Gude, M., Jonasson, C., and Scherer, D. (2002). Identification of geomorphic process units in Karkevagge, northern Sweden, by remote sensing and digital terrain analysis. *Geografiska Annaler Series a-Physical Geography* **84A**, 171–178.

Beamish, A., Neil, A., Wagner, I., and Scott, N. A. (2014). Short-term impacts of active layer detachments on carbon exchange in a High Arctic ecosystem, Cape Bounty, Nunavut, Canada. *Polar Biology* **37**, 1459–1468.

Berthling, I., Etzelmüller, B., Larsen, C. K., and Nordahl, K. (2002). Sediment fluxes from creep processes at Jomfrunut, southern Norway. *Norsk Geografisk Tidsskrift-Norwegian Journal of Geography* **56**, 67–73.

Bertran, P. and Fabre, R. (2005). Pleistocene cryostructures and landslide at Petit-Bost (southwestern France, 45 degrees N). *Geomorphology* **71**, 344–356.

Beven, K. and Kirkby, M. J. (1979). A physically based, variable contributing area model of basin hydrology/Un modèle à base physique de zone d'appel variable de l'hydrologie du bassin versant. *Hydrological Sciences Journal* **24**, 43–69.

Beylich, A. A. (2008). Sediment fluxes and sediment budget in Latnjavagge and the potential of applying unified methods for integrating investigations on sediment fluxes and budgets in cold-environment catchments. *Geology for Society. Geological Survey of Norway Special Publication* **11**, 111–130.

Bintanja, R. and Andry, O. (2017). Towards a rain-dominated Arctic. *Nature Climate Change* **7**, 263–+.

Blais-Stevens, A., Kremer, M., Bonnaventure, P. P., Smith, S. L., Lipovsky, P., and Lewkowicz, A. G. (2015). Active Layer Detachment Slides and Retrogressive Thaw Slumps Susceptibility Mapping for Current and Future Permafrost Distribution, Yukon Alaska Highway Corridor. *Engineering Geology for Society and Territory, Vol 1: Climate Change and Engineering Geology*, 449–453.

Boelhouwers, J. (2004). New perspectives on autochthonous blockfield development. *Polar Geography* **28**, 133–146.

Bolongaro-Crevenna, A., Torres-Rodriguez, V., Sorani, V., Frame, D., and Ortiz, M. A. (2005). Geomorphometric analysis for characterizing landforms in Morelos State, Mexico. *Geomorphology* **67**, 407–422.

Bonnaventure, P. P. and Lamoureux, S. F. (2013). The active layer: A conceptual review of monitoring, modelling techniques and changes in a warming climate. *Progress in Physical Geography* **37**, 352–376.

Booth, A. M., Roering, J. J., and Perron, J. T. (2009). Automated landslide mapping using spectral analysis and high-resolution topographic data: Puget Sound lowlands, Washington, and Portland Hills, Oregon. *Geomorphology* **109**, 132–147.

Bowden, W. B., Gooseff, M. N., Balser, A., Green, A., Peterson, B. J., and Bradford, J. (2008). Sediment and nutrient delivery from thermokarst features in the foothills of the North Slope, Alaska: Potential impacts on headwater stream ecosystems. *Journal of Geophysical Research-Biogeosciences* **113**.

Brenning, A. (2005). Spatial prediction models for landslide hazards: review, comparison and evaluation. *Natural Hazards and Earth System Sciences* **5**, 853–862.

Brenning, A. (2009). Benchmarking classifiers to optimally integrate terrain analysis and multispectral remote sensing in automatic rock glacier detection. *Remote Sensing of Environment* **113**, 239–247.

Brock, J. C. and Purkis, S. J. (2009). The Emerging Role of Lidar Remote Sensing in Coastal Research and Resource Management. *Journal of Coastal Research* **25**, 1–5.

Brown, J., Ferrians, O., Heginbottom, J. A., and Melnikov, E. (2002a). *Circum-Arctic Map of Permafrost and Ground-Ice Conditions, Version 2. Permafrost extent*. http://nsidc.org/data/GGD318.

Brown, J., Ferrians, O., Heginbottom, J. A., and Melnikov, E. (2002b). *Circum-Arctic Map of Permafrost and Ground-Ice Conditions, Version 2. Relative abundance of ground ice in the upper 20 m is estimated in percent volume*. http://nsidc.org/data/GGD318.

Brown, J., Hinkel, K. M., and Nelson, F. (2000). The circumpolar active layer monitoring (calm) program: Research designs and initial results 1. *Polar geography* **24**, 166–258.

Burn, C. R. and Kokelj, S. V. (2009). The Environment and Permafrost of the Mackenzie Delta Area. *Permafrost and Periglacial Processes* **20**, 83–105.

Burn, C. (1988). The development of near-surface ground ice during the Holocene at sites near Mayo, Yukon Territory, Canada. *Journal of Quaternary Science* **3**, 31–38.

Burn, C. and Michel, F. (1988). Evidence for recent temperature-induced water migration into permafrost from the tritium content of ground ice near Mayo, Yukon Territory, Canada. *Canadian Journal of Earth Sciences* **25**, 909–915.

Burrough, P. A., McDonnell, R. A., and Lloyd, C. D. (2015). Principles of geographical information systems. Oxford University Press.

Cannone, N., Lewkowicz, A. G., and Guglielmin, M. (2010). Vegetation colonization of permafrost-related landslides, Ellesmere Island, Canadian High Arctic. *Journal of Geophysical Research-Biogeosciences* **115**.

Christiansen, H. H. (2005). Thermal regime of ice-wedge cracking in adventdalen, Svalbard. *Permafrost and Periglacial Processes* **16**, 87–98.

Cogley, J. G. and McCann, S. B. (1976). An Exceptional Storm and Its Effects in the Canadian High Arctic. *Arctic and Alpine Research* **8**, 105–110.

Cohen, J., Screen, J. A., Furtado, J. C., Barlow, M., Whittleston, D., Coumou, D., Francis, J., Dethloff, K., Entekhabi, D., Overland, J., and Jones, J. (2014). Recent Arctic amplification and extreme mid-latitude weather. *Nature Geoscience* **7**, 627–637.

Couture, N. J. (2000). Sensitivity of Permafrost Terrain in a High Arctic Polar Desert: An Evaluation of Response to Disturbance Near Eureka, Ellesmere Island, Nunavut.

Curry, A. M. and Black, R. (2003). Structure, sedimentology and evolution of rockfall talus, Mynydd Du, south Wales. *Proceedings of the Geologists Association* **114**, 49–64.

Daanen, R. P., Grosse, G., Darrow, M. M., Hamilton, T. D., and Jones, B. M. (2012). Rapid movement of frozen debris-lobes: implications for permafrost degradation and slope instability in the south-central Brooks Range, Alaska. *Natural Hazards and Earth System Sciences* **12**, 1521–1537.

Dahl, R. (1966). Block fields, weathering pits and tor-like forms in the Narvik Mountains, Nordland, Norway. *Geografiska Annaler. Series A. Physical Geography*, 55–85.

De Pascale, G. P., Pollard, W. H., and Williams, K. K. (2008). Geophysical mapping of ground ice using a combination of capacitive coupled resistivity and ground-penetrating radar, Northwest Territories, Canada. *Journal of Geophysical Research-Earth Surface* **113**, 15.

Debella-Gilo, M. and Etzelmüller, B. (2009). Spatial prediction of soil classes using digital terrain analysis and multinomial logistic regression modeling integrated in GIS: Examples from Vestfold County, Norway. *Catena* **77**, 8–18.

DiBiase, R. A., Heimsath, A. M., and Whipple, K. X. (2012). Hillslope response to tectonic forcing in threshold landscapes. *Earth Surface Processes and Landforms* **37**, 855–865.

Dikau, R., Brabb, E., Mark, R. K., and Pike, R. J. (1995). Morphometric landform analysis of New Mexico. *Zeitschrift fur Geomorphologie Supplementband*, 109–126.

Dragut, L. and Blaschke, T. (2006). Automated classification of landform elements using object-based image analysis. *Geomorphology* **81**, 330–344.

Dugan, H. A., Lamoureux, S. F., Lewis, T., and Lafreniere, M. J. (2012). The Impact of Permafrost Disturbances and Sediment Loading on the Limnological Characteristics of Two High Arctic Lakes. *Permafrost and Periglacial Processes* **23**, 119–126.

Dyke, L. (2004). "Stability of frozen and thawing slopes in the Mackenzie Valley, Northwest Territories". In: *Proceedings of the 57th Canadian Geotechnical Conference, Quebec City, Quebec, Session G*. Vol. 1, 31–38.

Eckerstorfer, M., Christiansen, H. H., Vogel, S., and Rubensdotter, L. (2013). Snow cornice dynamics as a control on plateau edge erosion in central Svalbard. *Earth Surface Processes and Landforms* **38**, 466–476.

Eichel, J., Corenblit, D., and Dikau, R. (2016). Conditions for feedbacks between geomorphic and vegetation dynamics on lateral moraine slopes: a biogeomorphic feedback window. *Earth Surface Processes and Landforms* **41**, 406–419.

Etzelmüller, B., Odegard, R. S., Berthling, I., and Sollid, J. L. (2001). Terrain parameters and remote sensing data in the analysis of permafrost distribution and periglacial processes: Principles and examples from southern Norway. *Permafrost and Periglacial Processes* **12**, 79–92.

Etzelmüller, B. and Sulebak, J. R. (2000). Developments in the use of digital elevation models in periglacial geomorphology and glaciology. *Physische Geographie* **41**, 35–58.

Evans, I. S. (1972). General geomorphometry, derivatives of altitude, and descriptive statistics. *Spatial analysis in geomorphology*, 17–90.

Favero, P. (2009). Active layer detachment morphology, sedimentology, and mechanisms, Fosheim Peninsula, Ellesmere Island.

Fisher, O. (1866). IV.—On the Disintegration of a Chalk Cliff. *Geological Magazine* **3**, 354–356.

French, H. (2003). The development of periglacial geomorphology: 1-up to 1965. *Permafrost and Periglacial Processes* **14**, 29–60.

French, H. (2007). The Periglacial Environment. New York: Wiley, 458.

French, H. and Shur, Y. (2010). The principles of cryostratigraphy. *Earth-Science Reviews* **101**, 190–206.

Ghosh, S., Stepinski, T. F., and Vilalta, R. (2010). Automatic Annotation of Planetary Surfaces With Geomorphic Labels. *Ieee Transactions on Geoscience and Remote Sensing* **48**, 175–185.

Giles, P. T. and Franklin, S. E. (1998). An automated approach to the classification of the slope units using digital data. *Geomorphology* **21**, 251–264.

Goodfellow, B. W. (2007). Relict non-glacial surfaces in formerly glaciated landscapes. *Earth-Science Reviews* **80**, 47–73.

Gooseff, M., Balser, A., Bowden, W., and Jones, J. (2009). Effects of Hillslope Thermokarst in Norther Alaska. *Eos* **90**, 29–30.

Gordeev, V. V. (2006). Fluvial sediment flux to the Arctic Ocean. *Geomorphology* **80**, 94–104.

Gruber, S. (2012). Derivation and analysis of a high-resolution estimate of global permafrost zonation. *Cryosphere* **6**, 221–233.

Gruber, S., Hoelzle, M., and Haeberli, W. (2004). Permafrost thaw and destabilization of Alpine rock walls in the hot summer of 2003. *Geophysical Research Letters* **31**.

Gurney, S. D. and Bartsch, A. (2005). Mapping the spatial distribution of geomorphological processes in the Okstindan area of northern Norway, using Geomorphic Process Units as derived from remote sensing and ground survey. *Fennia-International Journal of Geography* **183**, 1–14.

Haas, T. de, Kleinhans, M. G., Carbonneau, P. E., Rubensdotter, L., and Hauber, E. (2015). Surface morphology of fans in the high-Arctic periglacial environment of Svalbard: Controls and processes. *Earth-Science Reviews* **146**, 163–182.

Hales, T. C. and Roering, J. J. (2005). Climate-controlled variations in scree production, Southern Alps, New Zealand. *Geology* **33**, 701–704.

Hales, T. C. and Roering, J. J. (2007). Climatic controls on frost cracking and implications for the evolution of bedrock landscapes. *Journal of Geophysical Research-Earth Surface* **112**, 14.

Hales, T. C. and Roering, J. J. (2009). A frost "buzzsaw" mechanism for erosion of the eastern Southern Alps, New Zealand. *Geomorphology* **107**, 241–253.

Hallet, B., Walder, J., and Stubbs, C. (1991). Weathering by segregation ice growth in microcracks at sustained sub-zero temperatures: verification from an experimental study using acoustic emissions. *Pemafrost and Periglacial Processes*, 283–300.

Hallet, B. (2006). Geology - Why do freezing rocks break? *Science* **314**, 1092–1093.

Hamilton, T. D. (2009). Guide to surficial geology and river-bluff exposures, Noatak National Preserve, northwestern Alaska. US Department, of the Interior, US Geological Survey.

Hammond, E. H. (1964). Analysis of properties in land form geography: an application to broad-scale land form mapping. *Annals of the Association of American Geographers* **54**, 11–19.

Hanna, A. J., McNeill, D., Tchekhovski, A., Fridel, T., and Babkirk, C. (1998). "The effects of the 1994 and 1995 forest fires on the slopes of the Norman Wells pipeline". In: *Proceedings, 7 th International Permafrost Conference, Yellowknife, NWT*, 421–426.

Harris, C. (1981). Periglacial Mass-wasting: A Review of Research. Geo Abstracts.

Harris, C., Arenson, L. U., Christiansen, H. H., Etzemuller, B., Frauenfelder, R., Gruber, S., Haeberli, W., Hauck, C., Holzle, M., Humlum, O., Isaksen, K., Kaab, A., Kern-Lutschg, M. A., Lehning, M., Matsuoka, N., Murton, J. B., Nozli, J., Phillips, M., Ross, N., Seppala, M., Springman, S. M., and Muhll, D. V. (2009). Permafrost and climate in Europe: Monitoring and modelling thermal, geomorphological and geotechnical responses. *Earth-Science Reviews* **92**, 117–171.

Harris, C. and Davies, M. C. R. (2000). Gelifluction: Observations from large-scale laboratory simulations. *Arctic Antarctic and Alpine Research* **32**, 202–207.

Harris, C., Davies, M. C. R., and Coutard, J. P. (1996). An experimental design for laboratory simulation of periglacial solifluction processes. *Earth Surface Processes and Landforms* **21**, 67–75.

Harris, C., Haeberli, W., Vonder Muhll, D., and King, L. (2001a). Permafrost monitoring in the high mountains of Europe: the PACE project in its global context. *Permafrost and Periglacial Processes* **12**, 3–11.

Harris, C. and Lewkowicz, A. G. (1993). Form and internal structure of Active-Layer detachment slides, Fosheim Peninsula, Ellesmere Island, Northwest-Territories, Canada. *Canadian Journal of Earth Sciences* **30**, 1708–1714.

Harris, C. and Lewkowicz, A. G. (2000). An analysis of the stability of thawing slopes, Ellesmere Island, Nunavut, Canada. *Canadian Geotechnical Journal* **37**, 449–462.

Harris, C., Rea, B., and Davies, M. (2001b). Scaled physical modelling of mass movement processes on thawing slopes. *Permafrost and Periglacial Processes* **12**, 125–135.

Harris, C. and Smith, J. S. (2003). Modelling gelifluction processes: the significance of frost heave and slope gradient. *Permafrost, Vols 1 and 2*, 355–360.

Harris, C., Vonder Muhll, D., Isaksen, K., Haeberli, W., Sollid, J. L., King, L., Holmlund, P., Dramis, F., Guglielmin, M., and Palacios, D. (2003). Warming permafrost in European mountains. *Global and Planetary Change* **39**, 215–225.

Harris, C., Kern-Luetschg, M., Christiansen, H. H., and Smith, F. (2011). The Role of Interannual Climate Variability in Controlling Solifluction Processes, Endalen, Svalbard. *Permafrost and Periglacial Processes* **22**, 239–253.

Harris, C., Kern-Luetschg, M., Murton, J., Font, M., Davies, M., and Smith, F. (2008a). Solifluction Processes on Permafrost and Non-permafrost Slopes: Results of a Large-scale Laboratory Simulation. *Permafrost and Periglacial Processes* **19**, 359–378.

Harris, C., Kern-Luetschg, M., Smith, F., and Isaksen, K. (2008b). Solifluction processes in an area of seasonal ground freezing, Dovrefjell, Norway. *Permafrost and Periglacial Processes* **19**, 31–47.

Harris, C., Smith, J. S., Davies, M. C. R., and Rea, B. (2008c). An investigation of periglacial slope stability in relation to soil properties based on physical modelling in the geotechnical centrifuge. *Geomorphology* **93**, 437–459.

Heimsath, A. M., DiBiase, R. A., and Whipple, K. X. (2012). Soil production limits and the transition to bedrock-dominated landscapes. *Nature Geoscience* **5**, 210–214.

Hilton, R. G., Galy, V., Gaillardet, J., Dellinger, M., Bryant, C., O'Regan, M., Groecke, D. R., Coxall, H., Bouchez, J., and Calmels, D. (2015). Erosion of

organic carbon in the Arctic as a geological carbon dioxide sink. *Nature* **524**, 84–U162.

Hinchliffe, S. and Ballantyne, C. K. (1999). Talus accumulation and rockwall retreat, Trotternish, Isle of Skye, Scotland. *Scottish Geographical Journal* **115**, 53–70.

Hinchliffe, S., Ballantyne, C. K., and Walden, J. (1998). The structure and sedimentology of relict talus, Trotternish, northern Skye, Scotland. *Earth Surface Processes and Landforms* **23**, 545–560.

Hjort, J. and Luoto, M. (2006). Modelling patterned ground distribution in Finnish Lapland: An integration of topographical, ground and remote sensing information. *Geografiska Annaler Series a-Physical Geography* **88A**, 19–29.

Hjort, J. and Luoto, M. (2011). Novel theoretical insights into geomorphic process-environment relationships using simulated response curves. *Earth Surface Processes and Landforms* **36**, 363–371.

Hjort, J., Luoto, M., and Seppala, M. (2007). Landscape scale determinants of periglacial features in subarctic Finland: A grid-based modelling approach. *Permafrost and Periglacial Processes* **18**, 115–127.

Hjort, J., Ujanen, J., Parviainen, M., Tolgensbakk, J., and Etzelmüller, B. (2014). Transferability of geomorphological distribution models: Evaluation using solifluction features in subarctic and Arctic regions. *Geomorphology* **204**, 165–176.

Hjort, J., Etzelmüller, B., and Tolgensbakk, J. (2010). Effects of Scale and Data Source in Periglacial Distribution Modelling in a High Arctic Environment, western Svalbard. *Permafrost and Periglacial Processes* **21**, 345–354.

Horton, R. E. (1945). Erosional development of streams and their drainage basins; hydrophysical approach to quantitative morphology. *Geological society of America bulletin* **56**, 275–370.

Hugelius, G., Strauss, J., Zubrzycki, S., Harden, J. W., Schuur, E. A. G., Ping, C. L., Schirrmeister, L., Grosse, G., Michaelson, G. J., Koven, C. D., O'Donnell, J. A., Elberling, B., Mishra, U., Camill, P., Yu, Z., Palmtag, J., and Kuhry, P. (2014). Estimated stocks of circumpolar permafrost carbon with quantified uncertainty ranges and identified data gaps. *Biogeosciences* **11**, 6573–6593.

Hugelius, G., Bockheim, J. G., Camill, P., Eberling, B., Grosse, G., Harden, J. W., Johnson, K., Jorgenson, T., Koven, C., Kuhry, P., et al. (2013). A new data set for estimating organic carbon storage to 3 m depth in soils of the northern circumpolar permafrost region. *Earth System Science Data* **5**, 393–402.

Hugenholtz, C. I. H. and Lewkowicz, A. G. (2002). Morphometry and environmental characteristics of turf-banked solifluction lobes, Kluane Range, Yukon Territory, Canada. *Permafrost and Periglacial Processes* **13**, 301–313.

Humlum, O. (2000). The geomorphic significance of rock glaciers: estimates of rock glacier debris volumes and headwall recession rates in West Greenland. *Geomorphology* **35**, 41–67.

Humlum, O., Instanes, A., and Sollid, J. L. (2003). Permafrost in Svalbard: a review of research history, climatic background and engineering challenges. *Polar Research* **22**, 191–215.

Humlum, O., Christiansen, H. H., and Juliussen, H. (2007). Avalanche-derived rock glaciers in Svalbard. *Permafrost and Periglacial Processes* **18**, 75–88.

Hutchinson, J. (1991). Theme lecture: Periglacial and slope processes. *Geological Society, London, Engineering Geology Special Publications* **7**, 283–331.

Irvin, B. J., Ventura, S. J., and Slater, B. K. (1997). Fuzzy and isodata classification of landform elements from digital terrain data in Pleasant Valley, Wisconsin. *Geoderma* **77**, 137–154.

Iwahashi, J., Watanabe, S., and Furuya, T. (2001). Landform analysis of slope movements using DEM in Higashikubiki area, Japan. *Computers & Geosciences* **27**, 851–865.

Iwahashi, J., Kamiya, I., and Yamagishi, H. (2012). High-resolution DEMs in the study of rainfall- and earthquake-induced landslides: Use of a variable window size method in digital terrain analysis. *Geomorphology* **153**, 29–38.

Iwahashi, J. and Pike, R. J. (2007). Automated classifications of topography from DEMs by an unsupervised nested-means algorithm and a three-part geometric signature. *Geomorphology* **86**, 409–440.

Jaesche, P., Veit, H., and Huwe, B. (2003). Snow cover and soil moisture controls on solifluction in an area of seasonal frost, eastern Alps. *Permafrost and Periglacial Processes* **14**, 399–410.

Jahn, A. (1967). Some features of mass movement on Spitsbergen slopes. *Geografiska Annaler. Series A. Physical Geography*, 213–225.

Jasiewicz, J. and Stepinski, T. F. (2013). Geomorphons - a pattern recognition approach to classification and mapping of landforms. *Geomorphology* **182**, 147–156.

Jolivel, M. and Allard, M. (2013). Thermokarst and export of sediment and organic carbon in the Sheldrake River watershed, Nunavik, Canada. *Journal of Geophysical Research-Earth Surface* **118**, 1729–1745.

Jorgenson, M. T., Shur, Y. L., and Pullman, E. R. (2006). Abrupt increase in permafrost degradation in Arctic Alaska. *Geophysical Research Letters* **33**, 4.

Jorgenson, M. T. (2009). An ecological land survey and landcover map of the Arctic Network. US Department of the Interior, National Park Service, Natural Resource Program Center.

Kirkby, M. J. and Statham, I. (1975). Surface stone movement and scree formation. *Journal of Geology* **83**, 349–362.

Kociuba, W. (2017). Analysis of geomorphic changes and quantification of sediment budgets of a small Arctic valley with the application of repeat TLS surveys. *Zeitschrift für Geomorphologie, Supplementary Issues* **61**, 105–120.

Kokelj, S. V. and Burn, C. R. (2003). Ground ice and soluble cations in near-surface permafrost, Inuvik, Northwest Territories, Canada. *Permafrost and Periglacial Processes* **14**, 275–289.

Kokelj, S. V. and Burn, C. R. (2005). Geochemistry of the active layer and near-surface permafrost, Mackenzie delta region, Northwest Territories, Canada. *Canadian Journal of Earth Sciences* **42**, 37–48.

Kokelj, S. V. and Jorgenson, M. T. (2013). Advances in Thermokarst Research. *Permafrost and Periglacial Processes* **24**, 108–119.

Kokelj, S. V. and Lewkowicz, A. G. (1999). Salinization of permafrost terrain due to natural geomorphic disturbance, Fosheim Peninsula, Ellesmere Island. *Arctic* **52**, 372–385.

Krahn, J. (2004). Stability modeling with SLOPE/W: An engineering methodology. *GEOSLOPE/W International Ltd. Calgary, Alberta, Canada*.

Lacerda, W., Ehrlich, M., Fontoura, S. A., and Sayao, A. S. (2004). Landslides: Evaluation and Stabilization/Glissement de Terrain: Evaluation et Stabilisation, Set of 2 Volumes: Proceedings of the Ninth International Symposium on Landslides, June 28-July 2, 2004 Rio de Janeiro, Brazil. CRC Press.

Lafreniere, J. and Lamoureux, F. (2013). Thermal Perturbation and Rainfall Runoff have Greater Impact on Seasonal Solute Loads than Physical Disturbance of the Active Layer. *Permafrost and Periglacial Processes* **24**, 241–251.

Lafreniere, M. J., Laurin, E., and Lamoureux, S. F. (2013). The Impact of Snow Accumulation on the Active Layer Thermal Regime in High Arctic Soils. *Vadose Zone Journal* **12**.

Lamoureux, S., Lafreniere, J., and Favaro, A. (2014). Erosion dynamics following localized permafrost slope disturbances. *Geophysical Research Letters* **41**, 5499–5505.

Lamoureux, S. and Lafreniere, M. (2009). Fluvial Impact of Extensive Active Layer Detachments, Cape Bounty, Melville Island, Canada. *Arctic Antarctic and Alpine Research* **41**, 59–68.

Lamoureux, S. and Lafreniere, M. (2014). Seasonal fluxes and age of particulate organic carbon exported from Arctic catchments impacted by localized permafrost slope disturbances. *Environmental Research Letters* **9**.

Landvik, J. Y., Bondevik, S., Elverhoi, A., Fjeldskaar, W., Mangerud, J., Salvigsen, O., Siegert, M. J., Svendsen, J. I., and Vorren, T. O. (1998). The last glacial maximum of Svalbard and the Barents Sea area: Ice sheet extent and configuration. *Quaternary Science Reviews* **17**, 43–75.

Larsson, S. (1982). Geomorphological effects on the slopes of Longyear valley, Spitsbergen, after a heavy rainstorm in July 1972. *Geografiska Annaler Series a-Physical Geography* **64**, 105–125.

Lawrence, D. M. and Slater, A. G. (2005). A projection of severe near-surface permafrost degradation during the 21st century. *Geophysical Research Letters* **32**.

Leibman, M. O. (1995). Cryogenic landslides on the Yamal peninsula, Russia - preliminary-observations. *Permafrost and Periglacial Processes* **6**, 259–264.

Leibman, M. O., Kizyakov, A. I., Sulerzhitsky, L. D., and Zaretskaia, N. E. (2003). Dynamics of landslide slopes and their development on Yamal peninsula. *Permafrost, Vols 1 and 2*, 651–656.

Lewis, T., Lafreniere, M. J., and Lamoureux, S. F. (2012). Hydrochemical and sedimentary responses of paired High Arctic watersheds to unusual climate and permafrost disturbance, Cape Bounty, Melville Island, Canada. *Hydrological Processes* **26**, 2003–2018.

Lewkowicz, A. (1992). Factors influencing the distribution and initiation of active-layer detachment slides on Ellesmere-Island, Arctic Canada. *Periglacial Geomorphology*, 223–250.

Lewkowicz, A. (2007). Dynamics of active-layer detachment failures, Fosheim Peninsula, Ellesmere Island, Nunavut, Canada. *Permafrost and Periglacial Processes* **18**, 89–103.

Lewkowicz, A. and Harris, C. (2005a). Frequency and magnitude of active-layer detachment failures in discontinuous and continuous permafrost, northern Canada. *Permafrost and Periglacial Processes* **16**, 115–130.

Lewkowicz, A. and Harris, C. (2005b). Morphology and geotechnique of active-layer detachment failures in discontinuous and continuous permafrost, northern Canada. *Geomorphology* **69**, 275–297.

Lewkowicz, A. and Kokelj, S. (2002). Slope sediment yield in and lowland continuous permafrost environments, Canadian Arctic Archipelago. *Catena* **46**, 261–283.

Lewkowicz, A. G. (1990). "Morphology, frequency and magnitude of active-layer detachment slides, Fosheim Peninsula, Ellesmere Island, NWT". In: *Proceedings of the 5th Canadian permafrost conference*. Vol. 54, 111–118.

Liljedahl, A., Hinzman, L., Busey, R., and Yoshikawa, K. (2007). Physical short-term changes after a tussock tundra fire, Seward Peninsula, Alaska. *Journal of Geophysical Research-Earth Surface* **112**.

Lipovsky, P., Coates, J., Lewkowicz, A., and Trochim, E. (2006). "Active-Layer Detachments Following the Summer 2004 Forest Fires near Dawson City, Yukon". In: *Yukon Exploration and Geology*. Ed. by D. Emond, G. Bradshaw, L. Lewis, and L. Weston. Yukon Geological Survey, 175–194.

Luoto, M. and Hjort, J. (2004). Generalized linear modelling in periglacial studies: Terrain parameters and patterned ground. *Permafrost and Periglacial Processes* **15**, 327–338.

Luoto, M. and Hjort, J. (2005). Evaluation of current statistical approaches for predictive geomorphological mapping. *Geomorphology* **67**, 299–315.

Luoto, M. and Hjort, J. (2006). Scale matters - A multi-resolution study of the determinants of patterned ground activity in subarctic Finland. *Geomorphology* **80**, 282–294.

Luoto, M. and Seppala, M. (2002). Modelling the distribution of palsas in Finnish lapland with logistic regression and GIS. *Permafrost and Periglacial Processes* **13**, 17–28.

Mackay, J. R. (1981). Active layer slope movement in a continuous permafrost environment, Garry Island, Northwest-Territories, Canada. *Canadian Journal of Earth Sciences* **18**, 1666–1680.

MacMillan, R. A., Martin, T. C., Earle, T. J., and McNabb, D. H. (2003). Automated analysis and classification of landforms using high-resolution digital elevation data: applications and issues. *Canadian Journal of Remote Sensing* **29**, 592–606.

Major, H., Haremo, P., Dallman, W. K., and Andresen, A. (2001). *Geological Map of Svalbard 1:100 000, sheet C9G Adventdalen (revised after Major 1964)*. Report. Norsk Polar Institute Temakart nr. 31.

Mann, D. H., Groves, P., Reanier, R. E., and Kunz, M. L. (2010). Floodplains, permafrost, cottonwood trees, and peat: What happened the last time climate warmed suddenly in arctic Alaska? *Quaternary Science Reviews* **29**, 3812–3830.

Marmion, M., Hjort, J., Thuiller, W., and Luoto, M. (2008). A comparison of predictive methods in modelling the distribution of periglacial landforms in Finnish Lapland. *Earth Surface Processes and Landforms* **33**, 2241–2254.

Marmion, M., Hjort, J., Thuiller, W., and Luoto, M. (2009). Statistical consensus methods for improving predictive geomorphology maps. *Computers & Geosciences* **35**, 615–625.

Marshall, J. A. and Roering, J. J. (2014). Diagenetic variation in the Oregon Coast Range: Implications for rock strength, soil production, hillslope form, and landscape evolution. *Journal of Geophysical Research-Earth Surface* **119**, 1395–1417.

Matsuoka, N. (1990). The rate of bedrock weathering by frost action - field-measurements and a predictive model. *Earth Surface Processes and Landforms* **15**, 73–90.

Matsuoka, N. (2001a). Solifluction rates, processes and landforms: a global review. *Earth-Science Reviews* **55**, 107–134.

Matsuoka, N. (2010). Solifluction and Mudflow on a Limestone Periglacial Slope in the Swiss Alps: 14 Years of Monitoring. *Permafrost and Periglacial Processes* **21**, 219–240.

Matsuoka, N. (2001b). Direct observation of frost wedging in alpine bedrock. *Earth Surface Processes and Landforms* **26**, 601–614.

Matsuoka, N. (2008). Frost weathering and rockwall erosion in the southeastern Swiss Alps: Long-term (1994-2006) observations. *Geomorphology* **99**, 353–368.

Matsuoka, N. (2011). Climate and material controls on periglacial soil processes: Toward improving periglacial climate indicators. *Quaternary Research* **75**, 356–365.

Matsuoka, N. and Hirakawa, K. (2000). Solifluction resulting from one-sided and two-sided freezing: field data from Svalbard. *Polar geoscience* **13**, 187–201.

McCarroll, D. and Ballantyne, C. K. (2000). The last ice sheet in Snowdonia. *Journal of Quaternary Science* **15**, 765–778.

McKean, J. and Roering, J. (2004). Objective landslide detection and surface morphology mapping using high-resolution airborne laser altimetry. *Geomorphology* **57**, 331–351.

McNamara, J. P., Kane, D. L., and Hinzman, L. D. (1999). An analysis of an arctic channel network using a digital elevation model. *Geomorphology* **29**, 339–353.

McRoberts, E. and Morgenstern, N. R. (1974). The stability of thawing slopes. *Canadian Geotechnical Journal* **11**, 447–469.

McRoberts, E. C. and Morgenstern, N. (1973). A Study of Landslides in the Vicinity of the Mackenzie River Mile 205 to 660. Ottawa, ESCOM Report 73-75: Environment-Social Committee, Northern-Pipelines.

Millar, S. (2013). Mass movement processes in the periglacial environment. *Treatise on Geomorphology* **8**, 374–391.

Millar, S. W. S. (2006). Processes dominating macro-fabric generation in periglacial colluvium. *Catena* **67**, 79–87.

Milodowski, D. T., Mudd, S. M., and Mitchard, E. T. A. (2015). Topographic roughness as a signature of the emergence of bedrock in eroding landscapes. *Earth Surface Dynamics* **3**, 483–499.

Minar, J. and Evans, I. S. (2008). Elementary forms for land surface segmentation: The theoretical basis of terrain analysis and geomorphological mapping. *Geomorphology* **95**, 236–259.

Montgomery, D. R. and Dietrich, W. E. (1992). Channel initiation and the problem of landscape scale. *Science* **255**, 826–830.

Montgomery, D. R. and Dietrich, W. E. (1994). A physically-based model for the topographic control on shallow landsliding. *Water Resources Research* **30**, 1153–1171.

Montgomery, D. R. and Greenberg, H. M. (2000). Local relief and the height of Mount Olympus. *Earth Surface Processes and Landforms* **25**, 385–396.

Montgomery, D. R., Schmidt, K. M., Greenberg, H. M., and Dietrich, W. E. (2000). Forest clearing and regional landsliding. *Geology* **28**, 311–314.

Moorman, B. J., Robinson, S. D., and Burgess, M. M. (2003). Imaging periglacial conditions with ground-penetrating radar. *Permafrost and Periglacial Processes* **14**, 319–329.

Morgenstern, N. and Price, V. (1965). The Analysis of the Stability of General Slip Surfaces. *Géotechnique* **15**, 79–93.

Morse, P. D., Burn, C. R., and Kokelj, S. V. (2009). Near-Surface Ground-Ice Distribution, Kendall Island Bird Sanctuary, Western Arctic Coast, Canada. *Permafrost and Periglacial Processes* **20**, 155–171.

Murton, J. B., Coutard, J. P., Lautridou, J. P., Ozouf, J. C., Robinson, D. A., and Williams, R. B. G. (2001). Physical modelling of bedrock brecciation by ice segregation in permafrost. *Permafrost and Periglacial Processes* **12**, 255–+.

Murton, J. B., Coutard, J. P., Lautridou, J. P., Ozouf, J. C., Robinson, D. A., Williams, R. B. G., Guillemet, G., and Simmons, P. (2000). Experimental design for a pilot study on bedrock weathering near the permafrost table. *Earth Surface Processes and Landforms* **25**, 1281–1294.

Murton, J. B., Peterson, R., and Ozouf, J. C. (2006). Bedrock fracture by ice segregation in cold regions. *Science* **314**, 1127–1129.

Murton, J. (2013). "Ground ice and cryostratigraphy". In: *Treatise on Geomorphology*. Ed. by J. Shroder. Vol. 8. San Diego, CA.: Academic Press. Chap. Glacial and Periglacial Geomorphology, 173–201.

Nater, P., Arenson, L. U., and Springman, S. M. (2008). "Choosing geotechnical parameters for slope stability assessments in alpine permafrost soils". In: *Ninth International Conference on Permafrost, University of Alaska Fairbanks*. Vol. 29, 1261–1266.

Niessen, A., Vanhorssen, P., and Koster, E. A. (1992). Altitudinal zonation of selected geomorphological phenomena in an alpine periglacial area (Abisko, northern Sweden). *Geografiska Annaler Series a-Physical Geography* **74**, 183–196.

Nishimura, S., Martin, C. J., Jardine, R. J., and Fenton, C. H. (2009). A new approach for assessing geothermal response to climate change in permafrost regions. *Geotechnique* **59**, 213–227.

Niu, F., Luo, J., Lin, Z., Fang, J., and Liu, M. (2015). Thaw-induced slope failures and stability analyses in permafrost regions of the Qinghai-Tibet Plateau, China. *Landslides*, 1–11.

NPI (2014). *Terrengmodell Svalbard (S0 Terrengmodell) [Data set]*. (Visited on 10/09/2015).

Osterkamp, T. E. (2003). Establishing long-term permafrost observatories for active-layer and permafrost investigations in Alaska: 1977-2002. *Permafrost and Periglacial Processes* **14**, 331–342.

Osterkamp, T. E. (2007). Characteristics of the recent warming of permafrost in Alaska. *Journal of Geophysical Research-Earth Surface* **112**.

Osterkamp, T. E., Jorgenson, M. T., Schuur, E. A. G., Shur, Y. L., Kanevskiy, M. Z., Vogel, J. G., and Tumskoy, V. E. (2009). Physical and Ecological Changes Associated with Warming Permafrost and Thermokarst in Interior Alaska. *Permafrost and Periglacial Processes* **20**, 235–256.

Pack, R. T., Tarboton, D., and Goodwin, C. (1999). SINMAP 2.0-A Stability Index Approach to Terrain Stability Hazard Mapping, User's Manual.

Parker, R. N., Rosser, N. J., and Hales, T. C. (2017). Spatial prediction of earthquake-induced landslide probability. *Nat. Hazards Earth Syst. Sci. Discuss.* **1**.

Pastick, N. J., Jorgenson, M. T., Wylie, B. K., Nield, S. J., Johnson, K. D., and Finley, A. O. (2015). Distribution of near-surface permafrost in Alaska: Estimates of present and future conditions. *Remote Sensing of Environment* **168**, 301–315.

Pautler, B. G., Simpson, A. J., McNally, D. J., Lamoureux, S. F., and Simpson, M. J. (2010). Arctic Permafrost Active Layer Detachments Stimulate Microbial Activity and Degradation of Soil Organic Matter. *Environmental Science & Technology* **44**, 4076–4082.

Pedregosa, F., Varoquaux, G., Gramfort, A., Michel, V., Thirion, B., Grisel, O., Blondel, M., Prettenhofer, P., Weiss, R., Dubourg, V., Vanderplas, J., Passos, A., Cournapeau, D., Brucher, M., Perrot, M., and Duchesnay, E. (2011). Scikit-learn: Machine Learning in Python. *Journal of Machine Learning Research* **12**, 2825–2830.

Pike, R. J. (1988). The geometric signature - quantifying landslide-terrain types from digital elevation models. *Mathematical Geology* **20**, 491–511.

Ping, C. L., Michaelson, G. J., Kimble, J. M., Romanovsky, V. E., Shur, Y. L., Swanson, D. K., and Walker, D. A. (2008). Cryogenesis and soil formation along a bioclimate gradient in Arctic North America. *Journal of Geophysical Research-Biogeosciences* **113**.

Pissart, A. (1967). Les modalités de l'écoulement de l'eau sur l'île Prince Patrick. *Biuletyn Peryglacjalny* **16**, 217–224.

Prick, A. (2003). Frost weathering and rock fall in an arctic environment, Longyearbyen, Svalbard. *Permafrost, Vols 1 and 2*, 907–912.

Prima, O. D. A. and Yoshida, T. (2010). Characterization of volcanic geomorphology and geology by slope and topographic openness. *Geomorphology* **118**, 22–32.

Prima, O. D. A., Echigo, A., Yokoyama, R., and Yoshida, T. (2006). Supervised landform classification of Northeast Honshu from DEM-derived thematic maps. *Geomorphology* **78**, 373–386.

Rapp, A. (1960a). Recent development of mountain slopes in Kärkevagge and surroundings, northern Scandinavia. *Geografiska Annaler* **42**, 65–200.

Rapp, A. (1960b). Talus slopes and mountain walls at Tempelfjorden, Spitsbergen: a geomorphological study of the denudation of slopes in an arctic locality.

Rea, B. R., Whalley, W. B., Rainey, M. M., and Gordon, J. E. (1996). Blockfields, old or new? Evidence and implications from some plateaus in northern Norway. *Geomorphology* **15**, 109–121.

Rea, B. (2007). Blockfields (Felsenmeer). *The Encyclopedia of Quaternary Science, edited by: Elias, SA* **3**, 523–534.

Rempel, A. W. (2007). Formation of ice lenses and frost heave. *Journal of Geophysical Research-Earth Surface* **112**.

Rempel, A. W., Wettlaufer, J. S., and Worster, M. G. (2004). Premelting dynamics in a continuum model of frost heave. *Journal of Fluid Mechanics* **498**, 227–244.

Ridefelt, H. and Boelhouwers, J. (2006). Observations on regional variation in solifluction landform morphology and environment in the Abisko region, northern Sweden. *Permafrost and Periglacial Processes* **17**, 253–266.

Ridefelt, H., Boelhouwers, J., and Eiken, T. (2009). Measurement of solifluction rates using multi-temporal aerial photography. *Earth Surface Processes and Landforms* **34**, 725–737.

Ridefelt, H., Boelhouwers, J., and Etzelmüller, B. (2011). Local variations of solifluction activity and environment in the Abisko Mountains, Northern Sweden. *Earth Surface Processes and Landforms* **36**, 2042–2053.

Ridefelt, H., Etzelmüller, B., and Boelhouwers, J. (2010). Spatial Analysis of Solifluction Landforms and Process Rates in the Abisko Mountains, Northern Sweden. *Permafrost and Periglacial Processes* **21**, 241–255.

Rixhon, G. and Demoulin, A. (2013). Evolution of slopes in a cold climate. *Glacial and Periglacial Geomorphology*, 392–415.

Romstad, B. and Etzelmüller, B. (2012). Mean-curvature watersheds: A simple method for segmentation of a digital elevation model into terrain units. *Geomorphology* **139**, 293–302.

Romstad, B. (2001). "Improving relief classification with contextual merging". In: *ScanGIS*, 3–13.

Ross, N., Brabham, P. J., Harris, C., and Christiansen, H. H. (2007). Internal structure of open system pingos, Adventdalen, Svalbard: The use of resistivity tomography to assess ground-ice conditions. *Journal of Environmental and Engineering Geophysics* **12**, 113–126.

Rudberg, S. (1961). Geomorphological processes in a cold semi-arid region. *Axel Heiberg Island research reports, preliminary report* **1962**, 139–150.

Rudy, A. C. A., Lamoureux, S. F., Treitz, P., and Collingwood, A. (2013). Identifying permafrost slope disturbance using multi-temporal optical satellite images and change detection techniques. *Cold Regions Science and Technology* **88**, 37–49.

Rudy, A. C. A., Lamoureux, S. F., Treitz, P., and Ewijk, K. Y. van (2016). Transferability of regional permafrost disturbance susceptibility modelling using generalized linear and generalized additive models. *Geomorphology* **264**, 95–108.

Rudy, A. C. A., Lamoureux, S. F., Treitz, P., Van Ewijk, K., Bonnaventure, P. P., and Budkewitsch, P. (2017). Terrain Controls and Landscape-Scale Susceptibility Modelling of Active-Layer Detachments, Sabine Peninsula, Melville Island, Nunavut. *Permafrost and Periglacial Processes* **28**, 79–91.

Sanders, D. (2010). Sedimentary facies and progradational style of a Pleistocene talus-slope succession, Northern Calcareous Alps, Austria. *Sedimentary Geology* **228**, 271–283.

Sass, O. (2005). Spatial patterns of rockfall intensity in the northern Alps. *Zeitschrift fur Geomorphologie* **138**, 51–65.

Schuur, E. A. G., McGuire, A. D., Schadel, C., Grosse, G., Harden, J. W., Hayes, D. J., Hugelius, G., Koven, C. D., Kuhry, P., Lawrence, D. M., Natali, S. M., Olefeldt, D., Romanovsky, V. E., Schaefer, K., Turetsky, M. R., Treat, C. C., and Vonk, J. E. (2015). Climate change and the permafrost carbon feedback. *Nature* **520**, 171–179.

Schuur, E. A. G., Bockheim, J., Canadell, J. G., Euskirchen, E., Field, C. B., Goryachkin, S. V., Hagemann, S., Kuhry, P., Lafleur, P. M., Lee, H., Mazhitova, G., Nelson, F. E., Rinke, A., Romanovsky, V. E., Shiklomanov, N., Tarnocai, C., Venevsky, S., Vogel, J. G., and Zimov, S. A. (2008). Vulnerability of permafrost carbon to climate change: Implications for the global carbon cycle. *Bioscience* **58**, 701–714.

Setsa, R. (2016). (Visited on 11/15/2017).

Showstack, R. (2017). *Eos: Earth and Space Science News* **98**.

Shur, Y., Hinkel, K. M., and Nelson, F. E. (2005). The transient layer: Implications for geocryology and climate-change science. *Permafrost and Periglacial Processes* **16**, 5–17.

Siewert, M. B., Krautblatter, M., Christiansen, H. H., and Eckerstorfer, M. (2012). Arctic rockwall retreat rates estimated using laboratory-calibrated ERT measurements of talus cones in Longyeardalen, Svalbard. *Earth Surface Processes and Landforms* **37**, 1542–1555.

Skempton, A. and DeLory, F. (1957). "Stability of natural slopes in London clay". In: *Selected Papers on Soil Mechanics*. Thomas Telford Publishing, 70–73.

Smith, J. S. (2004). Scaled geotechnical centrifuge modelling of gelifluction. PhD thesis. Cardiff University.

Statham, I. (1976). A scree slope rockfall model. *Earth Surface Processes and Landforms* **1**, 43–62.

Stepinski, T. and Vilalta, R. (2005). Digital topography models for Martian surfaces. *Ieee Geoscience and Remote Sensing Letters* **2**, 260–264.

Stocker, T. F., Qin, D., Plattner, G. K., Tignor, M., Allen, S. K., Boschung, J., Nauels, A., Xia, Y., Bex, V., and Midgley, P. M. (2013). *IPCC, 2013: summary for policymakers in climate change 2013: the physical science basis, contribution of working group I to the fifth assessment report of the intergovernmental panel on climate change*. Report. Cambridge University Press, Cambridge, New York, USA.

Stocker, T. (2014). Climate change 2013: the physical science basis: Working Group I contribution to the Fifth assessment report of the Intergovernmental Panel on Climate Change. Cambridge University Press.

Swanson, D. (2010). *Mapping of Erosion Features related to thaw of permafrost in Bering Land Bridge National Preserve, Cape Krusenstern National Monument, and Kobuk Valley National Park.* Report. National Park Service.

Swanson, D. (2012). *Mapping erosion features to thaw of permafrost in the Noatak Naional Preserve, Alaska.* Report. National Park Service.

Swanson, D. (2014). Mapping of Erosion Features Related to Thaw of Permafrost in the NPS Arctic Inventory and Monitoring Network, Alaska. *Natural Resource Data Series NPS/ARCN/NRDS–2010* **122**.

Syvitski, J. P. M. (2002). Sediment discharge variability in Arctic rivers: implications for a warmer future. *Polar Research* **21**, 323–330.

Taber, S. (1929). Frost heaving. *Journal of Geology* **37**, 428–461.

Table, W. (2008). Frost-Susceptible Soils. *American Concrete Pavement Association*.

Talebi, A., Troch, P. A., and Uijlenhoet, R. (2008). A steady-state analytical slope stability model for complex hillslopes. *Hydrological Processes* **22**, 546–553.

Tape, K., Sturm, M., and Racine, C. (2006). The evidence for shrub expansion in Northern Alaska and the Pan-Arctic. *Global Change Biology* **12**, 686–702.

Tarnocai, C., Canadell, J. G., Schuur, E. A. G., Kuhry, P., Mazhitova, G., and Zimov, S. (2009). Soil organic carbon pools in the northern circumpolar permafrost region. *Global Biogeochemical Cycles* **23**, 11.

Tolgensbakk, J., Sørbel, L., and Høgvard, K. (2000). Adventdalen, geomorphological and quaternary geological map, Svalbard 1: 100,000, Spitsbergen sheet C9Q. *Norsk Polarinstitutt Temakart* **32**.

Trochim, E. D., Jorgenson, M. T., Prakash, A., and Kane, D. L. (2016a). Geomorphic and biophysical factors affecting water tracks in northern Alaska. *Earth and Space Science* **3**, 123–141.

Trochim, E. D., Prakash, A., Kane, D. L., and Romanovsky, V. E. (2016b). Remote sensing of water tracks. *Earth and Space Science* **3**, 106–122.

Ukraintseva, N. G. and Leibman, M. O. (2007). The effect of cryogenic landslides (active-layer detachments) on fertility of tundra soils on Yamal peninsula, Russia. *Landslides/slope instability. AEG Special Publication* **23**, 1605–1615.

USGS (2015). *5 meter Alaska Digital Elevation Model (DEM) - USGS National Map*. (Visited on 09/02/2016).

Van Den Eeckhaut, M., Kerle, N., Poesen, J., and Hervas, J. (2012). Object-oriented identification of forested landslides with derivatives of single pulse LiDAR data. *Geomorphology* **173**, 30–42.

Van Rossum, G. and Drake, F. L. (2003). Python language reference manual. Network Theory.

Vorpahl, P., Elsenbeer, H., Marker, M., and Schroder, B. (2012). How can statistical models help to determine driving factors of landslides? *Ecological Modelling* **239**, 27–39.

Walber (2017). *Precision and recall - Wikipedia*.

Walder, J. and Hallet, B. (1985). A theoretical-model of the fracture of rock during freezing. *Geological Society of America Bulletin* **96**, 336–346.

Walker, D. A., Epstein, H. E., Romanovsky, V. E., Ping, C. L., Michaelson, G. J., Daanen, R. P., Shur, Y., Peterson, R. A., Krantz, W. B., Raynolds, M. K., Gould, W. A., Gonzalez, G., Nicolsky, D. J., Vonlanthen, C. M., Kade, A. N., Kuss, P., Kelley, A. M., Munger, C. A., Tamocai, C. T., Matveyeva, N. V., and Daniels, F. J. A. (2008). Arctic patterned-ground ecosystems: A synthesis of field studies and models along a North American Arctic Transect. *Journal of Geophysical Research-Biogeosciences* **113**.

Wang, H., Xing, X., Li, T., Qin, Z., and Yang, J. (2014). "Slope Instability Phenomenon in the Permafrost Region Along the Qinghai–Tibetan Highway, China". In: *Landslides in Cold Regions in the Context of Climate Change*. Springer, 11–22.

Washburn, A. L. (1980). Permafrost features as evidence of climatic-change. *Earth-Science Reviews* **15**, 327–402.

Westen, C. J. van, Castellanos, E., and Kuriakose, S. L. (2008). Spatial data for landslide susceptibility, hazard, and vulnerability assessment: An overview. *Engineering Geology* **102**, 112–131.

Wheaton, J. M., Brasington, J., Darby, S. E., and Sear, D. A. (2010). Accounting for uncertainty in DEMs from repeat topographic surveys: improved sediment budgets. *Earth Surface Processes and Landforms* **35**, 136–156.

Williams, P. and Smith, M. (1989). The frozen earth. Fundamentals of Geocryology. Studies in Polar Research. Cambridge: Cambridge University Press, 306 pp.

Wilson, F. H., Hults, C. P., Mull, C. G., and Karl, S. M. (2015). Geologic map of Alaska.

Yokoyama, R., Shirasawa, M., and Pike, R. J. (2002). Visualizing topography by Openness: A new application of image processing to digital elevation models. *Photogrammetric Engineering and Remote Sensing* **68**, 257–265.

Zhang, T., Barry, R. G., Knowles, K., Heginbottom, J., and Brown, J. (1999). Statistics and characteristics of permafrost and ground-ice distribution in the Northern Hemisphere 1. *Polar Geography* **23**, 132–154.

Zhang, T., Heginbottom, J., Barry, R. G., and Brown, J. (2000). Further statistics on the distribution of permafrost and ground ice in the Northern Hemisphere. *Polar geography* **24**, 126–131.

Zimov, S. A., Schuur, E. A. G., and Chapin, F. S. (2006). Permafrost and the global carbon budget. *Science* **312**, 1612–1613.